



**Mass Transport Through Freestanding  
Carbon Nanomembranes**

Yang Yang

Bielefeld University

2019



# **Mass Transport Through Freestanding Carbon Nanomembranes**

Dissertation

zur

Erlangung der Doktorwürde

der Fakultät für Physik

der Universität Bielefeld

**Yang Yang**

Bielefeld, February 2019

**Declaration:**

I hereby declare that the work in this thesis is my original work. None but the indicated resources were used.

**Committee:**

1. Prof. Dr. Armin Gölzhäuser
2. Prof. Dr. Dario Anselmetti

## Abstract

Membrane separation provides an energy-efficient technology for molecular separation. Conventional filtration systems are constrained by a trade-off between permeance and selectivity that results from broad pore size distribution. Recent developments on nanotechnology have demonstrated the potential to overcome this limitation by utilizing well-defined nanoconduits that allow a coordinated passage of water molecules. Fabrication of these materials is still very challenging, but their performance inspires research toward nanofabricated membranes.

Carbon nanomembranes (CNMs) are a special class of 2D materials made by crosslinking of self-assembled monolayers. This work will present the rapid and selective water permeation through a  $\sim 1.2$  nm thin CNM fabricated from terphenylthiol (TPT) precursors. Molecular transport through TPT CNMs is investigated by mass-loss measurements and gas permeation in vacuum system. TPT CNMs block the passage of most gases and liquids, while permitting water and helium to pass through. In particular, water transits with a remarkably high permeance of  $\sim 1.1 \times 10^{-4}$  mol $\cdot$ m $^{-2}\cdot$ s $^{-1}\cdot$ Pa $^{-1}$ , 2,500 times faster than helium. Scanning probe microscopy reveals that the membrane consists of sub-nanometer channels with a high areal density of  $10^{18}$  m $^{-2}$ . Assuming all channels in a TPT CNM are active in mass transport, we find a single-channel permeation of  $\sim 66$  water molecules $\cdot$ s $^{-1}\cdot$ Pa $^{-1}$ . This suggests that water molecules translocate fast and cooperatively through the sub-nanometer channels, similar to carbon nanotubes and membrane proteins (aquaporins).

Furthermore, ion transport across these membranes are investigated by conductance measurements using both DC and AC methods. The results show that freestanding TPT CNMs act as ionic insulators, preventing the penetration of ionic species including protons. The specific membrane resistance reaches  $\sim 10^4$   $\Omega\cdot$ cm $^2$ , comparable to the typical high resistance of planar lipid bilayers. The single-channel conductance yields  $2 \times 10^{-18}$  S in 1 M KCl solution,  $\sim 10^7$  lower than that of biological porins. This again confirms the existing of sub-nm channels within TPT CNMs.

Unlike other nanostructured membranes, CNMs are built in a versatile and scalable fabrication process, thus these 2D sieves will inspire the development of various advanced filtration systems that require highly efficient and precise separations.

# Table of Contents

|  |           |
|--|-----------|
| <b>Chapter 1 Introduction.....</b>                             | <b>11</b> |
| 1.1 Membrane Separation .....                                  | 11        |
| 1.2 Molecular Transport Mechanisms.....                        | 12        |
| 1.2.1 Solution-Diffusion Model .....                           | 13        |
| 1.2.2 Molecular Sieving .....                                  | 14        |
| 1.2.3 Knudsen Diffusion .....                                  | 15        |
| 1.2.4 Poiseuille Flow .....                                    | 18        |
| 1.3 Transport Characteristics: Permeance and Selectivity ..... | 19        |
| 1.4. Recent Developments on Membrane Materials .....           | 20        |
| 1.4.1 Conventional Polymeric Membranes .....                   | 20        |
| 1.4.2 Next-Generation Molecularly Selective Membranes.....     | 22        |
| 1.4.3 Carbon Nanomembranes (CNMs).....                         | 25        |
| 1.5 Motivation and Organization of the Thesis.....             | 29        |
| <br>   |           |
| <b>Chapter 2 Basics and Methodology .....</b>                  | <b>31</b> |
| 2.1 Fabrication of CNMs from SAMs.....                         | 31        |
| 2.1.1 SAM Formation .....                                      | 31        |
| 2.1.2 Crosslinking of SAMs.....                                | 33        |
| 2.2 Characterization of SAMs and CNMs .....                    | 34        |
| 2.2.1 X-ray Photoelectron Spectroscopy (XPS).....              | 35        |
| 2.2.2 Scanning Tunneling Microscopy (STM) .....                | 36        |
| 2.2.3 Atomic Force Microscopy (AFM) .....                      | 37        |
| 2.2.4 Helium Ion Microscopy (HIM).....                         | 39        |
| 2.2.5 Electrochemical Impedance Spectroscopy (EIS).....        | 40        |

---

|   |           |
|---|-----------|
| <b>Chapter 3 Fabrication of Micrometer-Scale Freestanding CNMs .....</b>                | <b>45</b> |
| 3.1 Fabrication of CNMs on Au(111)/Mica.....  | 45        |
| 3.1.1 CNMs from a New “Bulky” Precursor HPB Derivative 1.....                           | 45        |
| 3.1.2 CNMs from an Established “Linear” Precursor TPT.....                              | 51        |
| 3.2 Micrometer-Scale Freestanding CNMs on Si <sub>3</sub> N <sub>4</sub> /Si Chips..... | 52        |
| 3.3 Summary .....   | 55        |
| <br>  |           |
| <b>Chapter 4 Rapid and Selective Water Permeation Through TPT CNMs .....</b>            | <b>57</b> |
| 4.1 Introduction.....   | 57        |
| 4.2 Mass Loss Methods.....  | 57        |
| 4.2.1 Basics and Setup .....  | 57        |
| 4.2.2 Control Measurements .....  | 58        |
| 4.2.3 Vapor Permeation Through TPT CNMs.....  | 60        |
| 4.3 Measurements in Vacuum System.....  | 62        |
| 4.3.1 Basics and Setup .....  | 62        |
| 4.3.2 Gas Permeation Through TPT CNMs.....  | 64        |
| 4.4 Understanding the Permeation Behavior .....   | 67        |
| 4.4.1 Structure of TPT SAMs and CNMs.....   | 67        |
| 4.4.2 Molecular Transport Mechanism Through TPT CNMs.....                               | 72        |
| 4.5 Summary .....   | 75        |
| <br>  |           |
| <b>Chapter 5 Ion Exclusion by TPT CNMs .....</b>  | <b>77</b> |
| 5.1 Introduction.....   | 77        |
| 5.2 Basics and Setup .....  | 77        |
| 5.3 Ion Conductance Measurements .....  | 80        |
| 5.3.1 Measurements Using DC Method.....   | 80        |
| 5.3.2 Measurements Using AC Method.....   | 85        |
| 5.4 Summary .....   | 91        |



|  |            |
|--|------------|
| <b>Chapter 6 Conclusions and Outlook .....</b> | <b>93</b>  |
| <b>List of Figures .....</b>                   | <b>95</b>  |
| <b>List of Tables .....</b>                    | <b>102</b> |
| <b>References .....</b>                        | <b>103</b> |
| <b>Acknowledgement .....</b>                   | <b>113</b> |



# Chapter 1

## Introduction

### 1.1 Membrane Separation

Beginning in the early 1960s, the commercialization of membrane separation in the modern industry came out with the Loeb-Sourirajan technique for making high-performance reverse osmosis membranes (**Figure 1.1**).<sup>1-2</sup> Since then, membrane technology has received increased worldwide attention as global industries strive for higher energy efficiency and lower environmental impact. In comparison with traditional separation processes such as distillation, membrane-based separation has the potential to achieve more than 90% energy savings.<sup>3</sup> Up to the present, membrane separation spans a broad range of applications, e.g., water purification, gas separation, food processing, pharmaceutical industries, etc., playing an essential role in our daily life. The pore size of the membranes varies from several angstrom to micrometer dimension depending on the purpose of usage.



*Figure 1.1. First demonstration of reverse osmosis membranes.*<sup>4</sup>

## 1.2 Molecular Transport Mechanisms

Membranes separate targeted products from impurities can be distinguished basically in two categories: (i) transport in dense polymeric membranes without defined pores, e.g., reverse osmosis membranes, most gas separation membranes, described by a solution-diffusion model, in which the separation is achieved by the differences in the solubility and mobility of permeants in membranes; and (ii) transport in porous membranes, in which permeants are separated by transport through small pores,<sup>2,5</sup> commonly interpreted by transport mechanisms such as molecular sieving, Knudsen diffusion and Poiseuille flow.<sup>6</sup> The transition between the solution-diffusion and pore-flow mechanisms seems to occur with membranes having pores in the diameter range of 0.5–1 nm.<sup>7</sup>

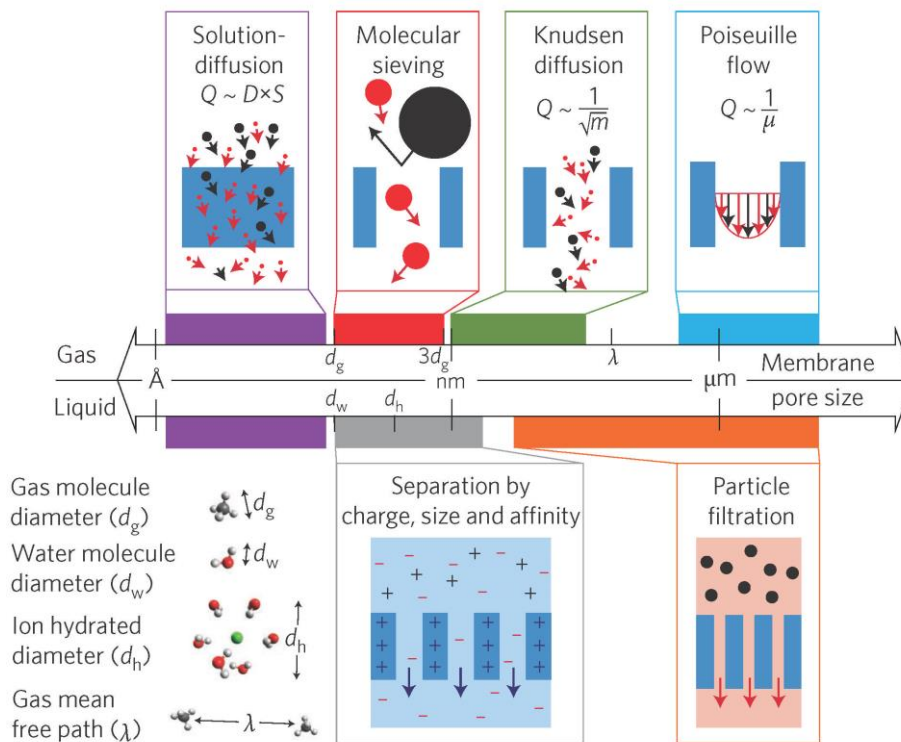


**Figure 1.2.** Mechanisms of molecular transport through dense membranes and porous membranes.<sup>2,5</sup> Reprinted with permission from ref. 5, Springer Nature.

### 1.2.1 Solution-Diffusion Model

Molecular transport in dense polymeric membrane is described by a solution-diffusion mechanism, which is generally accepted as a three-step process: (i) molecules in the bulk feed diffuse to the membrane surface and dissolve in a membrane; (ii) diffuse through the membrane; and (iii) desorb from the membrane and diffuse to the bulk permeate. A basic assumption of transport through membranes is that the fluid at the interface of the membrane material are in an equilibrium with the bulk phases of the feed and permeate sides.<sup>2,8</sup> This assumption implies that the second diffusion step is the rate-limiting step, which seems to be true for most membrane processes, but may fail in some cases, such as facilitated and directed transport.

On the basis of this assumption, the solution-diffusion model additionally assumes that the pressure is uniform within the membrane, and the transport of permeants is only driven by a concentration gradient across the membrane. Thus, the diffusion process inside the membrane can be described by Fick's law of diffusion.<sup>6</sup>

$$J = -D \frac{dc}{dx} \quad (\text{Equation 1.1})$$

where  $J$  is the mass flux ( $\text{kg}\cdot\text{m}^{-2}\cdot\text{s}^{-1}$ ),  $D$  is the diffusion coefficient ( $\text{m}^2\cdot\text{s}^{-1}$ ),  $c$  is the concentration of the component ( $\text{kg}\cdot\text{m}^{-3}$ ), and  $x$  is the thickness of the membrane (m).

In liquid systems, the diffusivity of spherical species in a dilute bulk solution can be expressed by the Stokes-Einstein equation:<sup>9</sup>

$$D_{bulk} = \frac{kT}{6\pi\mu r} \quad (\text{Equation 1.2})$$

where  $k$  is Boltzmann constant,  $T$  is the temperature (K),  $\mu$  is the solvent viscosity ( $\text{Pa}\cdot\text{s}$ ), and  $r$  is the radius of the solute (m).

Traditional polymeric membranes usually give a thickness of several  $\mu\text{m}$ , thus diffusion through these materials is quite slow. According to Fick's law, in practical diffusion-governed processes, a sufficient flux through the membrane is realizable by means of reducing the membrane thickness and creating large concentration gradients across the membrane.<sup>2</sup>

### 1.2.2 Molecular Sieving

When the pore dimensions are similar in size to those of target molecules, the separation of molecules is described by molecular sieving. The theoretical study of hindered transport in the fine pores of molecular dimensions dates back to early 1900s.<sup>10-11</sup> These studies considered many aspects of the pore–molecule interaction, including steric hindrance, hydrodynamic interaction, and electrostatic screening due to the Debye-layer repulsion.<sup>11-12</sup> In the case of steric hindrance, smaller molecules are more likely to find the pore compared with larger molecules, due to a faster Brownian motion of the molecules with smaller size. The hydrodynamic hindrance occurs especially in a pressure-driven transport. The motion of a particle within the pore is hindered by hydrodynamic drag forces. These hindrance effects are primarily a function of  $\lambda$ , where  $\lambda$  is a ratio of molecule radius  $r_m$  to pore radius  $r_p$ .

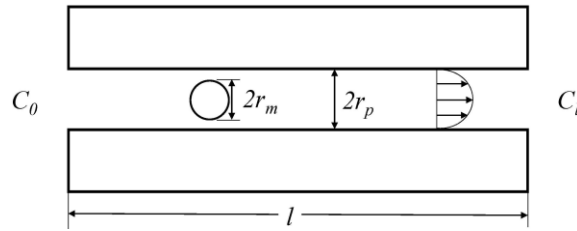


**Figure 1.3.** Spherical particle flow in a cylindrical pore.<sup>11</sup>

In liquid systems, when a steady state is reached along a pore between the two sides, the effective solute flux of a diffusion-dominated process can be quantified by:<sup>11,13</sup>

$$J = \frac{\Phi K_d D_{bulk}}{l} (C_0 - C_l) \quad (\text{Equation 1.3})$$

where  $\Phi$  is the equilibrium partitioning or distribution coefficient determined from the ratio of the average intrapore concentration to that in bulk solution,  $K_d$  is the hindrance factor for diffusive transport,  $D_{bulk}$  is the diffusion coefficient of solute in dilute bulk solution determined from Equation 1.2, the quantity  $K_d D_{bulk}$  represents an averaged intrapore diffusion coefficient, based on solute concentrations averaged over the pore cross section,  $l$  is the pore length,  $C_0$  and  $C_l$  are the solute concentration at the upstream and downstream surfaces of the pore, respectively.

The transport phenomena in molecular-dimension pores is not only important for fundamental studies, but also useful in many industrial applications. For example, the flow rate of water molecules through sub-nanometer sized channels, exceeds the predictions from a continuum flow in macroscopic channels by several orders of magnitude. This encourages the design of highly efficient water filters. Recent developments on fabricating nanopores with regular size and shape, e.g., carbon nanotubes, track-etched pores, provide new opportunities for further understanding the molecular sieving phenomena.

### 1.2.3 Knudsen Diffusion

For cylindrical pores, if the pore diameter is much larger than the molecular size but smaller than the mean free path, the molecules will collide with pore walls more frequently than with other molecules.<sup>6</sup> This transport process is governed by Knudsen diffusion, which usually occurs at low pressure and with small pores.

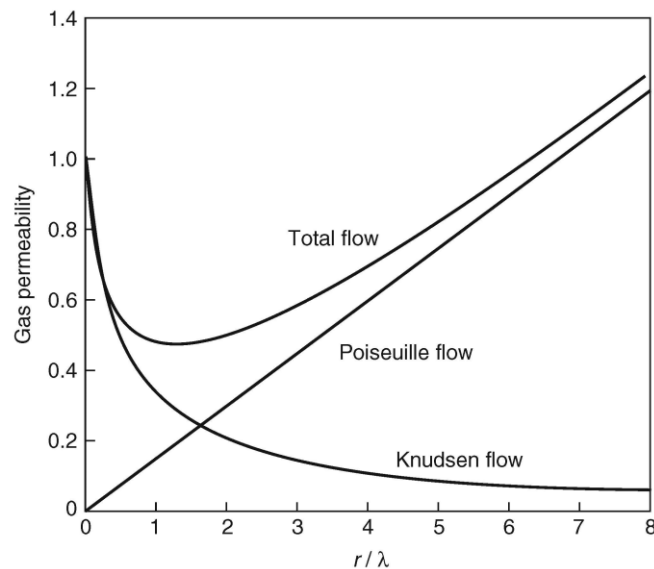


**Figure 1.4.** Permeation properties of Knudsen and Poiseuille flow as a function of the pore radius ( $r$ ) divided by the mean pore path ( $\lambda$ ) of the gas.<sup>2,14</sup>

The Knudsen number  $K_n$ , defined as the ratio of the molecular mean free path  $\lambda$  to the pore diameter  $d_p$ , is an important dimensionless quantity which can be used to

distinguish the flow regimes.

$$K_n = \frac{\lambda}{d_p} \quad (\text{Equation 1.4})$$

If the Knudsen number is large, i.e.,  $K_n \gg 1$ , the transport will be dominated by Knudsen diffusion (**Figure 1.4**). If the Knudsen number is small, diffusion in the pore has the same characteristics as it does in the bulk phase, then the transport is treated as a Poiseuille flow (see Section 1.2.4).

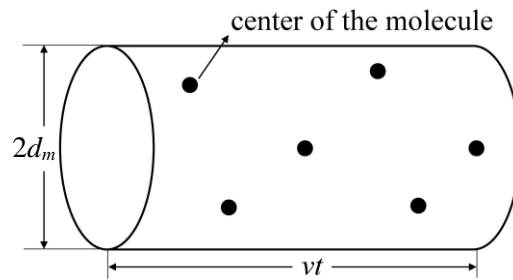


**Figure 1.5.** Illustration of estimating mean free path from kinetic theory.<sup>15-16</sup>

As the mean free path of liquids is only several angstrom, the Knudsen number is very small. Therefore, Knudsen diffusion is almost negligible for liquids. The mean free path of gases can be estimated from the kinetic theory. For the molecule with a diameter of  $d_m$ , the effective collision area is considered to be  $A = \pi d_m^2$ . The mean free path, i.e., the average distance that a molecule needs to travel to make a collision with another molecule, then can be estimated from dividing the length of molecular path by number of collisions occurred (**Figure 1.5**).<sup>15-16</sup>

$$\lambda = \frac{vt}{\pi d_m^2 \cdot \sqrt{2} vt \cdot N_V} = \frac{1}{\sqrt{2} \pi d_m^2 \cdot N_V} \quad (\text{Equation 1.5})$$

where  $v$  is the velocity of diffusing molecules ( $\text{m} \cdot \text{s}^{-1}$ ),  $t$  is the time (s),  $\pi d_m^2 \cdot \sqrt{2} vt$  defines the effective interaction volume ( $\text{m}^3$ ) by taking into account that the velocities of the particles have a Maxwell distribution,<sup>17</sup>  $N_V$  is the number of molecules per unit volume ( $\text{m}^{-3}$ ).



$N_V$  can be determined from the ideal gas law,  $pV = nRT$ :

$$N_V = \frac{p}{RT} \cdot N_A \quad (\text{Equation 1.6})$$

Accordingly,

$$\lambda = \frac{kT}{\sqrt{2}\pi d_m^2 p} \quad (\text{Equation 1.7})$$

where  $k$  is Boltzmann constant,  $p$  is the pressure.

The Knudsen diffusion coefficient can then be derived from the kinetic theory.<sup>6,18-19</sup>

$$D_K = \frac{1}{3} d_p \bar{v} \quad (\text{Equation 1.8})$$

where  $\bar{v}$  is the average velocity of the particles, equal to  $\frac{2}{\sqrt{\pi}} v$ .

According to the kinetic molecular theory, the kinetic energy of gas particles is proportional to the absolute temperature.<sup>18</sup>

$$\frac{1}{2} m v^2 = kT \quad (\text{Equation 1.9})$$

the Knudsen diffusion coefficient can thus be expressed as follows:

$$D_K = \frac{d_p}{3} \sqrt{\frac{8kT}{\pi m}} = \frac{d_p}{3} \sqrt{\frac{8RT}{\pi M}} \quad (\text{Equation 1.10})$$

Following the equation for Fick's law of diffusion, the flow rate of Knudsen diffusion through a cylindrical pore can be expressed as:

$$Q = D_K \times \frac{\Delta c}{l} \times \frac{\pi d_p^2}{4} = D_K \times \frac{\Delta p}{RTl} \times \frac{\pi d_p^2}{4} = \frac{d_p^3 \Delta p}{6l} \sqrt{\frac{2\pi}{MRT}} \quad (\text{Equation 1.11})$$

where  $Q$  is the molar flow rate ( $\text{mol}\cdot\text{s}^{-1}$ ),  $l$  is the pore length (m),  $M$  is the molar mass ( $\text{kg}\cdot\text{mol}^{-1}$ ),  $\Delta p$  is the pressure drop across the pore (Pa).

Accordingly, if the fluid flow fits to the Knudsen diffusion regime, the selectivity  $\alpha_{i,j}$  of species  $i$  to  $j$  is only dependent of the square root of the molecular mass.

$$\alpha_{i,j} = \frac{P_i}{P_j} = \sqrt{\frac{m_j}{m_i}} \quad (\text{Equation 1.12})$$

where  $P_i$  and  $P_j$  are permeance of species  $i$  and  $j$ . Permeance is defined as the ratio of flux to pressure difference. This relation can be used to readily determine whether the flow is within the Knudsen regime from the measured permeances.

### 1.2.4 Poiseuille Flow

Poiseuille flow describes a laminar flow of Newtonian fluids through a long cylindrical pore where the pore diameter is larger than the mean free path and the flow characteristics are determined mainly by the molecule–molecule collisions. This transport process is expressed by the Hagen-Poiseuille law, which can be derived from the Navier-Stokes equations.<sup>20-21</sup>

$$v = \frac{d^2 \Delta p}{32 \mu l} \quad (\text{Equation 1.13})$$

where  $v$  is the flow velocity of fluids through the pore ( $\text{m}\cdot\text{s}^{-1}$ ),  $d$  is the pore diameter (m),  $\Delta p$  is the pressure drop across the pore (Pa),  $\mu$  is the fluid viscosity ( $\text{Pa}\cdot\text{s}$ ),  $l$  is the pore length (m).

The volumetric flow rate is then given by:

$$Q = \frac{\pi d^4 \Delta p}{128 \mu l} \quad (\text{Equation 1.14})$$

The flux for a membrane with a certain number of pores can be calculated as follows:<sup>2</sup>

$$J = \frac{Q \cdot N}{A} = \frac{\pi d^4 \Delta p}{128 \mu l} \times \frac{N}{A} \quad (\text{Equation 1.15})$$

where  $N$  is number of pores per square meter of the membrane,  $A$  is the membrane area.

For membranes with a given porosity  $\varepsilon$ ,

$$\varepsilon = N \times \frac{\pi d^2}{4} \times \frac{1}{A} \quad (\text{Equation 1.16})$$

The membrane flux can be expressed by combining Equations 1.14 and 1.15:

$$J = \frac{\varepsilon d^2 \Delta p}{32 \mu l} \quad (\text{Equation 1.17})$$

Unlike the transport in Knudsen regime, the flow in Poiseuille regime relies on the viscosity of the fluids. The fluid with a low viscosity travels faster in the pore.

### 1.3 Transport Characteristics: Permeance and Selectivity

The performance of a membrane is characterized by two main properties:

(i) Permeance  $P$ , which describes how fast the molecules can move through a membrane per unit area per unit pressure.

$$P = \frac{Q}{A \cdot \Delta p} \quad (\text{Equation 1.18})$$

where  $Q$  is the flow rate across the membrane,  $A$  is the membrane area,  $\Delta p$  is the pressure difference.

and (ii) Selectivity  $\alpha_{i,j}$ , defining the degree to which a membrane separates the targeted molecule  $i$  from the rest  $j$ .

$$\alpha_{i,j} = \frac{P_i}{P_j} \quad (\text{Equation 1.19})$$

Membranes with both high permeance and high selectivity are considered as ideal filters, which is in principle realizable by designing a material with an ultrathin selective layer with uniform pore diameters. Polymeric membranes are the most successful example in commercialization, however, accomplishing a precise control over the structure of these membranes remains a bottleneck. Recent developments in nanotechnology advocates meeting the challenge by constructing a membrane with molecular-level design approaches.<sup>22-24</sup>

## 1.4. Recent Developments on Membrane Materials

### 1.4.1 Conventional Polymeric Membranes

Commercially available membranes are mainly polymeric, since polymer membranes are more versatile, less expensive and less brittle than inorganic membranes, and can be readily up-scaled for commercial use. However, the development of these membranes are constrained by a major drawback that the polymer chains are usually arranged in a random order, which leads to a wide distribution of free volume or pore size in the bulk membrane material. As a result, polymer membranes in general exhibit a trade-off between permeance and selectivity (**Figure 1.6**).<sup>22,24</sup>

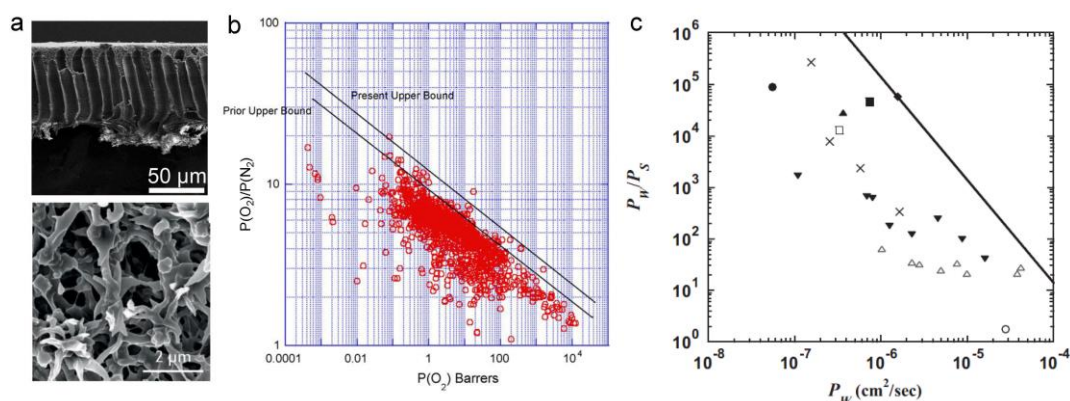


**Figure 1.6.** Properties of conventional polymer membranes. (a) Scanning electron microscopy images of porous membranes made by phase inversion: the upper panel is a cross-section of a polysulfone membrane with finger-like macrovoids,<sup>25</sup> and the lower panel is a top view of a commercial polyvinylidene fluoride membrane (EMD Millipore, Billerica, MA, USA).<sup>22</sup> (b–c), Permeance and selectivity trade-off relations in polymer membranes: b, O<sub>2</sub>/N<sub>2</sub> separation;<sup>26</sup> c, Water/salt separation.<sup>27</sup> The upper panel of part a is reprinted with permission from ref. 25, Elsevier, and the lower panel is reprinted with permission from ref. 22, Springer Nature. Part b is adapted with permission from ref. 26, Elsevier. Part c is reprinted with permission from ref. 27, Elsevier.

Moreover, the synthesis of polymer membranes by phase inversion or interfacial polymerization<sup>22</sup> usually results in a selective layer with thickness of 100 nm to several μm, which generates a high membrane resistance and hence a need for high pressure to

achieve a sufficient flux. This further gives rise to high energy consumption and requires high mechanical stability.<sup>28</sup> To address this issue, several attempts have been made in order to reduce the thickness of the selective layer of polymer membranes, and significant progresses have been achieved by reforming the synthesis process of thin-film composite (TFC) membranes with interfacial polymerization (**Figure 1.7**). A conventional way to fabricate TFC membrane is preparing a dense polyamide film on a porous membrane support through interfacial polymerization of a diamine with a triacyl chloride.<sup>2</sup> The polyamide film serves as the selective layer and dominates the membrane resistance. In the polymerization process, the porous support is first brought into contact with the aqueous solution containing diamine, then immersed into an organic solution containing triacyl chloride which is immiscible with water. The diamine reacts with triacyl chloride at the water/organic interface to form a polyamide film. As the underlying support has a very rough surface, the polyamide layer must keep a sufficient thickness, usually of 100–500 nm,<sup>22</sup> to assure that the formed film is free of defects.

To overcome this obstacle, Livingston group succeeded in fabricating a sub-10-nm thin polyamide film by using a sacrificial layer of cadmium hydroxide nanostrands.<sup>29</sup> The nanostrand layer is formed on top of a porous support and have a thickness of ~120 nm. The advantage of the nanostrand layer is that this thin film can reduce the surface roughness of the underlying support and produces a very smooth surface for interfacial polymerization, which can eventually generate a thin and defect-free polyamide film. Another pronounced progress is made by McCutcheon and his colleagues by using an electrospraying technique, in which the monomers are deposited directly onto a substrate, where they react to form polyamide.<sup>30</sup> The small droplet size of the monomer solution combined with the low monomer concentrations lead to smoother and thinner polyamide films. The approach allows for control of polyamide thickness down to 4 nm increments and roughness as low as 2 nm.

The aforementioned accomplishments provide possibilities to tailor the thickness of polyamide films in a nanometer scale range. However, the monomers are still arranged in a random order on the support, which inevitably results in an uncontrollable polymerization. Thus the resulting pore size is still not well defined and a trade-off between permeance and selectivity may still exist. To address this issue, materials with controllable molecular architectures which give defined microporosity, are needed.

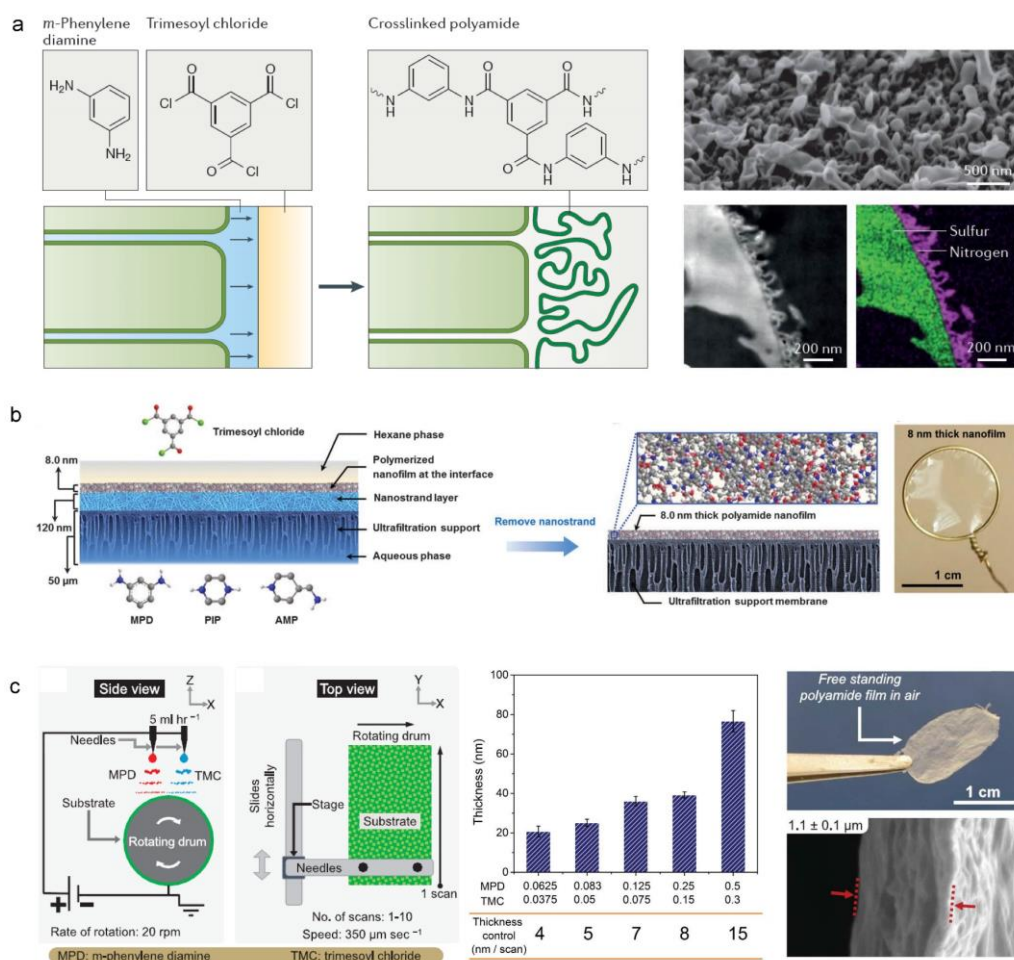


**Figure 1.7.** Thin-film composite membranes made by interfacial polymerization. (a) Polyamide fabricated in a conventional way.<sup>22</sup> (b) Sub-10-nm thin polyamide fabricated with a sacrificial layer of nanostrands.<sup>29</sup> (c) Polyamide fabricated by electrospaying.<sup>30</sup> Panel a is reprinted with permission from ref. 22, Springer Nature. Panel b is reprinted with permission from ref. 29, The American Association for the Advancement of Science. Panel c is reprinted with permission from ref. 30, The American Association for the Advancement of Science.

## 1.4.2 Next-Generation Molecularly Selective Membranes

Recent nanotechnology breakthroughs have led to novel approaches for tailoring of membrane thickness and pore size at a sub-nanometer level, with the precision and flexibility that are not achievable with polymer-based randomized fabrication. Although these nanoconduit devices are still in their infancy and a mass fabrication seems remote, the emerging field of carbon nanofluidics<sup>31</sup> already provides fascinating insights on

materials separation. There are basically two avenues for making membranes with molecular dimensions: bottom-up approach by embedding membrane proteins<sup>32</sup>, carbon nanotubes<sup>33-34</sup> or molecular-sieving fillers (zeolite, metal organic framework)<sup>24,35-36</sup> into supports, and top-down approach by creating artificial pores/channels<sup>5,37-38</sup> with two-dimensional materials.

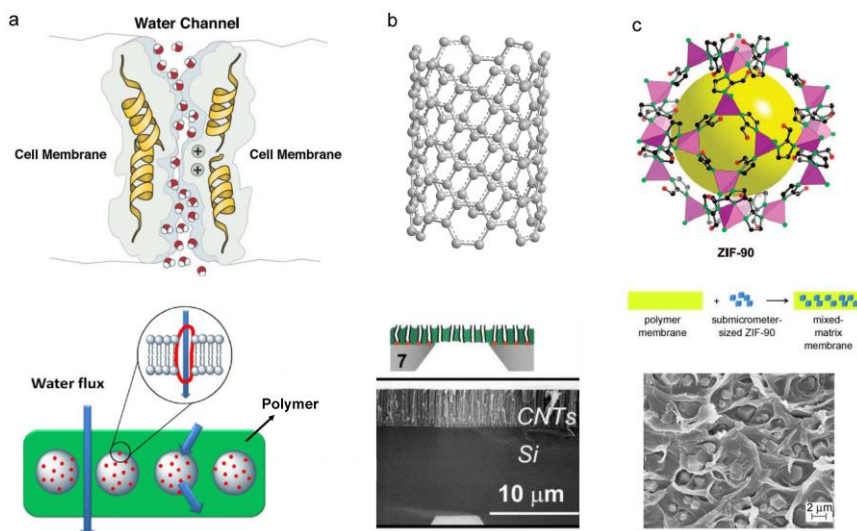


**Figure 1.8.** Bottom-up approach for fabricating molecularly selective membranes. (a) Top, illustration view of water passage through aquaporin;<sup>39</sup> bottom, schematic of aquaporin-based biomimetic membranes.<sup>40</sup> (b) Top, illustration view of CNT structure; bottom, schematic and SEM cross-section view of CNT-embedded membranes.<sup>33</sup> (c) Top, crystal structure of ZIF-90;<sup>41</sup> bottom, SEM cross-section view of mixed-matrix membranes containing ZIF-90 crystals.<sup>42</sup> Part a is reprinted with permission from ref. 40, Elsevier. Part b is adapted with permission from ref. 33, The American Association for the Advancement of Science. Part c is adapted with permission from ref. 41, American Chemical Society, and ref. 42, John Wiley and Sons.

Aquaporin proteins, with a channel size of only  $\sim 0.3$  nm, just wide enough for one molecule,<sup>43</sup> are one of nature's most intelligent inventions, which allow a coordinated transport of water molecules but block all ionic species. Aquaporins have been utilized in water desalination through incorporation into polymer matrices.<sup>40</sup> These nanofilters not only accelerate water flow through polymer-based membranes, but also serve as a barrier that prevents penetration of ions due to interactions of their inner amino groups with ionic species. Inspired by biological channels, carbon nanotubes (CNTs) with

atomically smooth walls are created and promise a frictionless water flow, through which the molecular transport was studied theoretically<sup>44-45</sup> and experimentally.<sup>33-34,46</sup> Like biological channels, CNTs show extraordinary high water flow-rates owing to their smooth interfaces and single-file motions.<sup>33,44-46</sup> The nanotube properties depend on the atomic arrangement of the graphite sheets, and defined by chiral vector and angle.<sup>47</sup> CNTs thus enables a better control over the nanopore geometry. Arrangements of these nanotubes in an optimized manner will gain further unique functionalities. Over the past decades, these artificial nanochannels have encouraged rapid progress in nanopore fabrication,<sup>33,46</sup> however, the challenge has been finding a productive way for vertically aligning the nanotubes to a film over macroscopic scales. Porous solids, such as inorganic zeolites and organic-inorganic hybrid metal organic frameworks (MOFs), are also one of the most intense areas due to their well-defined pore size and shape. These particles are incorporated into polymers as molecular fillers for fabricating mixed matrix membranes. Compared to zeolites, MOFs have a higher degree of tunability in the structures.<sup>48</sup> One of the challenges in pursuing a desired membrane performance has been exploring a highly compatible integration of these additives into polymer matrix with homogeneous dispersions at high loading levels.<sup>24,48</sup>

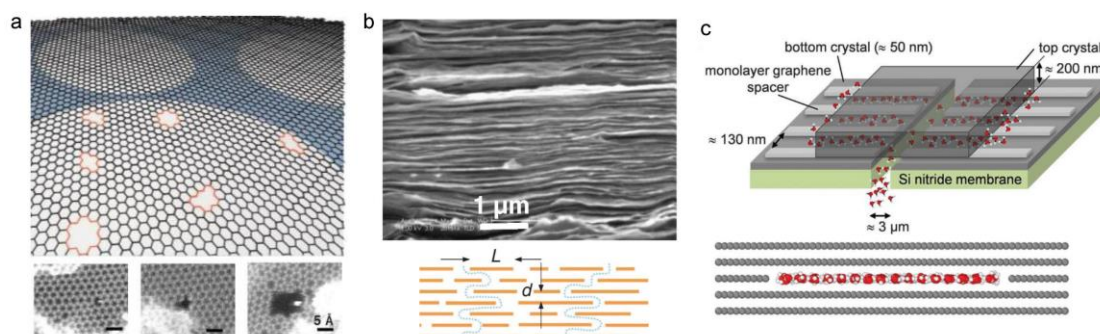


**Figure 1.9.** Top-down approach for fabricating molecularly selective membranes. (a) perforated graphene.<sup>49</sup> (b) graphene oxide membranes.<sup>50</sup> (c) 2D capillary devices made from bulk crystals with graphene as spacers.<sup>51</sup> Part a is reprinted with permission from ref. 49, American Chemical Society. Part b is reprinted with permission from ref. 50, The American Association for the Advancement of Science. Part c is reprinted with permission from ref. 51, The American Association for the Advancement of Science.



In addition to the above nanoporous structures, another significant development is the emergence of two-dimensional (2D) materials which can offer unique electrical, mechanical, optical and thermal properties. A typical example is the thinnest material—single atom thick graphene. Because of the high electron density of its aromatic rings, pristine graphene are impermeable to all molecules.<sup>52</sup> Therefore, graphene sheets have been perforated by ion bombardment with nanometer-size holes in producing a molecular sieve that permits water/ion separation with high selectivity and flow-rate.<sup>5,38,53</sup> However, the stability of the produced nanopores and the scalability of this fabrication technique remains a debate when developing porous graphene. Graphene oxide (GO) is another form of graphene-based membranes. GO also shows low-friction water flow through the confined 2D space between adjacent GO sheets.<sup>54</sup> GO stacks are easily fabricated, but GO membranes swell in water leading to a reduced selectivity.<sup>55</sup> In addition, 2D capillary devices have been created from bulk crystals (such as graphite or hexagonal boron nitride) with graphene stripes as spacers.<sup>51,56</sup> The resulting slit-like channels have atomically smooth surface and little surface charge, which permit frictionless rapid water flow but reject small ionic species such as  $\text{Na}^+$  and  $\text{Cl}^-$ . The channel size can be tailored at an atomic level with the spacers. These devices promise certainly exciting opportunities for fundamental studies but it seems extremely difficult to produce them for real applications.

Overall, these artificial molecular filters provide ultra-fine pores that is controllable at nanometer-dimensions with relatively high throughput. These membranes have been fabricated and tested for various applications, confirming that a better control over the membrane geometry by the nanofabrication techniques can provide extraordinary functionality and performance. However, the aforementioned techniques are complex and unlikely to be easily engineered at a very large scale. Thus, a simple approach for producing scalable thin films with a high density of sub-nanometer channels, still needs to be developed.

### 1.4.3 Carbon Nanomembranes (CNMs)

In addition to graphene, CNMs are another type of 2D materials fabricated by irradiation induced crosslinking of self-assembled monolayers, thus giving the thickness of only single molecule.<sup>57</sup> CNMs are mechanically stable due to the characteristic of crosslinked structures. **Figure 1.10** shows a helium ion micrograph of

a 1-nm-thick CNM freely suspended over a 400  $\mu\text{m}$  wide hexagonal opening. The mechanical properties of membranes are quantified by bulge tests. CNMs made from different molecular precursors exhibit Young's moduli of 10–20 GPa.<sup>58</sup>

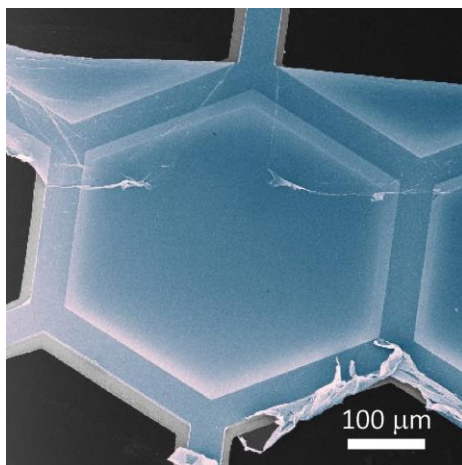


**Figure 1.10.** Helium ion micrograph of a 1-nm-thick freestanding CNM suspended over a 400  $\mu\text{m}$  wide hexagonal opening of a copper grid.<sup>57</sup> Reprinted with permission from ref. 57, John Wiley and Sons.

CNMs mainly comprise carbon, so possess high thermal stability,<sup>59</sup> which allows transformation of the membrane to graphene by pyrolysis.<sup>60</sup> The structural conversion to graphene begins after annealing CNMs at approximately 800 K, which is evidenced by appearance of the characteristic D-, G-, and 2D peaks in the Raman spectra.<sup>61-62</sup> Another special advantage of CNMs is that the membrane structure may be tuned by selection of precursor molecules with varied length and shape (**Figure 1.11**).<sup>63</sup> The membrane thickness is associated with the precursor length and the molecular packing density. “Linear” shaped precursors tend to build a relatively “dense” film, while “bulky” precursors likely form a nanoporous CNM. Moreover, both surfaces of the membrane can be functionalized by selecting precursors with designed chemical groups.<sup>64</sup> The potential tunability integrating with the ease fabrication would grant CNMs a privilege in membrane engineering and upscaling compared with other existing 2D materials.

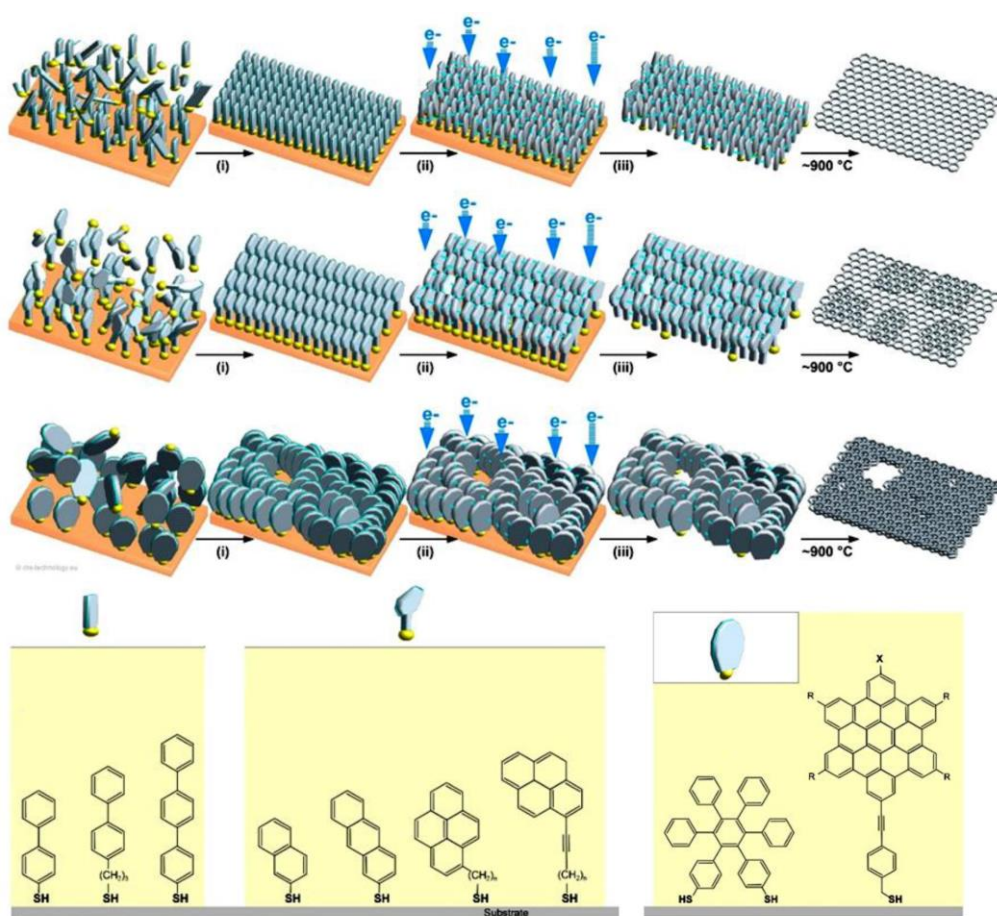


**Figure 1.11.** Fabrication of CNMs from different precursor molecules.<sup>63</sup> The graph is adapted with permission from ref. 63, American Chemical Society.

Despite being only one nanometer thick, CNMs are transferrable to almost any surface with the assistance of PMMA coatings.<sup>62</sup> The membrane forms a tight adhesion to new surfaces by van der Waal forces.<sup>65</sup> The membrane is flexible enough to follow the morphology of the underlying substrate. This allows us to test the performance of CNMs on another supporting substrate, or even in a freestanding manner. So far, the charge transport through CNMs<sup>66</sup> and the mechanical properties<sup>58</sup> have been studied. As the membrane also holds great potential as a candidate for energy-efficient molecular separations, unraveling the permeation properties of CNMs has become especially important. Ai *et al.* first attempted to investigate the permeation behaviour of CNMs by transferring the membrane onto polymer substrates. They found that polymer-supported CNMs could separate small molecules (He, H<sub>2</sub>) from larger ones (O<sub>2</sub>, N<sub>2</sub>).<sup>67</sup>

A resistance model was employed to extract the permeation properties of bare CNMs, however, the presence of the polymer support still hampered an uncovering of mechanisms.

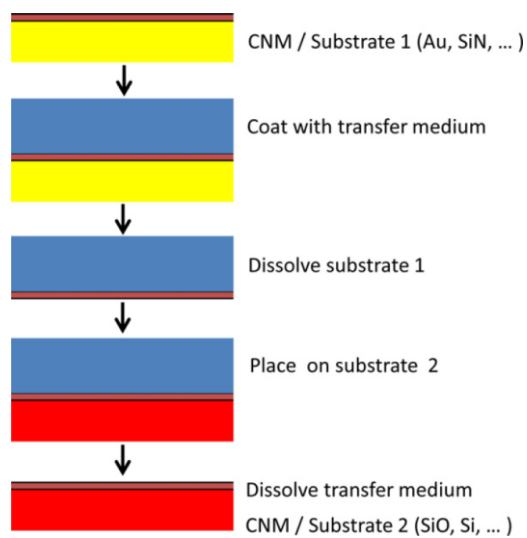


**Figure 1.12.** Transfer CNMs to another substrate.<sup>68</sup> Reprinted with permission from ref. 68, Elsevier.

## 1.5 Motivation and Organization of the Thesis

This work aims to investigate mass transport through freestanding CNMs, eliminating the interference from underneath supports, so as to explore the fundamental permeation properties of CNMs.

Chapter 2 will introduce the basic knowledge of creating CNMs from self-assembled monolayers (SAMs), as well as principles of main methodologies that are employed for characterizing membrane structures and properties.

Chapter 3 will present firstly fabrication of CNMs from a new molecular precursor. This part will introduce the experimental steps involved in developing a protocol, including how to prepare a well-organized SAM, as well as determining a successful conversion of SAMs into CNMs. Afterwards, this new type of membrane will be compared with another CNM made from a linear precursor TPT with an already established fabrication procedure. Finally, the possibility of making stable micrometer-scale freestanding CNMs from the two precursors will be discussed.

Chapter 4 will investigate the single gas and liquid transport through freestanding TPT CNMs by two different permeation experiments. The acquired permeance is compared with the state-of-the-art values. The architecture of TPT CNMs is re-investigated with a high-resolution atomic force microscopy operated in ultrahigh vacuum system. Single-channel permeation coefficient is estimated from the microscopy imaging and the permeance values. The mechanism of molecular transport through CNMs will be discussed.

In Chapter 5, ion transport across TPT CNMs is investigated by electrochemical techniques using both DC and AC methods. The ion diffusion resistance through CNMs and the single-channel ion conductance is extracted from the measured values and compared with that of biological systems. The ion exclusion mechanism by CNMs will be discussed.

Chapter 6 draws final conclusions of the thesis and gives outlooks for future work.



## Chapter 2

### Basics and Methodology

#### 2.1 Fabrication of CNMs from SAMs

##### 2.1.1 SAM Formation

The preparation of CNMs starts from a well-ordered and densely-packed self-assembled monolayer (SAM). The thickness, architecture and surface properties of the membranes are determined from the characteristics of the precursor molecules and their packing density on the surface. SAMs are created by chemisorption of organic molecules with specific “head groups” onto a substrate (**Figure 2.1**). The commonly used head groups include  $-\text{SH}$ ,  $-\text{OH}$ ,  $-\text{SiCH}_3$ , etc., and substrates are Au, Ag, Si, etc.<sup>68-69</sup> In this thesis, gold is employed as the substrate and aromatic thiols as precursors for SAM synthesis.

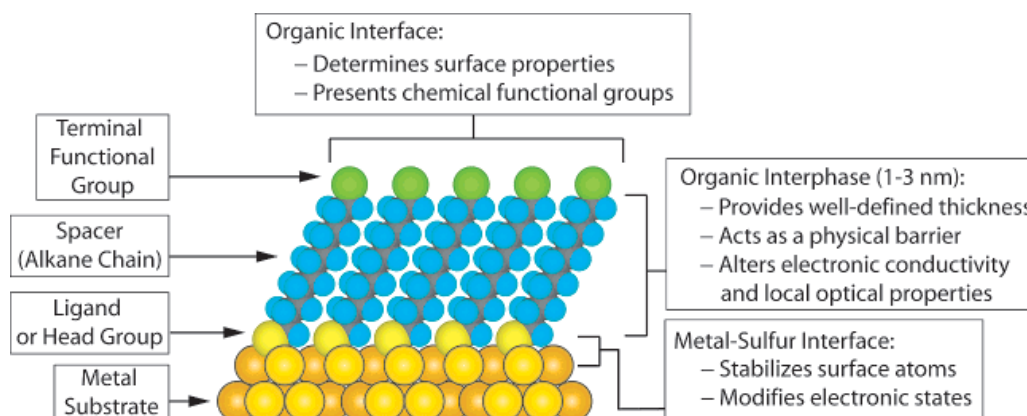


**Figure 2.1.** Schematic illustration of a self-assembled monolayer (SAM) formed from alkanethiolates on an Au(111) surface.<sup>69</sup> Reprinted with permission from ref. 69, American Chemical Society.

Selection of gold as substrates is due to its unique advantages.<sup>69</sup> First, gold is the noblest and the least reactive metal towards atoms or molecules at the interface with a gas or a liquid;<sup>70</sup> Second, a thin gold film can be readily produced by techniques, such as physical vapor deposition, sputtering, electrodeposition, etc.; Third, gold are common substrates used for spectroscopies and other analytical techniques.

The gold substrate tends to adsorb aromatic thiols RS–H because the adsorbates lower the interfacial free energy.<sup>71</sup> But how the thiols bind to gold surfaces to form a SAM remains an open question so far. One of the proposed reaction pathways is that the RS–H thiols are converted, via a dissociative adsorption, to RS–Au thiolates.<sup>72</sup> The adsorption comprises three main steps:

(i) cleavage of the RS–H bond (the bond dissociation energy  $\Delta H = 87 \text{ kcal}\cdot\text{mol}^{-1}$ ),<sup>73</sup>



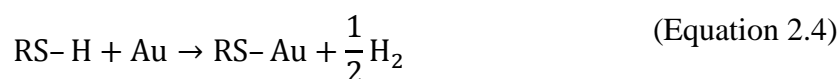
(ii) formation of the RS–Au bond ( $\Delta H = 40 \text{ kcal}\cdot\text{mol}^{-1}$ ),<sup>74</sup>



and (iii) recombination of free hydrogen radicals as  $\text{H}_2$  ( $\Delta H = 104 \text{ kcal}\cdot\text{mol}^{-1}$ ),<sup>73</sup>



According to these bond dissociation energies, the overall enthalpy change of the reaction is calculated to be  $-5 \text{ kcal}\cdot\text{mol}^{-1}$ , which suggests an exothermic adsorption process.



In addition to enthalpic contributions to the reaction, the entropy also plays a non-negligible part and is necessarily to be considered. The thermodynamics of the self-assembling process can be presented by a Gibbs free energy  $\Delta G$ :

$$\Delta G = \Delta H - T\Delta S \quad (\text{Equation 2.5})$$

where  $\Delta H$  is the enthalpy change of the process,  $\Delta S$  is the change in entropy associated with the arrangement of randomly distributed molecules into a well-defined and organized structure, which thus leads to a decrease in entropy.



An *in-situ* detection of a alkanethiol monolayer formation on gold surface reveals that the  $\Delta G_{ads}$  of the process is around  $-5.5 \text{ kcal}\cdot\text{mol}^{-1}$ ,  $\Delta H_{ads}$  is  $-20 \text{ kcal}\cdot\text{mol}^{-1}$ , and  $\Delta S_{ads}$  is  $-48 \text{ cal}\cdot\text{mol}^{-1}\cdot\text{K}^{-1}$ .<sup>72</sup> Hence, a spontaneous SAM formation results from a compromise achieved between the enthalpic and entropic contribution to the adsorption process.<sup>69,72</sup> The Au–S interaction drives the molecular assembly to the limiting status, and the lateral interaction between the adjacent molecules promotes a secondary organization of the molecules which establishes the fine details of the final superlattice structure.<sup>69</sup>

### 2.1.2 Crosslinking of SAMs

Exposure of aromatic SAMs to electrons<sup>75</sup> or UV light<sup>76</sup> could induce the cleavage of C–H bonds and consequently creation of new C–C bonds, which eventually leads to a lateral cross-linking of the monolayer into a 2D film. In this thesis, conversion of SAMs into CNMs is achieved by using an electron flood-gun in a high vacuum ( $<3\times 10^{-7}$  mbar) and employing 100 eV electrons and a dose of  $50 \text{ mC}/\text{cm}^2$ .

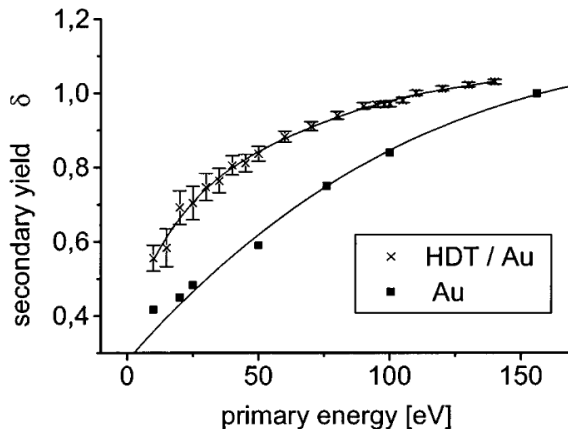


**Figure 2.2.** The secondary electron yield as a function of the primary energy for a hexadecanethiol (HDT) monolayer on a gold substrate.<sup>77</sup> Reprinted with permission from ref. 77, AIP Publishing.

The electron emission source is a thermionic emitter, which utilizes a thermal energy to overcome the work function of a metal filament, and induce an electron flow from the metal surface. When the electron beam impinges upon a sample surface, electrons

within the material may acquire sufficient kinetic energy to be emitted from the surface. The bombarding electrons are called primary, and the emitted electrons are named secondary. The secondary electron yield  $\delta$  is defined as follows:

$$\delta = I_s/I_p \quad (\text{Equation 2.6})$$

where  $I_s$  and  $I_p$  are the currents of the emitted secondary electrons and the primary beam, respectively. A relationship between  $\delta$  and the primary energy was acquired by measuring the primary and the sample currents.<sup>77</sup> In the primary energy region of 100 eV,  $\delta$  reaches up to 1.0 for a hexadecanethiol monolayer on a gold substrate (**Figure 2.2**). Spectroscopic studies suggest that the primary and secondary electrons both contribute to the electron-induced crosslinking in aromatic SAMs.<sup>78</sup> The basic steps involved in crosslinking of a biphenylthiol SAM is schematically shown in **Figure 2.3**, which includes irradiation, emission of secondary electrons, cleavage of C–H bonds, and lateral linking of adjacent molecules.<sup>78</sup>

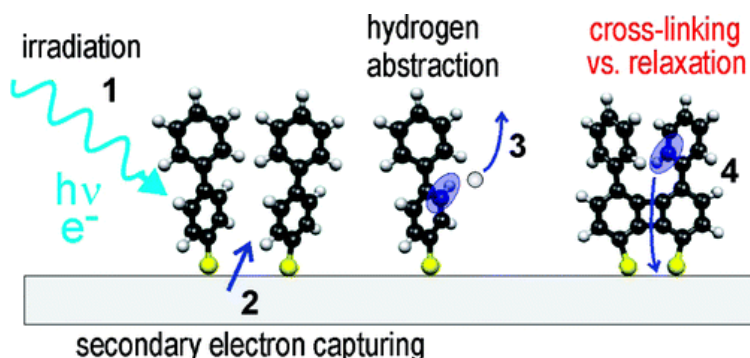


**Figure 2.3.** Schematic representation of four main steps involved in the cross-linking of biphenylthiol SAMs.<sup>78</sup> Reprinted with permission from ref. 78, American Chemical Society.

## 2.2 Characterization of SAMs and CNMs

The chemical composition and thickness of CNMs are characterized with X-ray photoelectron spectroscopy. The intermolecular distance and packing density of the molecules, as well as the membrane architecture are investigated with scanning tunneling microscopy and atomic force microscopy. The membrane intactness is

examined by Helium ion microscopy to exclude defects larger than 1.5 nm. Ion transport through CNMs are characterized by electrochemical impedance spectroscopy.

### 2.2.1 X-ray Photoelectron Spectroscopy (XPS)

XPS was performed using an Omicron Multiprobe system with a base pressure of  $\sim 10^{-10}$  mbar. The system consists of a monochromatic X-ray source (Al  $K\alpha$ ) and a hemispherical electron analyzer (SPHERA). XPS were measured with a photoelectron emission angle of  $\sim 13^\circ$ . The spectra were analyzed using the CasaXPS program.

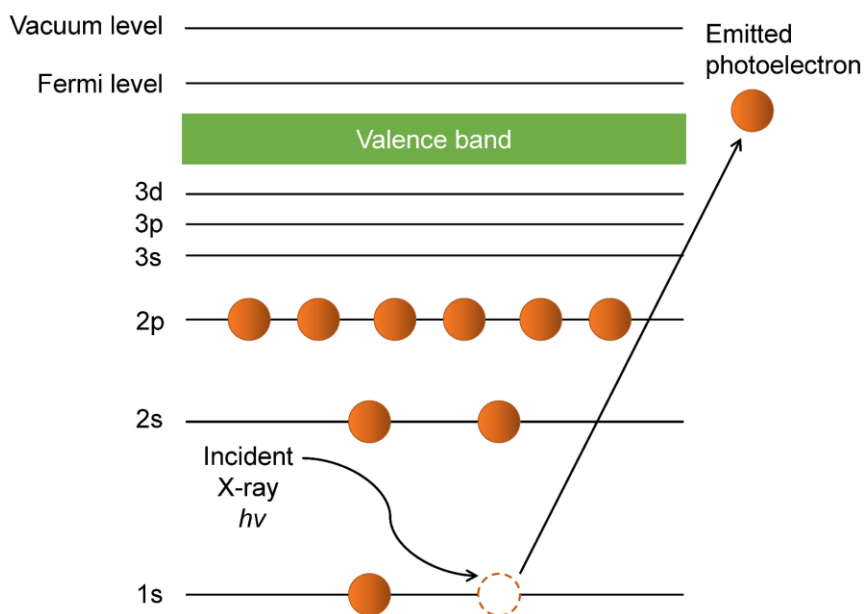


**Figure 2.4.** Schematic illustration of X-ray photoemission process.

When a X-ray beam with photon energies of  $h\nu$  impinges on a surface, electrons can be ejected from the atoms within the material.<sup>79</sup> By measuring the kinetic energy ( $KE$ ) of the emitted electrons, the binding energy ( $BE$ ) of the electron can be determined.

$$BE = h\nu - KE - \Phi \quad (\text{Equation 2.7})$$

where  $h$  is Planck's constant,  $\nu$  is the frequency,  $\Phi$  is the work function of the spectrometer and the material. The obtained BE is related to the elements and their chemical states. The intensity of photoelectron peak relies on the elemental

concentration on the surface. Thus, XPS allows a quantitative determination of the chemical composition of the material surface.

The thickness  $d$  of the monolayer can be determined from the attenuation of the substrate Au4f<sub>7/2</sub> signal according to:<sup>79</sup>

$$I_d = I_0 e^{-\frac{d}{\lambda \cos \theta}} \quad (\text{Equation 2.8})$$

where  $I_0$  and  $I_d$  are XPS signals from the clean and film-covered substrate, respectively,  $\lambda$  is the attenuation length of Au4f<sub>7/2</sub> photoelectrons, which was taken to be 36 Å,<sup>76</sup>  $\theta$  is the emission angle.

### 2.2.2 Scanning Tunneling Microscopy (STM)

The STM image was obtained in a constant current mode by using a multi-chamber UHV system (Omicron) with a base pressure of  $5 \times 10^{-11}$  mbar. The measurement was operated at room temperature. The tunneling tip was prepared by electrochemical etching (3 mol·l<sup>-1</sup> NaOH solution) of a tungsten wire and further processed in situ by sputtering with Ar<sup>+</sup> ions ( $p_{Ar} = 3 \times 10^{-10}$  mbar,  $E = 1$  keV,  $t = 1-2$  min).

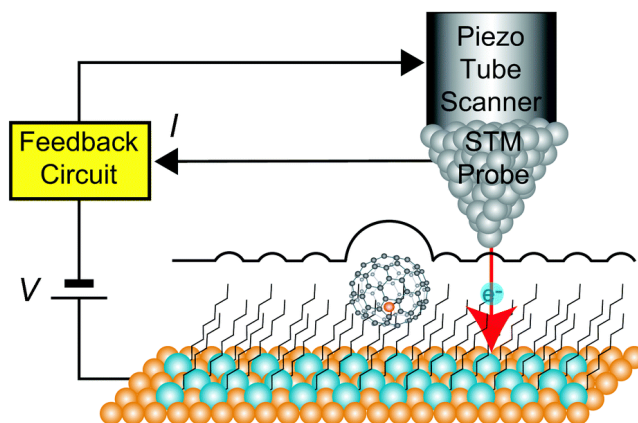


**Figure 2.5.** Schematic illustration of scanning a metallofullerene and alkanethiol SAM on Au(111) by STM in a constant-current mode.<sup>80</sup> Reprinted from Ref. 80.

The atomic resolution of STM is based on a quantum tunneling mechanism. When an atomically sharp tip moves sufficiently close to a surface with a distance of 3–10 Å,

applying a bias voltage  $V_t$  between the tip and the surface can generate a tunneling current through the vacuum.<sup>81-82</sup> The current results from an overlap between electronic wave functions of the tip and the surface, which decays exponentially with the increase of the gap.

When the applied voltage  $V_t$  is compared to the work function  $\phi$  of the two surfaces, the tunneling current  $I_t$  can be expressed in a following relationship:<sup>83</sup>

$$I_t = I_0 e^{-2kd} \quad (\text{Equation 2.9})$$

where  $I_0$  is a function of the applied voltage and density of states in both tip and sample,  $d$  is the distance between two surfaces,  $k = (2m\phi)^{0.5}/\hbar$ , where  $m$  is the mass of the electron, and  $\hbar$  is the reduced Planck's constant.

### 2.2.3 Atomic Force Microscopy (AFM)

The AFM images of TPT SAM and CNM were acquired using a RHK UHV 7500 system ( $5 \times 10^{-11}$  mbar) with R9 controller. The measurements were conducted at 93 K using a liquid nitrogen flow cryostat. The AFM tips were sputtered with  $\text{Ar}^+$  ions at 680 eV for 90 s. For the AFM images, Tap300Al-G force sensors ( $\sim 40 \text{ N}\cdot\text{m}^{-1}$ ,  $\sim 280 \text{ kHz}$ ,  $Q \sim 10000$ , Budget Sensors) were used.

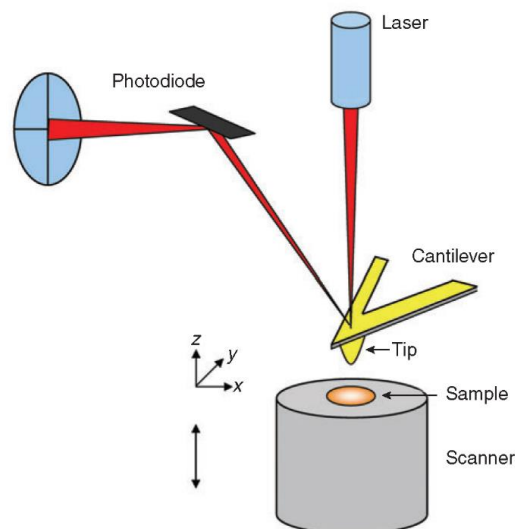


**Figure 2.6.** Schematic view of the principle of AFM.<sup>84</sup> Reprinted with permission from ref. 84, Springer Nature.

The principle of AFM is schematically shown in **Figure 2.6**. A sharp tip attached to a cantilever is utilized to scan over a surface. When the tip approaches the surface to a close proximity, the tip–sample interaction force leads to a deflection of the cantilever. In a typical beam-deflection AFM, a laser beam is used to track the bending of the cantilever, and the changes on the reflected beam is detected by a position-sensitive photodetector.

According to Hooke’s law, the interaction force  $F$  can be determined from the cantilever deflection  $x$ :

$$F = -kx \quad (\text{Equation 2.10})$$

where  $k$  is the spring constant of the cantilever.

In addition, the interaction force as a function of the separation distance  $d$  between the tip and the sample can be described by a Lennard-Jones potential  $V_{LJ}(d)$  function.<sup>85</sup>  $V_{LJ}(d)$  is commonly interpreted as a sum contribution of the Pauli repulsion and the attractive Van der Waals force.

$$V_{LJ}(d) = 4\varepsilon\left[\left(\frac{\sigma}{d}\right)^{12} - \left(\frac{\sigma}{d}\right)^6\right] \quad (\text{Equation 2.11})$$

where  $\varepsilon$  is the depth of the potential well,  $\sigma$  is the finite distance at which the inter-atomic potential is zero,  $d$  is the tip–sample separation distance. The net force  $F(d)$  can be determine from  $V_{LJ}(d)$ :  $F(d) = \partial V_{LJ}(d) / \partial d$ .

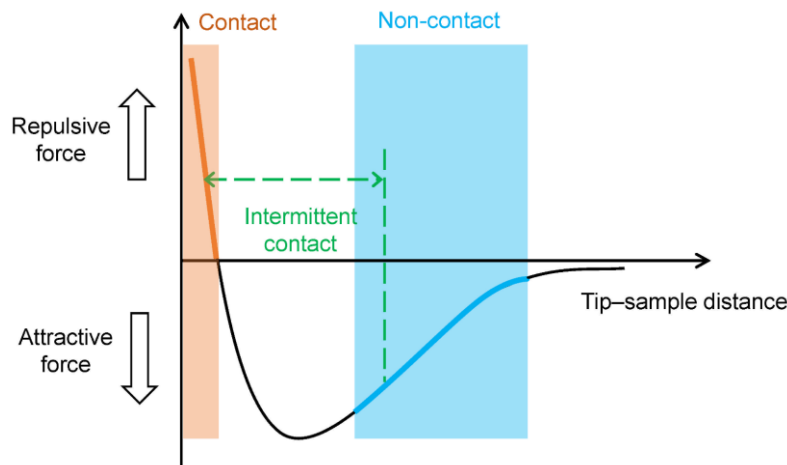


**Figure 2.7.** The tip–sample interaction force as a function of the distance.<sup>86</sup>

At relatively large distances, the attractive Van der Waals force dominates the interaction. When the distance decreases, short-range repulsive forces arise due to the overlap of electron orbitals. According to the force–distance curves shown in **Figure 2.7**, the AFM can be principally classified into two operation modes: static mode (contact mode) and dynamic mode (non-contact and intermittent contact mode).

#### 2.2.4 Helium Ion Microscopy (HIM)

The HIM images were acquired in secondary electron or bright-field ion transmission mode with a Zeiss ORION Plus Helium Ion Microscope. The microscope was operated at a beam energy of 35 keV and an ion beam current of 1 pA. Charges on the sample were neutralized by using a build-in electron floodgun for avoiding charge-induced ruptures.

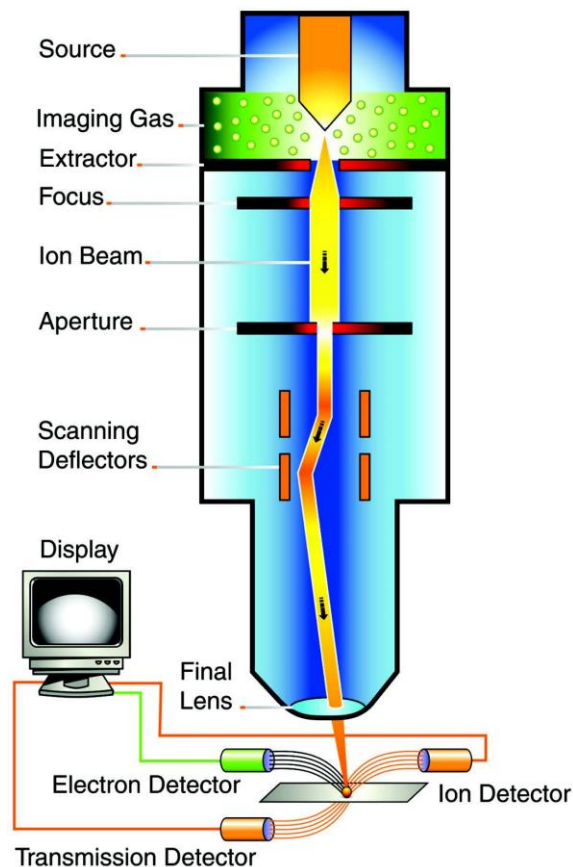


**Figure 2.8.** Schematic representation of HIM.<sup>87</sup> Reprinted with permission from ref. 87, AIP Publishing.

The ion source in HIM consists of a very sharp needle with a tip ending with only three atoms referred as a trimer. Applying a high voltage of 5–30 kV on the tip in a helium atmosphere leads to a field ionization of the He atoms. The He ions are instantly accelerated away from the tip and focused on a sample surface. Upon interactions with the sample, secondary electrons are ejected from the sample and are collected by a detector. A raster scan across the sample with the ion beam builds an image of the surface.

Compared to traditional Scanning Electron Microscope (SEM), HIM have several advantages.<sup>87-88</sup> First, helium ions have a ~100 times shorter wavelength than electrons, thus HIM can provide a smaller spot size than SEM. Second, achieving a similar contrast, a helium ion beam have a smaller interaction volume in the sample than an electron beam. These two specific properties promise a higher resolution and higher surface sensitivity by HIM than SEM. Moreover, HIM allows a high resolution imaging of insulating surfaces without additional modification with gold particles. The positive charge built up on the surface can be neutralized with an electron gun.

## 2.2.5 Electrochemical Impedance Spectroscopy (EIS)

### 2.2.5.1 Concept of EIS

The electrical resistance  $R$  of an ideal resistor is interpreted by the Ohm's law:

$$R = \frac{V}{I} \quad (\text{Equation 2.12})$$

where  $V$  and  $I$  is the voltage and current across the object.

However, the real system contains more complex electrical elements and behaviors. Impedance extends the simple concept of resistance to AC circuits and measures the ability of a circuit to resist the flow of electrical current.<sup>89</sup> The EIS experiments are conducted by applying a small amplitude of sinusoidal signal, e.g., potential  $V_t$ , and measuring the response current  $I_t$ .

$$V_t = V_0 \sin(\omega t) \quad (\text{Equation 2.13})$$

where  $V_t$  is the voltage at time  $t$ ,  $V_0$  is the amplitude of the signal, and  $\omega$  is the radial frequency (rad/s),  $\omega = 2\pi f$ ,  $f$  is frequency expressed in Hz.



$$I_t = I_0 \sin(\omega t + \varphi) \quad (\text{Equation 2.14})$$

where  $\varphi$  is the phase shift between the voltage and the current.

Accordingly, the impedance can be expressed in an Ohm's law-like relationship:

$$Z = \frac{V_t}{I_t} = \frac{V_0 \sin(\omega t)}{I_0 \sin(\omega t + \varphi)} = Z_0 \frac{\sin(\omega t)}{\sin(\omega t + \varphi)} \quad (\text{Equation 2.15})$$

Thus, the impedance spectrum describes not only the magnitude  $Z_0$ , but also the phase shift  $\varphi$ .

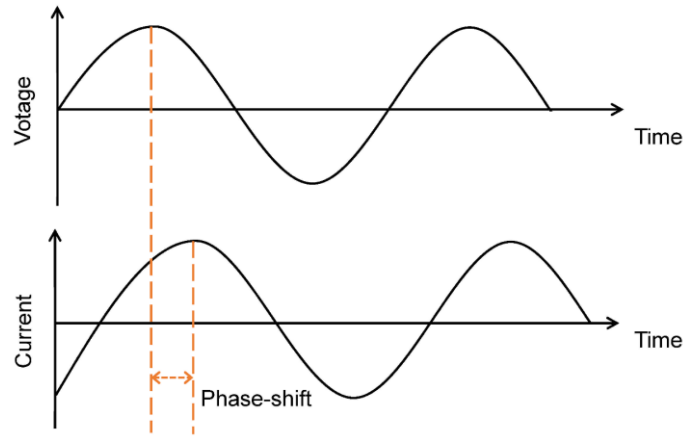


**Figure 2.9.** Sinusoidal Current Response in a Linear System.

In addition, using Euler's formula,

$$e^{j\varphi} = \cos\varphi + j\sin\varphi \quad (\text{Equation 2.16})$$

the impedance can also be expressed in a complex function:

$$Z = \frac{V_t}{I_t} = \frac{V_0 e^{j\omega t}}{I_0 e^{j\omega t - \varphi}} = Z_0 e^{j\varphi} = Z_0 (\cos\varphi + j\sin\varphi) \quad (\text{Equation 2.17})$$

The impedance  $Z$  can now be resolved into two components:  $|Z| = Z_{real} + jZ_{imag}$ , the real component:  $Z_{real} = |Z|\cos\varphi$ , and the imaginary component:  $Z_{imag} = |Z|\sin\varphi$ . The relationship between  $Z_{imag}$  and  $Z_{real}$  can be described by a Nyquist plot. Another representation of the EIS data is Bode plot, which displays the phase shift  $\varphi$  and the

logarithm of absolute value of impedance  $|Z|$  as a function of the logarithm of the frequency  $f$ .

### 2.2.5.2 Interpretation of EIS

The EIS data can be interpreted by fitting to equivalent circuit models. Commonly used electrical elements are resistor, capacitor and inductor. A certain connection of these elements can form various types of circuits. **Figure 2.10** shows Nyquist plots of four common types of equivalent circuit models.

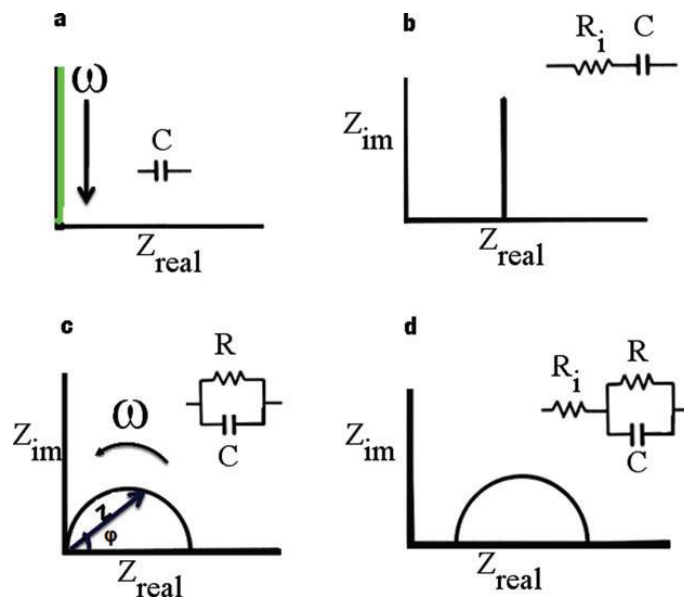


**Figure 2.10.** Nyquist plots for (a) a capacitor, (b) a capacitor in series with a resistor, (c) a capacitor in parallel with a resistor, and (d) a resistor in series with a parallel RC-circuit.<sup>90</sup> Reprinted with permission from ref. 90, Royal Society of Chemistry.

For an ideal resistor, the phase shift is zero, thus  $|Z| = Z_{real} = R$ . The impedance of a resistor is independent of frequency.

The capacitance  $C$  of a capacitor can be determined from the following equation:

$$I_t = C \frac{dV_t}{dt} = C \frac{d(V_0 e^{j\omega t})}{dt} = j\omega C V_0 e^{j\omega t} = j\omega C V_t \quad (\text{Equation 2.18})$$

Hence,

$$Z_{capacitor} = \frac{V_t}{I_t} = \frac{1}{j\omega C} \quad (\text{Equation 2.19})$$

Deduced from Equation 2.19, the impedance of a capacitor decreases when the frequency is increased. The current through a capacitor is phase shifted  $90^\circ$  with respect to the voltage.

In contrast, the inductance  $L$  of an inductor can be determined from the following relationship:

$$V_t = L \frac{dI_t}{dt} = L \frac{d(I_0 e^{j\omega t})}{dt} = j\omega L I_0 e^{j\omega t} = j\omega L I_t \quad (\text{Equation 2.20})$$

Thus,

$$Z_{inductor} = \frac{V_t}{I_t} = j\omega L \quad (\text{Equation 2.21})$$

Accordingly, the impedance of an inductor increases when the frequency is increased. The current through an inductor is phase shifted  $-90^\circ$  with respect to the voltage.

For an inhomogeneous material, of which the physical properties, such as the charge mobilities, are different everywhere, a constant phase element (CPE) is commonly used to describe the capacitive behavior and interpreted as an imperfect capacitor.<sup>89,91</sup> The presence of CPE results in a depressed semicircle in Nyquist plot. The capacitance of a CPE component can be calculated from the following equation:<sup>92</sup>

$$C = \frac{(Y^0 \cdot R)^{1/n}}{R} \quad (\text{Equation 2.22})$$

where  $Y^0$  is the CPE parameter ( $S \cdot s^n$ ),  $R$  is the resistance of the resistor in parallel to the CPE ( $\Omega$ ).



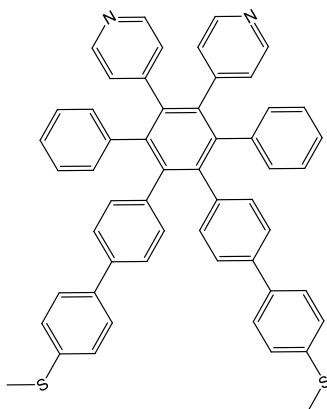
## Chapter 3

### Fabrication of Micrometer-Scale Freestanding CNMs

#### 3.1 Fabrication of CNMs on Au(111)/Mica

##### 3.1.1 CNMs from a New “Bulky” Precursor HPB Derivative 1

The motivation of this work is to seek more available precursors for synthesizing CNMs, which would enrich our understanding on molecular mechanisms of crosslinking in aromatic SAMs, and also build up the precursor systems in exploring the possibility of tailoring the CNM properties. The objective is to develop a protocol for fabricating mechanically stable CNMs from the new precursor HPB derivative **1**. The molecule is synthesized by Max Planck Institute for Polymer Research through a project collaboration.

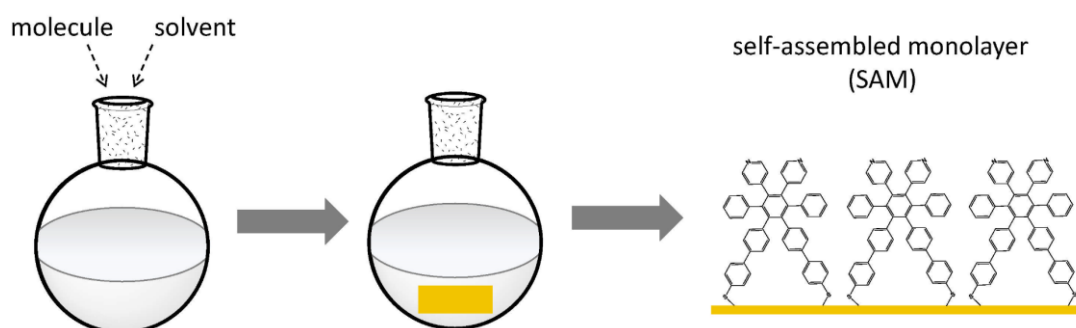


molecular formula:  $C_{54}H_{40}N_2S_2$

molecular length: 15 Å

**Figure 3.1.** Structure of hexaphenylbenzene (HPB) based derivative **1**: 4,4'-(4,4''''-bis(methylthio)-3'',6''-diphenyl-[1,1':4',1'':2'',1''':4''',1''''-quinquephenyl]-4'',5''-diyl)dipyridine.

The structure of the new molecule HPB derivative **1** is shown in **Figure 3.1**. It is a “bulky” molecule containing two pyridine-N in the phenyl rings. Instead of commonly used thiol groups, two thioether groups function as the head groups, which is specially designed to protect sulfur from being oxidized. The procedure for fabricating SAM is illustrated in **Figure 3.2**. First, the molecule is dissolved in a solvent, then a clean Au(111)/mica substrate (G. Albert PVD, Silz, Germany) is immersed in the solution. After a specific reaction time, a SAM is formed and the SAM/Au/mica is taken out from the solution. Optical microscopy, XPS and helium ion microscopy are employed to examine the quality of the formed SAMs and resulting CNMs.

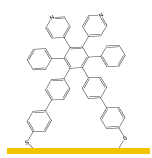
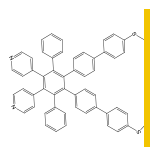


**Figure 3.2.** Schematic illustration of the SAM preparation from HPB derivative **1**.

In order to obtain a well-ordered and densely-packed monolayer, a variety of preparation conditions are investigated as listed in Table 3.1. As a starting step, several common solvents, such as DMF, DMSO,  $\text{CHCl}_3$  and  $\text{CH}_2\text{Cl}_2$ , are tested. It turns out that the molecule can well dissolve in  $\text{CHCl}_3$  and  $\text{CH}_2\text{Cl}_2$ . Subsequently, the concentration of molecules in the solution was tuned. The monolayer thickness appears to be highly related to the molecule concentration. The thickness of SAMs prepared in  $\text{CHCl}_3$  is reduced when the concentration decreases. As the molecules assemble on the surface usually with a tilted angle, the thickness of a densely packed monolayer is supposed to be slightly smaller than the length of the molecule, in this case,  $\sim 1.5$  nm. In addition, when the monolayer is prepared with a high molecular concentration, the obtained sample surface is largely covered with the particles which is even visible to naked eyes. These particles are most likely the physisorbed molecules, as a result of the big mass of the bulky molecules. In contrast, a low concentration results in a low coverage of molecules on the surface, which can be observed from the C1s intensity of XPS spectra,

associated to the monolayer thickness described in Table 3.1. Thus, the “monolayer” with thickness larger than 1.5 nm is ascribed to the physisorbed molecules on the monolayer surface. This is also supported by the observation of a substantial reduction in C1s intensity after exposing these thick “monolayers” to electron beams. The smallest reduction of carbon is achieved with 0.1 mM solution in  $\text{CHCl}_3$ .

**Table 3.1.** Varied conditions for preparing CNMs from HPB derivative 1.

| Solvent                  | $c^*$<br>(mM) | $t^*$<br>(days) | Thickness<br>(Å)** |     | Reduction<br>of carbon | Position of<br>substrates  | Comments                                      |
|--------------------------|---------------|-----------------|--------------------|-----|------------------------|--|---|
|                          |               |                 | SAM                | CNM |                        |  |   |
| $\text{CH}_2\text{Cl}_2$ | 0.3           | 1               | 18                 | 12  | 16%                    |  | Physisorbed<br>molecules<br>on the<br>surface |
|                          |               | 6               | 14                 | 11  | 8%                     |  |   |
| $\text{CHCl}_3$          | 0.6           | 1               | 16                 | 11  | 10%                    |  |   |
|                          |               | 1               | 11                 | 8   | 2%                     |  |   |
|                          |               | 1               | 7                  | 5   | 9%                     |  |   |
|                          |               | 3               | 6                  | -   | -                      |  |   |
| $\text{CH}_2\text{Cl}_2$ | 0.1           | 1               | 11                 | -   | -                      |  | Broader S2p<br>signal                         |
| $\text{CHCl}_3$          |               |                 | 10                 | 8   | 2%                     |  | ✓   |

\* $c$ : concentration,  $t$ : immersion time. \*\*The monolayer thickness is calculated from Equation 2.8.

Immersing the substrate in the solution for one day seems to be sufficient for forming a dense monolayer. Preparation with a longer immersion time did not make a substantial change on the monolayer quality. Moreover, the physisorption of molecules on the surface can be prevented by placing the substrate in a standing-up position instead of lying down. At the same conditions, the monolayer prepared in  $\text{CHCl}_3$  exhibits a narrow S2p signal and a high C1s intensity compared to that prepared in  $\text{CH}_2\text{Cl}_2$ , indicating a high purity of chemisorbed monolayer on the substrate. Finally, a ~1 nm thin SAM from

HPB derivative **1** is created by immersing the Au/mica substrate in 0.1 mM solution  $\text{CHCl}_3$  by a standing-up position for one day at room temperature. After electron irradiation, the monolayer is converted to a  $\sim 0.8$  nm thin CNM.

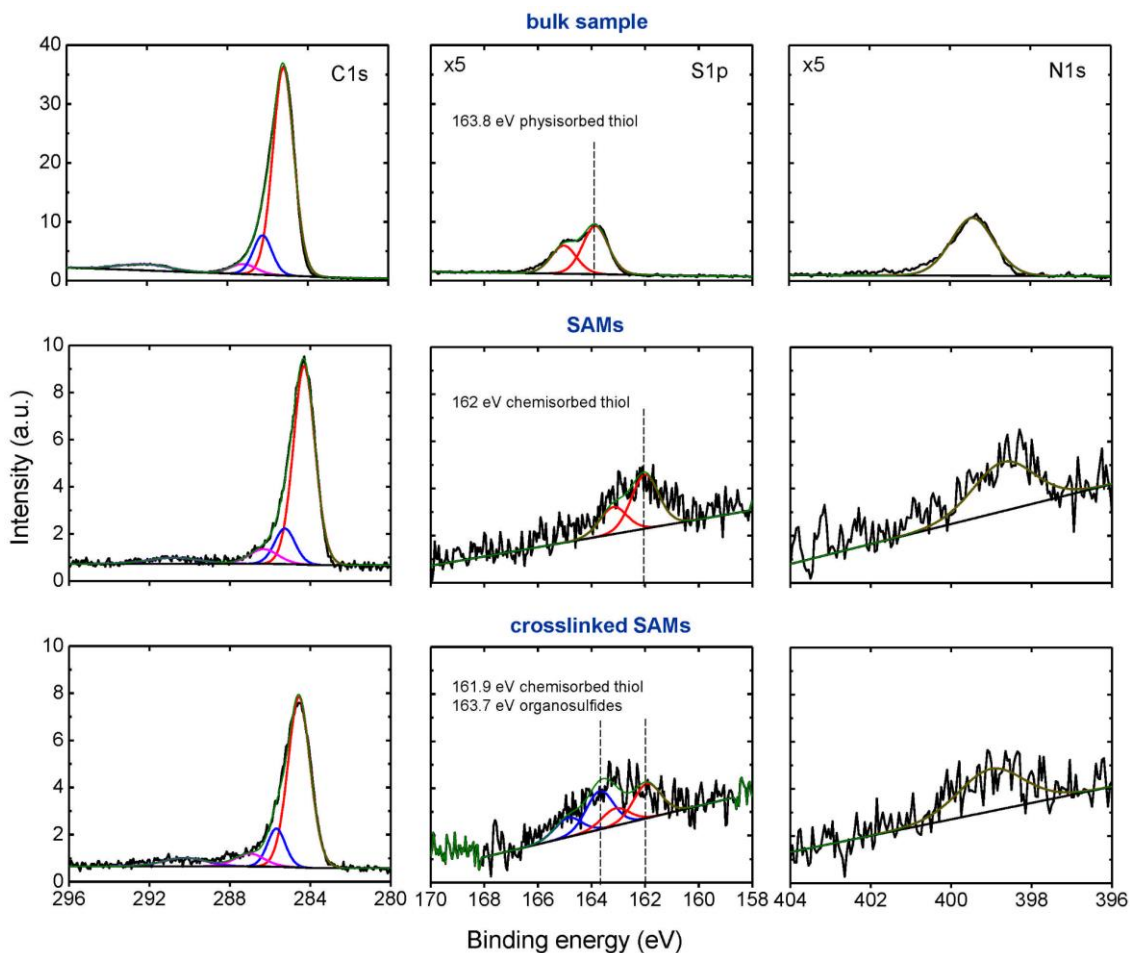


**Figure 3.3.** X-ray photoelectron spectra of the bulk sample, SAM and crosslinked SAM prepared from HPB derivative **1**.

**Figure 3.3** shows the XPS spectra of a bulk sample, SAM and crosslinked SAM made from HPB derivative **1**. The bulk sample was prepared by drop casting a diluted solution of the molecule on the gold surface. Measurements with the bulk sample would be useful in determining the binding energy (BE) of the thioether group on gold in an unbound state. The sulfur signal for the bulk sample consists of a doublet with a  $\text{S}2\text{p}_{3/2}$  BE of  $\sim 163.8$  eV, which is assigned to unbound thiol species on gold.<sup>93</sup> Note that the



BE of the C1s signal for the bulk sample are shifted to higher values compared to that for the monolayer, which is possibly due to a weak electrical coupling of the thick film to the substrate.<sup>94-95</sup> The BE of sulfur signal for the SAM sample shifts to  $\sim 162.0$  eV, attributing to chemisorbed thiol species on gold via RS–Au bonds.<sup>96</sup> The presence of single doublet in the S2p spectra suggests that the two thioether groups in the precursor both chemisorbed on the gold substrate. N1s peaks with BE of 398.6 eV is assigned to pyridinic nitrogen.<sup>97</sup> In the S2p spectrum of the irradiated SAM, in addition to the thiolate species with a Sp3/2 BE of 161.9 eV, another new sulfur species with a Sp3/2 BE of 163.7 eV is observed, which is assigned to organosulfides (R–S–R or R–S–S–R) formed during the crosslinking process.<sup>78,98</sup> The XPS analyses demonstrate that the HPB derivative **1** precursors are successfully bound to the gold substrate and well assembled into a dense monolayer. Irradiation of the monolayer induces successfully a crosslinking of the adjacent molecules.

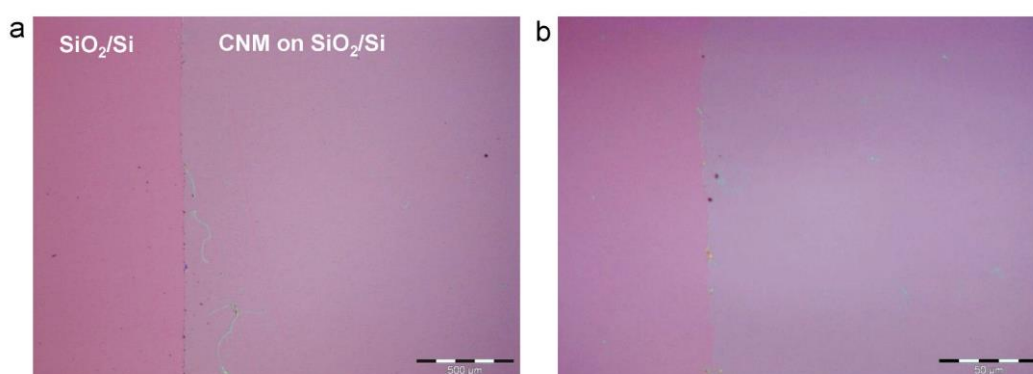


**Figure 3.4.** Optical micrograph of CNMs from HPB derivative **1** transferred on SiO<sub>2</sub>/Si.

The irradiated monolayer, i.e., CNM, is then transferred onto SiO<sub>2</sub>/Si substrates with the assistance of PMMA coatings. The transfer procedure is described elsewhere in detail.<sup>63</sup> The membrane appears as a transparent, homogeneous and dense film on the silicon substrate (**Figure 3.4**). The film is free of nanoscopic holes, according to the HIM imaging of the CNMs that are transferred onto Lacey carbon films/copper grids and quantifoil TEM grids (**Figure 3.5a–b**). The membrane is also mechanically stable enough to be suspended freely over a 40 μm-sized hexagonal opening on copper TEM grids without any supporting films (**Figure 3.5c**).

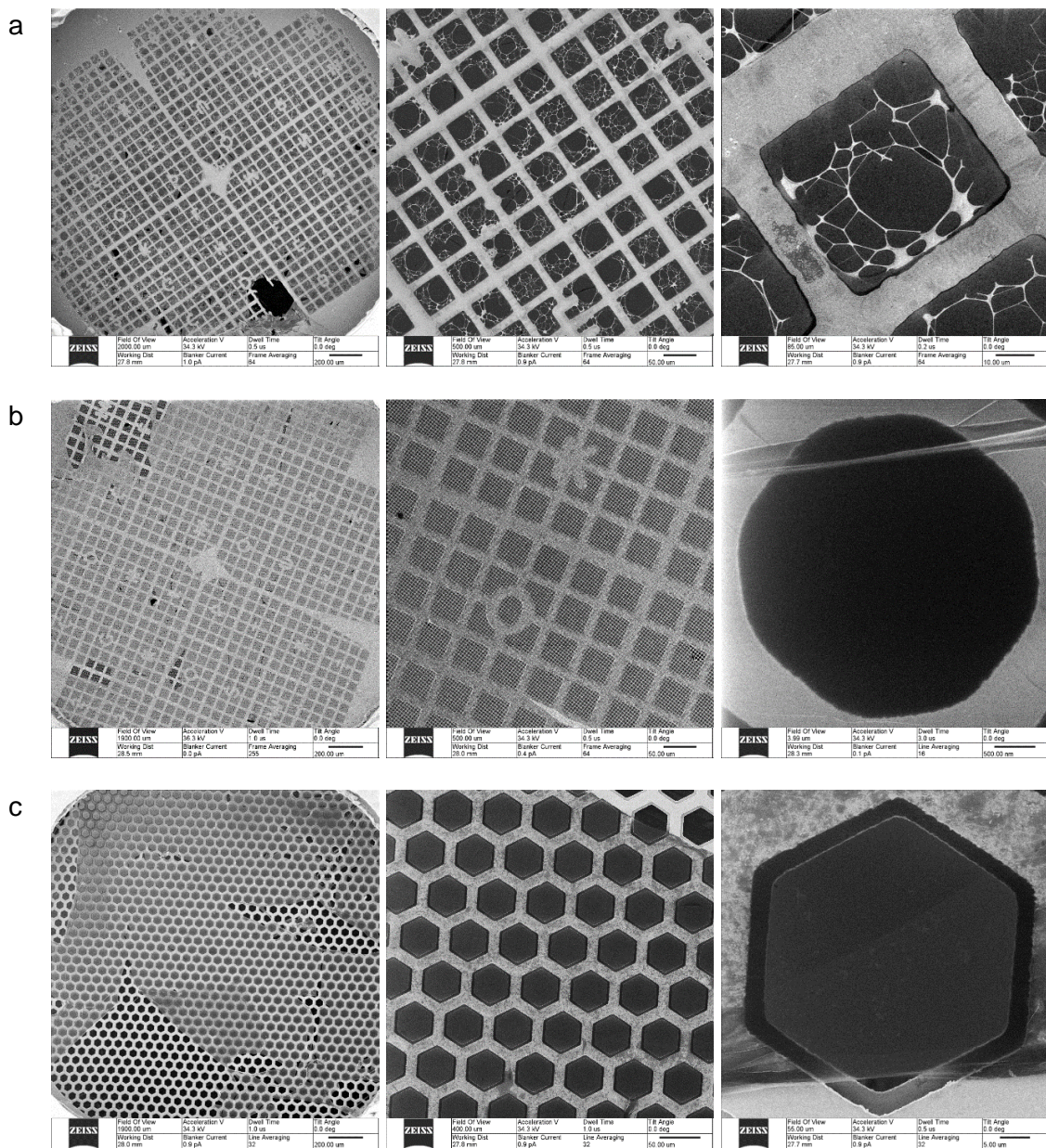


**Figure 3.5.** Helium ion micrograph of the CNMs made from HPB derivative **1** and transferred onto (a) Lacey carbon films on Cu grids, (b) Quantifoil TEM grids, and (c) Cu 400 mesh grids.

### 3.1.2 CNMs from an Established “Linear” Precursor TPT

Fabrication of SAMs from terphenylthiol (TPT) precursors follows a procedure described elsewhere.<sup>63</sup> The length of the TPT molecule is ~1.5 nm. Determined from XPS analysis, the carbon content of the monolayer was only reduced by 2% after electron irradiation with 50 eV electrons at a dose of 50 mC/cm<sup>2</sup>. The resulting CNMs has a thickness of ~1.2 nm, calculated from the exponential attenuation of the Au substrate Au4f7/2 signal (see Equation 2.8).

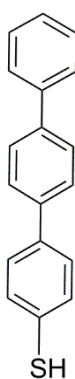


*Figure 3.6. Structure of the precursor terphenyl-4-thiol (TPT).*

The sulfur spectrum of TPT SAM shows a single doublet with a S2p<sub>3/2</sub> BE of 162.0 eV that is attributed to thiolates on gold (R–S–Au).<sup>78</sup> The presence of the single doublet indicates a high quality thiol-derived SAM.<sup>99</sup> After exposing the monolayer to irradiation, a new sulfur species with a S2p<sub>3/2</sub> BE of 163.5 eV is detected which is assigned to organosulfides,<sup>98</sup> suggesting that some sulfur groups no longer bond to gold but form sulfides (R–S–R) or disulfides (R–S–S–R) by linking adjacent molecules.<sup>78,98</sup> The membrane stability was also tested by transferring the CNM from the original gold substrate to a new gold surface. In the C1s spectrum of the transferred sample, the carbon intensity seems to be mostly preserved. Shoulders at 286.5 and 288.7 eV were detected, which may occur as a result of the adsorbed CO<sub>2</sub> and H<sub>2</sub>O during the transfer process. Another possibility is ascribed to the existence of the residue of carbon radicals generated in the crosslinking process. These carbon radicals might get oxidized and converted to oxygen-containing functional groups like carboxyl, after CNMs are taken

out from the vacuum system and exposed to atmospheric condition. The interpretations are supported by the observing of oxygen species on the transferred sample. In addition, the sulfur species of thiolates on gold (S2p<sub>3/2</sub> binding energy of 162 eV) disappeared on the S2p spectrum of the transferred sample. This likely occurs due to the fact that the original gold substrate is etched away during the transfer process.

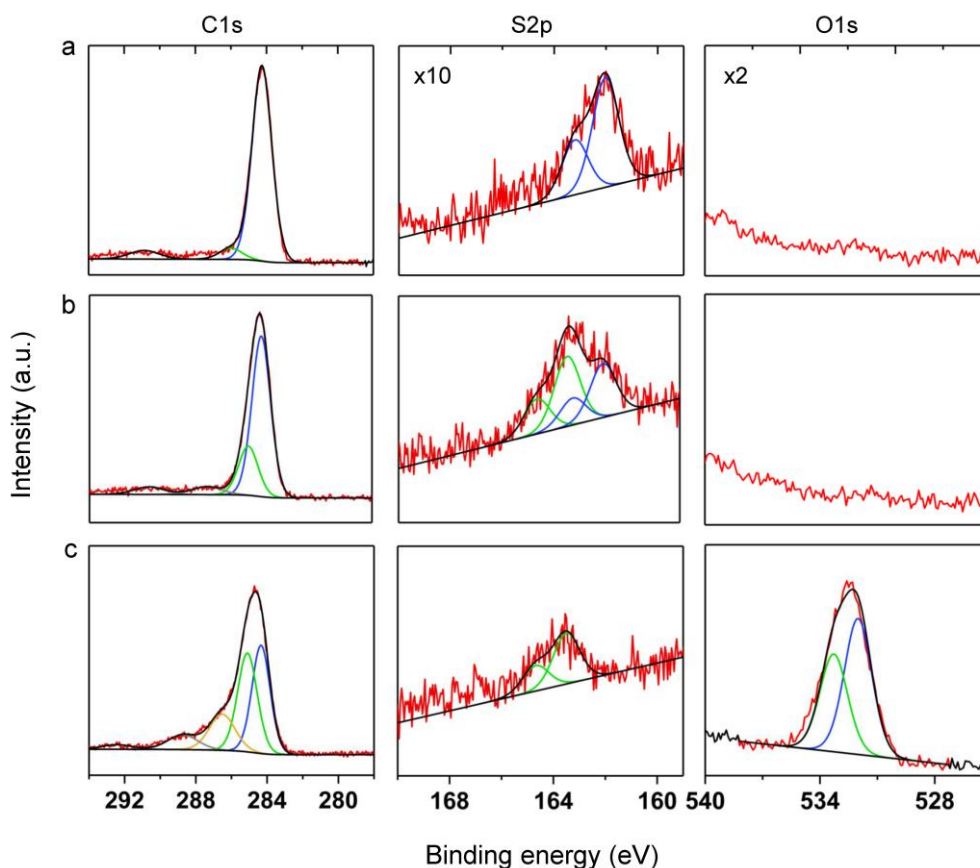


**Figure 3.7.** X-ray Photoelectron Spectra. (a) TPT SAM on Au(111)/mica. (b) TPT CNM on Au(111)/mica. (c) TPT-CNM transferred onto a new Au(111)/mica substrate.

### 3.2 Micrometer-Scale Freestanding CNMs on Si<sub>3</sub>N<sub>4</sub>/Si Chips

The target substrate employed for holding CNMs in permeation measurements is a Si<sub>3</sub>N<sub>4</sub>/Si chip which consists of a 500 nm thick silicon nitride membrane on top of a 200 μm thick silicon supporting frame (Silson Ltd, UK); a circular opening with diameter of 5–50 μm is made in the silicon nitride membrane (**Figure 3.8**). The size of

the opening defines the effective membrane area for permeation experiments. CNMs made from HPB derivative **1** and TPT precursors are transferred onto  $\text{Si}_3\text{N}_4/\text{Si}$  chips respectively, with the assistance of PMMA coatings as described elsewhere.<sup>58</sup>

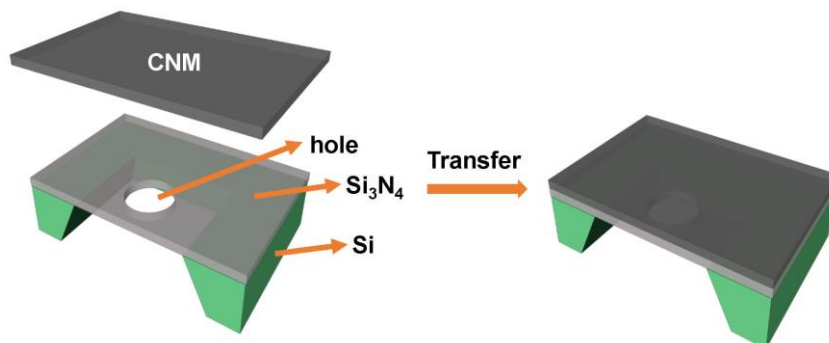


**Figure 3.8.** Schematic illustration of transferring the CNM onto a  $\text{Si}_3\text{N}_4/\text{Si}$  chip device with a single microhole.

The intactness of the transferred CNMs is first examined with optical microscopy, from which the micrometer-sized defects can be readily detected. The yield of intact samples prepared from HPB derivative **1** is found to be only ~30%. Most of the membranes get ruptured during the transfer process (**Figure 3.9**). In comparison, the yield of intact membranes made from TPT precursors is nearly 100%. The freestanding TPT CNMs are further checked with HIM to exclude the existence of nanoscopic defects larger than ~1.5 nm (resolution of HIM). **Figure 3.10** shows optical and helium-ion micrographs of a freestanding TPT CNM that is suspended over a 18  $\mu\text{m}$  circular hole on a  $\text{Si}_3\text{N}_4/\text{Si}$  chip. The membrane appears as a dense film on the substrate and is free of defects/holes visible in the resolution limit of HIM.

The higher yield of intact samples from TPT precursors is possibly due to the fact that CNMs made from TPT are ~0.4 nm thicker than CNMs from HPB derivative **1** and are hence more mechanically stable. The “bulky” shape determines that HPB derivative **1** might not assemble in a monolayer structure as dense as the “linear” precursor TPT does, thus tending to form a thinner membrane, even though the molecular length of the two precursors are similar. On the other hand, the membrane thickness may also be related to the preparation conditions, as indicated in a previous work;<sup>63</sup> for those molecules of which the intermolecular interactions relies on factors, such as temperature

and solvent, the monolayer thickness can be tailored by varying these preparation conditions. As tailoring of the CNM properties is not the focus of this work, optimizing the membrane structures from HPB derivative **1** will not be proceeded here. The CNMs prepared from TPT precursors seem to be sufficiently qualified for further permeation experiments.

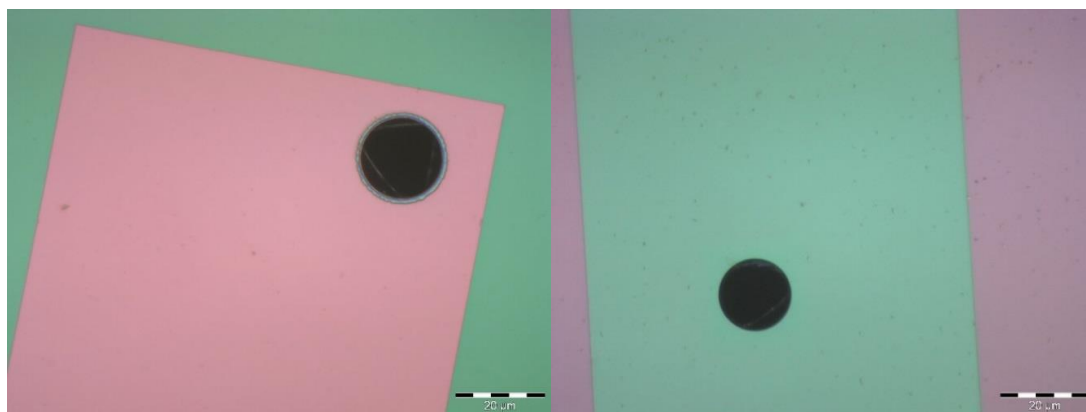


**Figure 3.9.** Optical micrograph of two ruptured CNMs from HPB derivative **1** suspended over a microhole on  $\text{Si}_3\text{N}_4/\text{Si}$  chip.

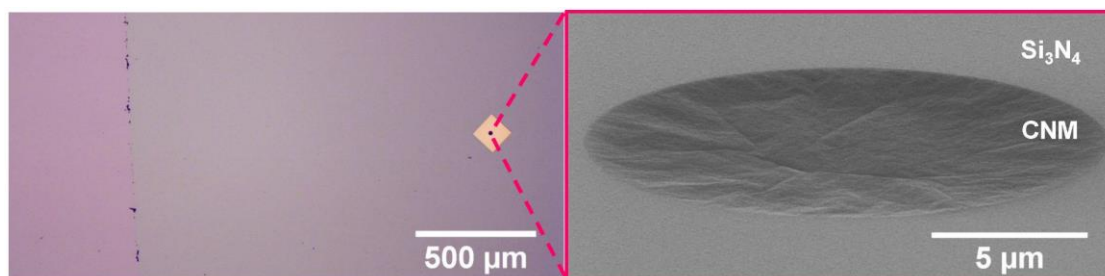


**Figure 3.10.** Optical and helium ion micrographs of a freestanding TPT CNM suspended over a microhole on  $\text{Si}_3\text{N}_4/\text{Si}$  chip. The sample was tilted by  $\sim 75^\circ$  for HIM imaging.

### 3.3 Summary

Two precursor molecules were employed to fabricate micrometer-scale freestanding CNMs. Firstly, a ~0.8 nm thick CNM is fabricated from a new bulky precursor HPB derivative **1**, of which the molecular length is 1.5 nm. The membrane is free of nanoscopic holes, and are mechanically stable enough to be suspended over ~40  $\mu\text{m}$  sized hexagonal openings. In contrast, a linear shape TPT precursor with similar molecular length forms a 1.2 nm thick CNM.

As the first preparing step for permeation experiments, both membranes are transferred from the original gold surface to the target substrate of  $\text{Si}_3\text{N}_4/\text{Si}$  device with a single 15–20  $\mu\text{m}$  sized aperture. The yield of intact samples made from HPB derivative **1** is only ~30%, substantially lower than 100% yield from TPT. We attribute this to the fact that CNMs made from TPT are ~0.4 nm thicker than that from HPB derivative **1** and thus more mechanically stable. A possible way to enhance the yield of intact membranes from HPB derivative **1** would be reducing the freestanding membrane dimension. However, this will also bring down the signal-to-noise ratio in the subsequent permeation experiments. Considering that CNMs are only ~1 nm thick, performing measurements with these thin films is very challenging. Thus, as a starting point, this work will only focus on the transport properties of TPT CNMs, so as to keep a relatively high desired signal in the permeation measurements, as well as minimizing the influence of membrane fractures.





## Chapter 4

# Rapid and Selective Water Permeation Through TPT CNMs

### 4.1 Introduction

In this chapter, molecular transport through freestanding TPT CNMs will be quantified by two different permeation experiments: mass-loss measurements and gas permeation measurements in vacuum system. To understand the permeation behavior, the architecture of TPT CNMs will be re-investigated by high-resolution scanning probe microscopy operated in ultrahigh vacuum system. The transport mechanism through CNMs will also be discussed. The main results of this chapter have been published in a peer-reviewed journal (*ACS Nano* **2018**, *12*, 4695-4701).<sup>100</sup>

### 4.2 Mass Loss Methods

#### 4.2.1 Basics and Setup

The permeation of water and organic liquids through CNMs is studied with a mass loss measurement.<sup>101</sup> The setup is schematically shown in **Figure 4.1**. The CNM covered Si chips are sealed by epoxy on top of a container which is filled with 400  $\mu\text{l}$  of Milli-Q water. The experiment starts in  $\sim 15$  h to make sure that the relative humidity (RH) inside the container achieves up to 100% and the mass loss change of the system reaches a steady state. The container is then placed into an enclosed oven with a constant temperature of  $30 \pm 0.1$  °C and the RH inside the oven (i.e., outside the container) is controlled around  $15\% \pm 2\%$  by using saturated LiCl solution.<sup>102</sup> Due to a differential water vapour pressure inside and outside the container, water will evaporate inside the container and permeate across the membrane. The mass loss of the container is recorded with a microbalance (Sartorius ME36S, sensitivity: 1  $\mu\text{g}$ ).

The water permeance of the CNM can be calculated by the following equation:

$$P = \frac{\Delta m / M}{A \cdot t \cdot \Delta p} \quad (\text{Equation 4.1})$$

where  $\Delta m$  is the mass change of the container (kg),  $M$  is the molar mass of water ( $\text{kg} \cdot \text{mol}^{-1}$ ),  $A$  is the membrane area ( $\text{m}^2$ ),  $t$  is the time interval for an experiment (s),  $\Delta p$  is the vapor pressure difference (Pa). In this study,  $\Delta p$  is around 3,600 Pa.

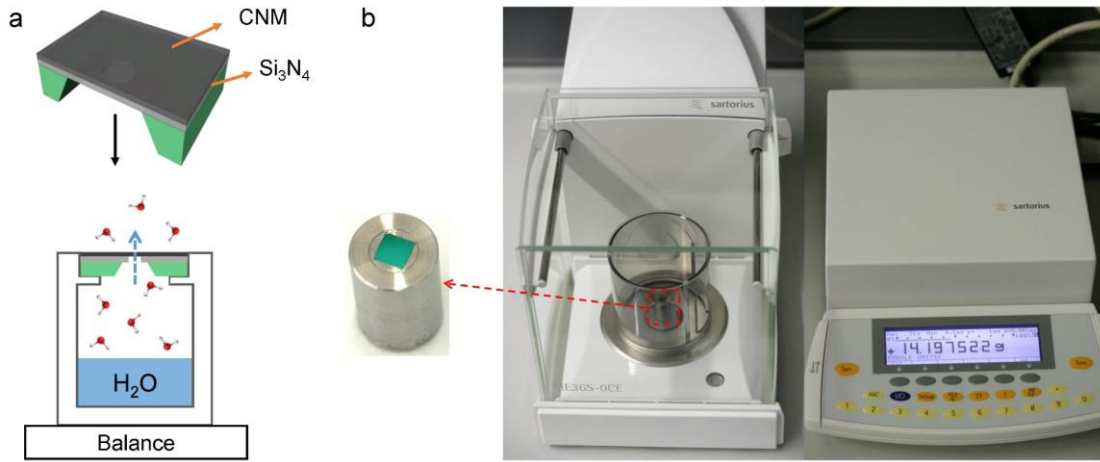


**Figure 4.1.** (a) Schematic view and (b) photograph of the mass loss experiments.

#### 4.2.2 Control Measurements

To confirm the reliability of the method, we first investigated the water flow through an uncovered open aperture. The diffusion of water molecules through a thin orifice can be predicted from the following equation:<sup>56,103-104</sup>

$$Q = D \cdot \frac{m}{K_B T} \cdot d \cdot \Delta p \quad (\text{Equation 4.2})$$

where  $Q$  is the mass flow rate ( $\text{kg} \cdot \text{s}^{-1}$ ),  $D$  is the diffusion coefficient of water in air at  $30^\circ\text{C}$  ( $26 \times 10^{-6} \text{ m}^2 \cdot \text{s}^{-1}$ ),<sup>105</sup>  $m$  is the molecular mass of water (kg),  $K_B$  is the Boltzmann constant ( $\text{m}^2 \cdot \text{kg} \cdot \text{s}^{-2} \cdot \text{K}^{-1}$ ),  $T$  is the temperature (K),  $d$  is the diameter of the aperture (m),  $\Delta p$  is the vapor pressure difference (Pa).

As control measurements, two subsequent experiments are performed respectively as follows. First, the diameter of the aperture is kept constant, the mass loss is recorded as a function of the operating time. **Figure 4.2** shows a linear relationship of the mass loss through a 20  $\mu\text{m}$  sized aperture with the running time, which confirms that the measurement is operated at a steady state of the mass change. The experimental data also fit well with the theoretical values estimated from Equation 4.2. The second experiment is carried out by keeping the operation time constant, and recording the mass loss as a function of the aperture size. As shown in **Figure 4.3**, a linear dependence of the water flow rate  $Q$  is obtained with the diameter  $D$  of apertures:  $Q = 6.6 \times 10^{-10} \text{ g}\cdot\text{s}^{-1}\cdot\mu\text{m}^{-1} \times D$ , which achieves a  $\sim 90\%$  fit to the experimental data. The above experiments demonstrate the reliability of the mass loss measurements. In addition, leakage tests are performed with sealed silicon chips when the container is filled with water and organic liquids, respectively. No mass loss ( $<1 \mu\text{g}$ ) is detected within a week for the chips, confirming a fine sealing of the setup.

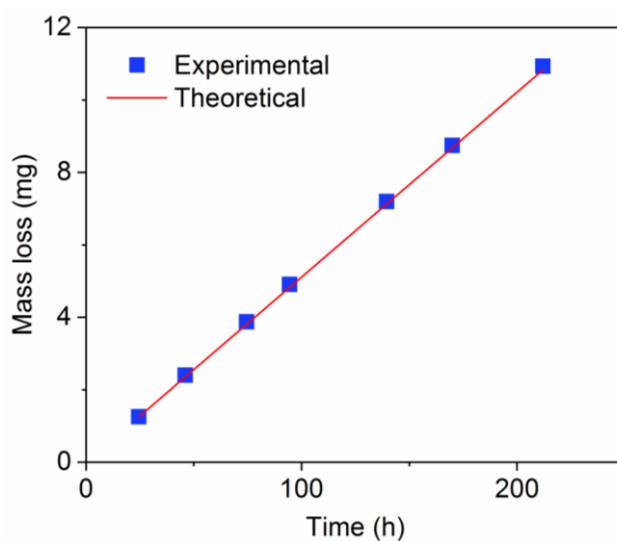


**Figure 4.2.** Mass loss through a 20  $\mu\text{m}$  sized aperture as a function of time. The blue square is the experimental data, and the red curve is plotted with the theoretical values calculated from Equation 4.2.

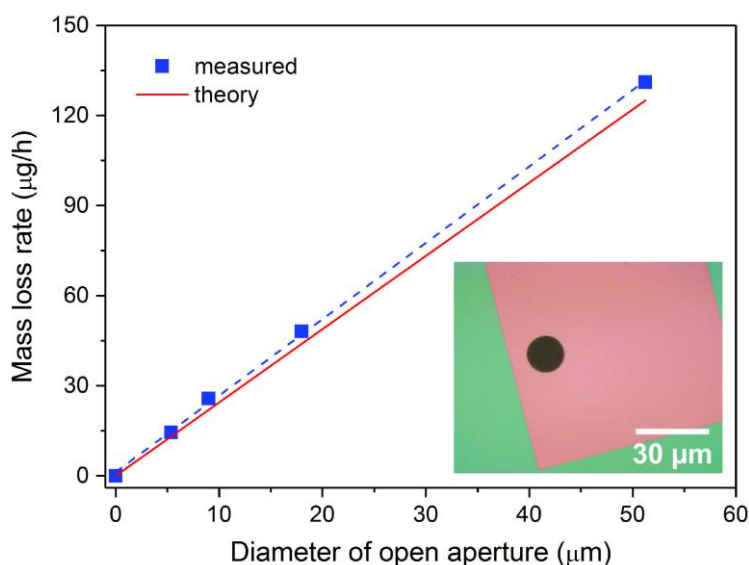


**Figure 4.3.** Dependence of the mass loss rate on the diameter of open apertures. The blue dashed line is a curve derived from a linear fit of the experimental data, and the red line is plotted with the theoretical values predicted from Equation 4.2.

### 4.2.3 Vapor Permeation Through TPT CNMs

Water permeation through TPT CNMs was studied with silicon chips with a 18 μm sized hole. As a reference, we first measured the water flow rate through a same sized aperture without CNMs, observing a mass loss rate of 48.1 μg/h (**Figure 4.4a**). When the aperture is covered with CNMs, the mass loss is only reduced to 6.6 μg/h, corresponding to a water permeance of  $1.1 \times 10^{-4} \text{ mol} \cdot \text{m}^{-2} \cdot \text{s}^{-1} \cdot \text{Pa}^{-1}$ . Compared with other reported literature values measured by the similar method, the water permeance achieved by TPT CNMs seems to be the highest so far. This value is more than 10 times higher than the reported permeances of other nanomembranes (aquaporin biomimetic membranes,<sup>106</sup> graphene based membranes<sup>38,54</sup> and CNT-parylene composite films<sup>34</sup>), and about 2–3 orders of magnitude higher than that of commercial breathable polymer membranes (**Figure 4.5**).<sup>107</sup>

With the same method, other (polar and non-polar) liquids like acetonitrile, n-hexane, ethanol and 2-propanol were also tested. Strikingly, no mass loss was detected, despite that the organic vapors generate a higher vapor pressure difference, i.e., a larger driving force, than water vapor. Considering that kinetic diameters of these liquids are larger

than 0.265 nm of water,<sup>108</sup> this indicates that TPT CNMs act as molecular sieves, which only permit the passing of molecules below a certain size.

Moreover, to understand the fast water permeation through TPT CNMs, we carried out another mass loss experiment with containers upside down, which resulted in the same permeance as with containers in the upright position, which suggests that the observed fast water transport is likely attributed to a liquid water film on the membrane surface (**Figure 4.4b**). As TPT CNM has a hydrophilic surface with contact angle of  $\sim 49.9^\circ$ ,<sup>109</sup> water vapor in the saturation condition can readily adsorb on its surface and form a liquid layer even in the upright cup measurements. The high water permeance of TPT CNMs was also independently confirmed by another gas permeation measurement in vacuum system (see Section 4.3).

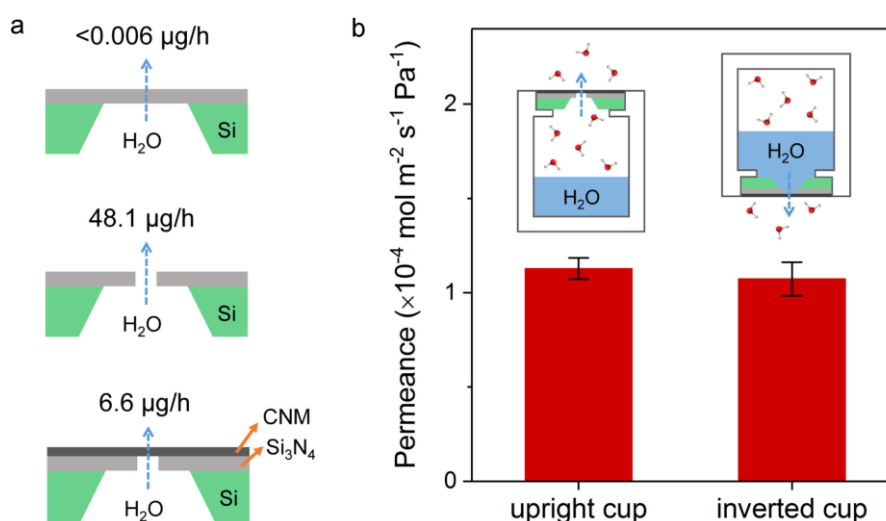


**Figure 4.4.** Mass loss measurements. (a) Mass loss rates measured in upright position for a sealed Si<sub>3</sub>N<sub>4</sub>/Si chip (top), a 18- $\mu\text{m}$ -sized hole without (middle) and covered with CNMs (bottom). (b) Water permeance of TPT CNMs measured by mass loss—upright cup (liquid water not in contact with CNMs) and inverted cup (liquid water in contact with CNMs). The error bars denote standard error of mean within 4–6 samples.

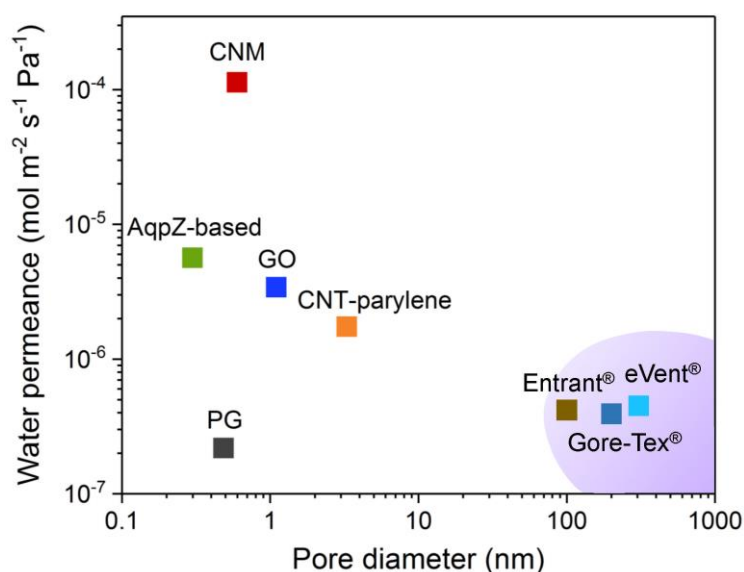


**Figure 4.5.** Water permeances of CNMs and other membranes (commercial breathable polymers,<sup>107</sup> CNT-parylene composite films<sup>34</sup>, aquaporin-based membrane<sup>106</sup>, perforated graphene (PG) with pore diameter of ~0.5 nm and porosity of 0.6%<sup>38</sup> and graphene oxide membrane<sup>54</sup>) as a function of pore diameters. The boundary for breathable polymers was plotted on the basis of the reported values in the literature.<sup>107</sup>

### 4.3 Measurements in Vacuum System

#### 4.3.1 Basics and Setup

In order to characterize gas permeation through freestanding CNMs, we adopted an approach used for ultrathin polymeric membranes.<sup>110</sup> The principle scheme of the experiment is illustrated in **Figure 4.6**. A suspended CNM sample was sealed onto a 2 mm thick copper disk compatible with a CF<sup>®</sup> flange. The assembled sample was further mounted in a homemade permeation cell representing a multiport CF<sup>®</sup> vessel. The cell was designed to have two ports for membranes and reference samples providing identical pathways for incoming molecules. The permeation cell was connected to a high vacuum chamber equipped with a quadrupole mass-spectrometer (Hal-1001 Hiden Analytical) and with a base pressure of  $\sim 2 \times 10^{-9}$  mbar. The upstream side of the sample was exposed to variable amounts of anhydrous gases or water vapors as controlled by a capacitance manometer (MKS Baratron<sup>®</sup> Type 626).

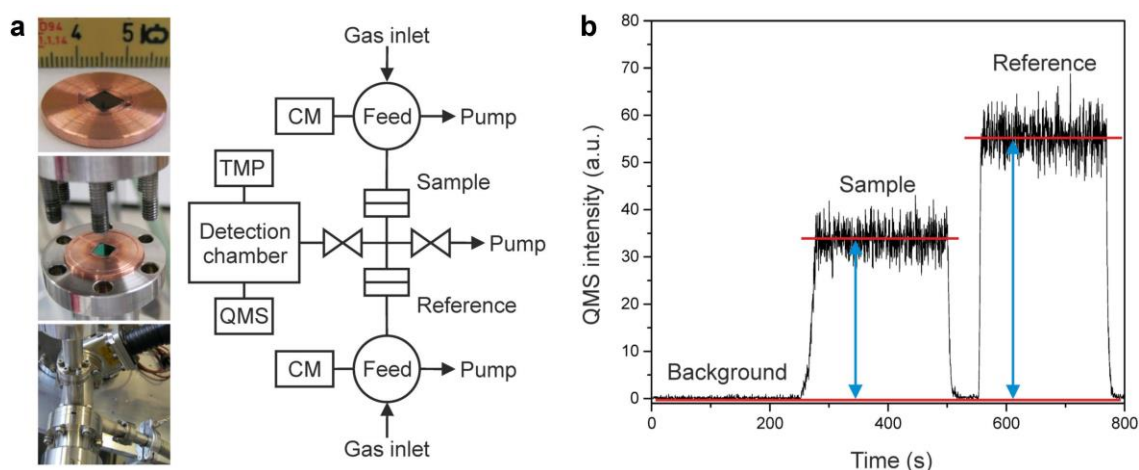


**Figure 4.6.** (a) Schematic and photographs of the gas permeation setup. The permeance was detected by a quadrupole mass-spectrometer (QMS). (b) Exemplary mass-spectrometry analysis: the signal intensity of instrumental background noise, a TPT CNM sample and the reference sample.

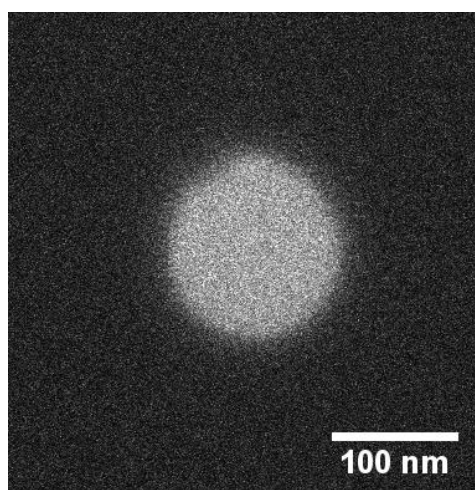


**Figure 4.7.** Scanning transmission HIM image of a reference sample used for mass spectrometer measurements. The reference sample is produced by drilling a  $\sim 140$  nm sized hole in a 100 nm thick  $\text{Si}_3\text{N}_4$  membrane by using a focused helium ion beam.

The membrane permeance was quantified by the mass-spectrometer with a help of the reference sample which can be separately fed by a gas of interest. As a reference, we employed a nanoaperture produced in a 100 nm thick  $\text{Si}_3\text{N}_4$  membrane by a focused helium ion beam (**Figure 4.7**). A linear response of the spectrometer to the amount of

gas in the permeation cell is observed over the range of interest. To ensure that the mass spectrometer was not overwhelmed by large quantities of water vapor, Si<sub>3</sub>N<sub>4</sub>/Si chips with 5 μm sized holes were employed for preparing freestanding CNMs measured in the vacuum system.

To start a gas permeation measurement, we first record the mass-spectrometer background signal corresponding to residual concentration of the species of interest in the detection chamber, then we feed the CNM sample with the gas of interest and measure the signal of the permeating molecules. When the chamber is evacuated and the background signal is recovered, we supply the gas of interest to a reference sample and detect the respective signal. The experimental data were evaluated as following:

$$P = \frac{P_{ref} \cdot I_{sample} \cdot A_{ref}}{P_{sample} \cdot I_{ref} \cdot A_{sample}} \cdot \frac{1}{\sqrt{2\pi mkT} \cdot N_A} \quad (\text{Equation 4.3})$$

where  $p_{sample}$ ,  $p_{ref}$  are feed pressures applied to the membrane and reference samples respectively (Pa),  $I_{sample}$  and  $I_{ref}$  are mass spectrometer signals corresponding to the membrane and reference samples,  $A_{ref}$  is area of the reference aperture (m<sup>2</sup>),  $A_{sample}$  is membrane area (m<sup>2</sup>),  $m$  is molecular mass of the gas of interest (kg),  $k$  is the Boltzmann constant (m<sup>2</sup>·kg·s<sup>-2</sup>·K<sup>-1</sup>),  $T$  is temperature (K), and  $N_A$  is the Avogadro constant (mol<sup>-1</sup>). The experiments were performed at room temperature.

### 4.3.2 Gas Permeation Through TPT CNMs

With the vacuum system, water permeation through TPT CNMs was first investigated. One side of the CNM was exposed to water vapor under the relative humidity (RH) which is controlled by the amount of water vapor supplied in the feed chamber and quantified by the partial pressure. The flow of permeating molecules was detected by the mass spectrometer placed behind the CNMs in the detection chamber. The measured water permeance as a function of the RH is plotted in **Figure 4.8**. Within the experimental accuracy, the water permeance at saturation conditions (100% RH) agrees well with the gravimetric results, confirming an extremely high water permeance of TPT CNMs. At lower humidity, the permeance dropped. That is likely because that at high humidity, more water molecules adsorbed on solid surfaces,<sup>111</sup> facilitating the movement of water across the membranes. Unlike GO membranes that water permeation stopped at low humidity,<sup>54</sup> the permeance of TPT CNMs did not vanish with



decreasing humidity but remained at  $\sim 2.0 \times 10^{-5} \text{ mol}\cdot\text{m}^{-2}\cdot\text{s}^{-1}\cdot\text{Pa}^{-1}$  at RH below 20%. This seems related to a transition between different transport mechanisms.

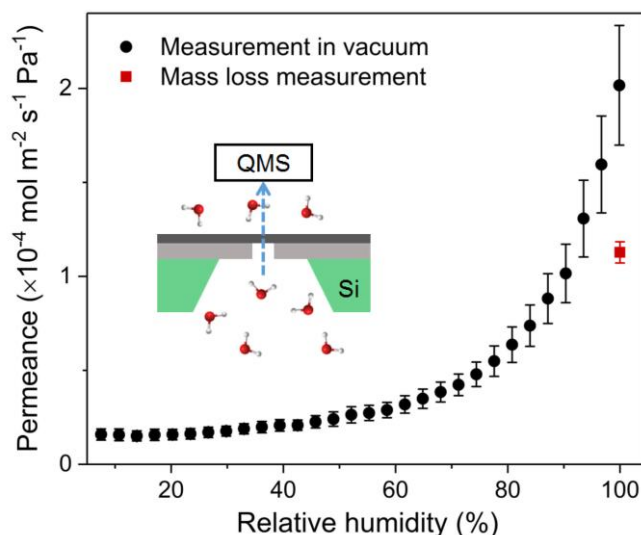


**Figure 4.8.** Water permeance of TPT CNMs as a function of the RH in the feed chamber measured in the vacuum apparatus. The red square is the value measured by the mass loss methods (upright cup). The error bars denote standard error of mean within 4–6 samples.

With the same methods, we also tested the transport of other gases, including He, Ne, CO<sub>2</sub>, Ar, O<sub>2</sub>, N<sub>2</sub>. Only permeation of helium through TPT CNMs was detected. Interestingly, the permeance of helium ( $\sim 4.5 \times 10^{-8} \text{ mol}\cdot\text{m}^{-2}\cdot\text{s}^{-1}\cdot\text{Pa}^{-1}$ ) is 2,500 times lower than that of water although they have similar kinetic diameters<sup>112</sup> (0.265 nm for water and 0.26 nm for helium). No noticeable permeation was detected for other gas molecules with kinetic diameters larger than 0.275 nm. This is consistent with the mass loss measurements that the CNM is a “sieve” that only allows the passing of small molecules and atoms (**Figure 4.9**).

After the permeation experiments, CNMs are examined by HIM to ascertain that they were not damaged during the permeation measurements. An example of the samples is shown in **Figure 4.10**. The membrane remains intact after measurements. The contamination on the surface likely results from the transmitting process from the vacuum system to the atmospheric condition.

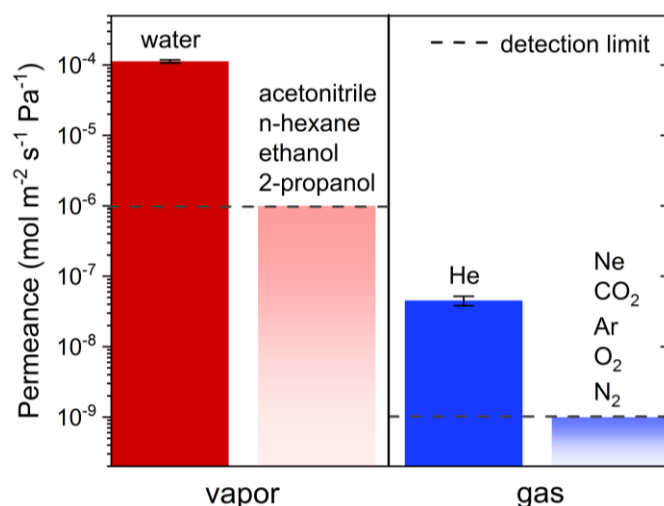


**Figure 4.9.** Permeances of vapors and gases of TPT CNMs measured by two different experiments. The dashed lines indicate the respective detection limits of our measurements. The detection limit of vapor permeation measurements is related to the sensitivity of the balance and the duration of the experiment. The detection limit of gas permeation measurements depends on the instrumental background noise (a signal produced with a blank test) of the mass spectrometer. The error bars denote standard error of mean within 4–6 samples.

**Table 4.1.** Kinetic diameters of gases and liquids.<sup>108,112</sup> The values are taken from refs. 108 and 112.

|                 | Kinetic diameter (Å) |
|-----------------|----------------------|
| water           | 2.65                 |
| acetonitrile    | 3.4                  |
| n-hexane        | 4.3                  |
| ethanol         | 4.3                  |
| 2-propanol      | 4.7                  |
| He              | 2.6                  |
| Ne              | 2.75                 |
| CO <sub>2</sub> | 3.3                  |
| Ar              | 3.4                  |
| O <sub>2</sub>  | 3.46                 |
| N <sub>2</sub>  | 3.64                 |

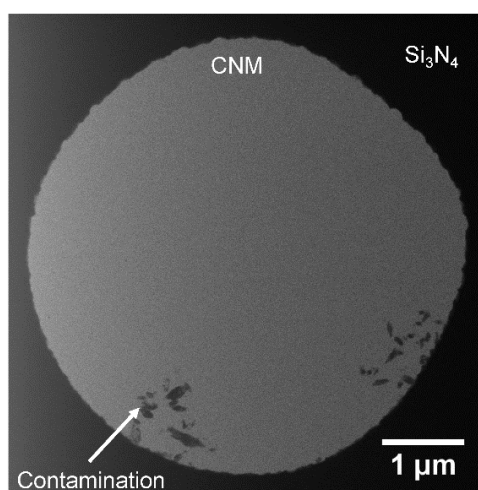


**Figure 4.10.** Scanning transmission HIM image. A TPT CNM covering a 5  $\mu\text{m}$  hole in a  $\text{Si}_3\text{N}_4/\text{Si}$  chip is still intact after permeation experiments.

## 4.4 Understanding the Permeation Behavior

### 4.4.1 Structure of TPT SAMs and CNMs

To understand the observed permeation behaviors, the structure of TPT CNMs was reinvestigated using high-resolution STM and AFM in ultra-high vacuum system. Conversion of TPT SAMs to CNMs is schematically illustrated in **Figure 4.11a**. The topography image of a TPT SAM acquired by STM shows that TPT molecules adsorb in different but highly oriented and densely packed monolayer domains on Au(111) surface, as shown in **Figure 4.11b** and **Figure 4.12a**.<sup>113-115</sup> A boundary between two domains is marked by a yellow line in **Figure 4.11b**. The topography of TPT SAM investigated by AFM (**Figure 4.12b**) is similar to the one shown by the STM image. The molecular corrugations of  $0.58 \pm 0.01$  nm and  $1.03 \pm 0.02$  nm extracted from line profiles of the microscope imaging are in accordance with other reported values.<sup>114-115</sup> XPS measurements in Section 3.1.2 revealed that the TPT molecules were arranged in a densely packed monolayer of  $\sim 1.2$  nm thickness, as determined from the attenuation of the Au4f7/2 photoelectrons.<sup>78-79</sup> After electron irradiation, this monolayer structure is completely reorganized. Tapping mode AFM images show that the resulting CNM contains a dense network of sub-nanometer (sub-nm) channels (**Figure 4.11c**).

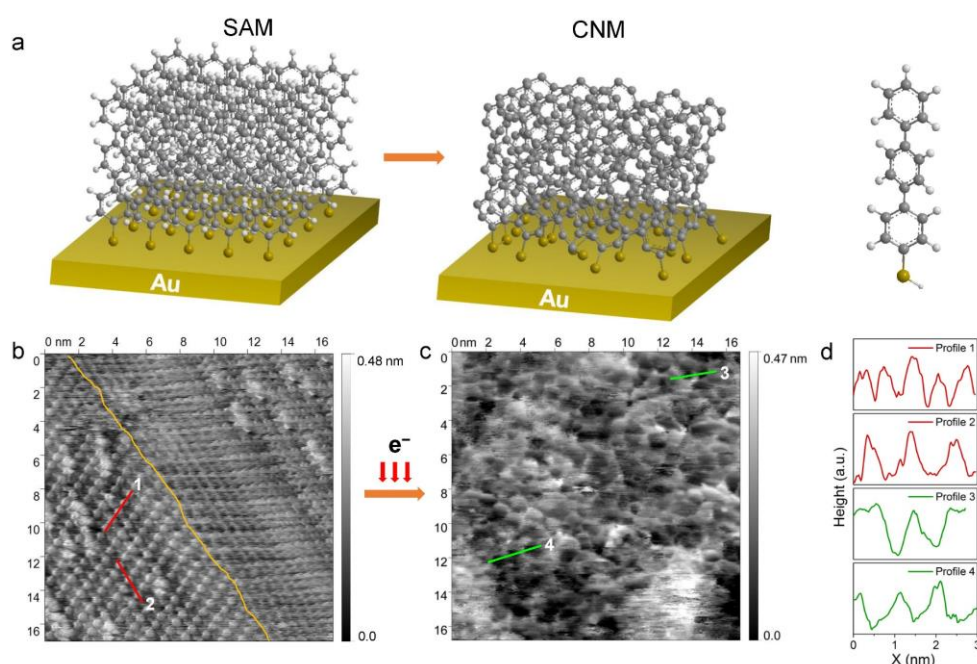


**Figure 4.11.** (a) Schematic illustration of transforming TPT SAMs to CNMs. (b) STM image of TPT SAM measured at room temperature in ultra-high vacuum (UHV) ( $U_{Bias} = 790$  mV,  $I_T = 40$  pA). (c) AFM image of TPT CNM measured at 93 K in UHV via AFM tapping mode of operation (amplitude set point  $A = 8.9$  nm, center frequency  $f_0 = 274.9$  kHz). (d) Extracted line profiles in (b) (marked with red lines) and (c) (marked with green lines). All the STM and AFM images shown were drift corrected.

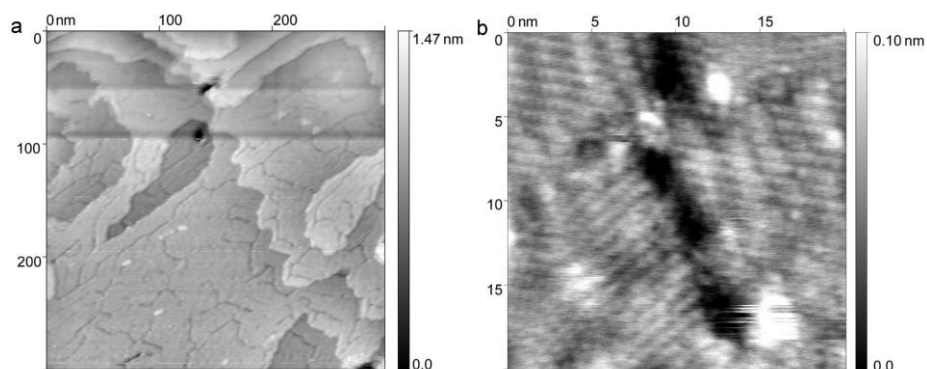


**Figure 4.12.** Morphology of TPT SAM measured by STM and AFM in UHV. (a) STM image of TPT SAM measured at room temperature on a  $300$  nm  $\times$   $300$  nm scale ( $U_{Bias} = 330$  mV,  $I_T = 75$  pA). (b) AFM image of TPT SAM measured at 93 K via non-contact mode of operation (amplitude set point  $A = 14.8$  nm, center frequency  $f_0 = -21.4$  Hz,  $U_{Bias} = 400$  mV).

The pore diameters  $d_{\text{pore}}$  of CNMs is estimated manually by measuring the area of the pores ( $A_{\text{pore}}$ ) shown in AFM images using a mask drawing tool in Gwyddion program (see **Figure 4.13** for example pores). The pore diameter is calculated by assuming that all pores are circular.

$$d_{\text{pore}} = \sqrt{\frac{4A_{\text{pore}}}{\pi}} \quad (\text{Equation 4.4})$$

In addition, by counting the number of pores  $N$  in a selected area  $A$ , the areal pore density  $\sigma$  can be estimated as follows (**Figure 4.14**).

$$\sigma = \frac{N}{A} \quad (\text{Equation 4.5})$$

Based on these analyses, we obtain an average pore diameter of  $0.7 \pm 0.1$  nm and an areal density of  $\sim 10^{18}$  channels  $\text{m}^{-2}$  for TPT CNMs.

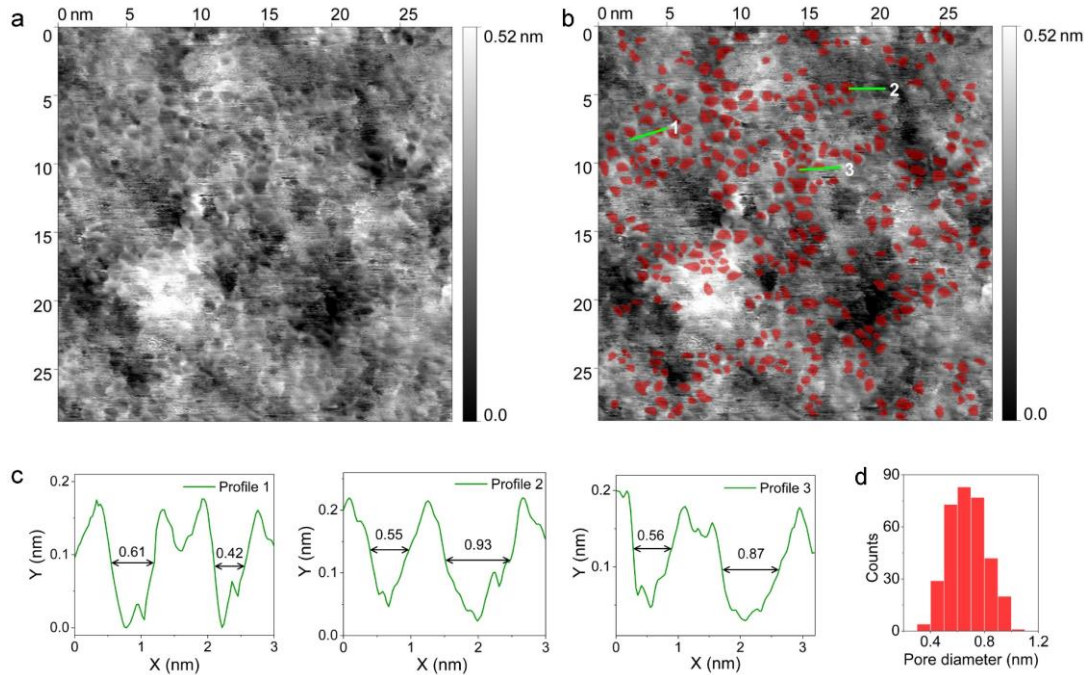


**Figure 4.13.** UHV-AFM image of TPT-CNMs measured at 93 K by AFM tapping mode of operation. (a) Pristine AFM image (amplitude set point  $A = 10.2$  nm, center frequency  $f_0 = 274.9$  kHz). (b) The AFM image with exemplified pores marked by the mask drawing tool of Gwyddion. (c) Extracted Line profiles marked with green lines in (b). (d) Estimated pore diameter distribution of (a).

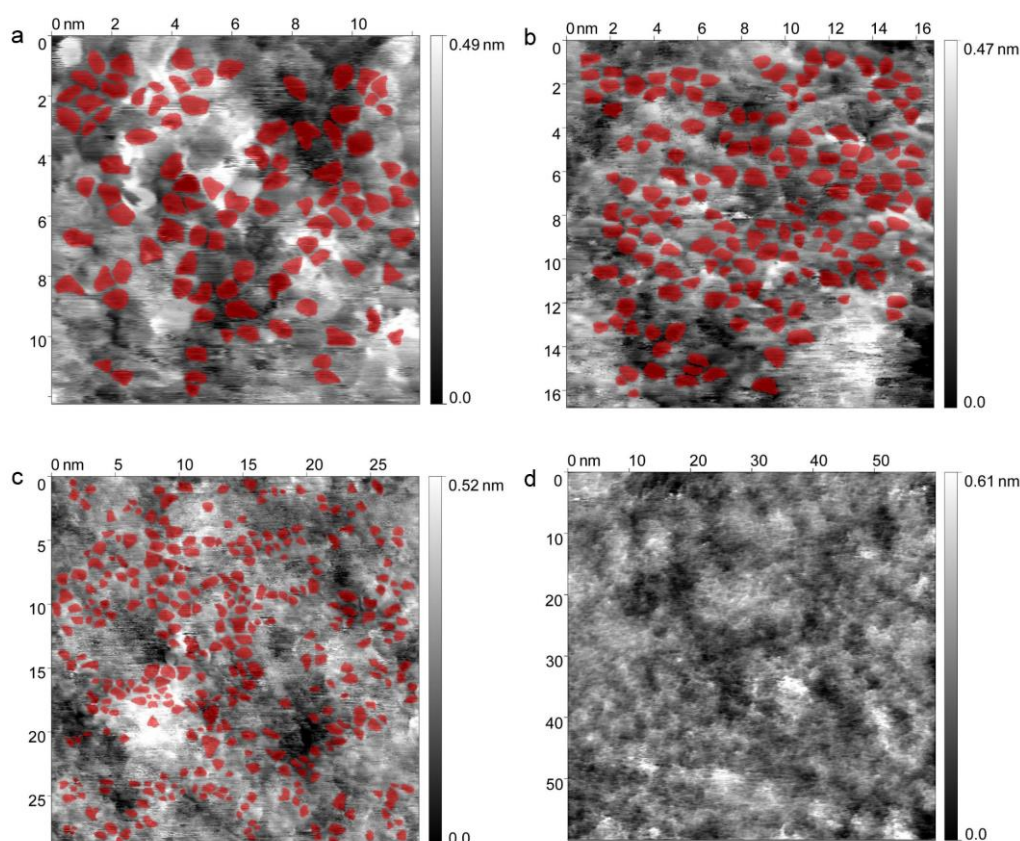


**Figure 4.14.** Estimation of areal pore density from the UHV-AFM images of TPT CNMs. (a) 95 pores are marked and the areal pore density is  $\sim 0.7 \times 10^{18} \text{ m}^{-2}$ . (b) 155 pores are marked and the areal pore density is  $\sim 0.6 \times 10^{18} \text{ m}^{-2}$ . (c) 330 pores are marked and the areal pore density is  $\sim 0.5 \times 10^{18} \text{ m}^{-2}$ . (d) A large-scale AFM image which clearly shows that the TPT CNMs consist of a high density of sub-nm pores.

Earlier spectroscopic and quantum chemical studies<sup>57,78</sup> provided evidence of C–H bond cleavage during electron irradiation of aromatic SAMs, leading to a lateral cross-linking via the formation of C–C linked phenyl rings. A recent study with electron energy loss spectroscopy confirmed that the irradiation of TPT SAMs by 50 eV electrons mainly results in the loss of hydrogen content.<sup>116</sup> In contrast, the content of carbon was conserved, either in aromatic carbon or aliphatic C=C as a result of ring opening,<sup>116</sup> which agrees with our XPS observation in **Figure 3.7** that only a 2% reduction of carbon is detected after electron irradiation. The sulfur spectrum also suggests a transformation from chemisorbed thiolates (R–S–Au) in TPT SAMs to organosulfides (R–S–S–R or R–S–R) in TPT CNMs. The above analyses imply that the formation of sub-nm conduits within the CNMs develop in the occurrence of these cross-linking reactions.

The shape of the sub-nm channels within CNMs can be clearly observed from a high magnification view by AFM (**Figure 4.15**). To understand the pore forming process, we made a drawing of a triangle shaped channel by laterally crosslinking seven TPT molecules using Chemdraw program (PerkinElmer Informatics). The created channel has a similar shape to the one observed by AFM imaging.

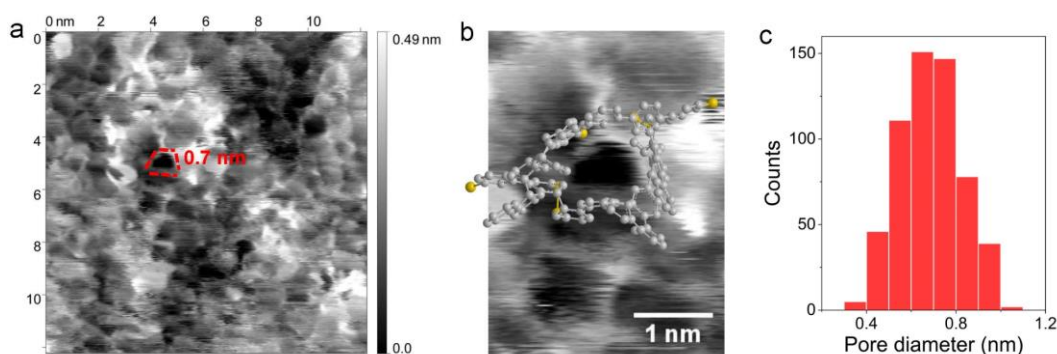


**Figure 4.15.** (a) AFM image of TPT CNM measured at 93 K in UHV via AFM tapping mode of operation (amplitude set point  $A = 7.6$  nm, center frequency  $f_0 = 274.8$  kHz). (b) A drawing of the marked pore in (a) by Chemdraw program (PerkinElmer Informatics). (c) The estimated pore diameter distributions ( $0.7 \pm 0.1$  nm, the error bar denotes standard deviation) extracted from the acquired AFM images.

However, if looking at the kinetic diameters of the non-permeating molecules (**Table 4.1**), the AFM based estimation of  $\sim 0.7$  nm for the average channel diameter appears to be too large. This is possibly because that the AFM images were obtained from tapping mode operation which are governed by short-range repulsive interaction forces,<sup>117</sup> whereas the permeation through  $\sim 1.2$  nm long channels in TPT CNMs may also be affected by (attractive) long-range forces. In addition, the channels may possess inner structures inaccessible by AFM imaging. Assuming that the channels are narrower in the middle and wider at their ends, similar like the channels in aquaporin proteins, this would reduce the active pore diameter in permeation. This view is further supported by an estimation of pore sizes from the classical models. Sampson's formula is a typical model that can be used for evaluating a viscous flow through an orifice of zero thickness.<sup>118</sup> Using this model, Celebi *et al.* well predicted the gas flow through perforated graphene.<sup>37</sup> However, considering that TPT CNMs are not infinitely thin and

their thickness is still larger than the average pore diameter, another modified model for assessing the viscous flow through a finitely-thin orifice is employed here:<sup>119</sup>

$$r = \left[ \frac{Q \cdot \mu}{\Delta p} \cdot \left( \frac{8L}{\pi \cdot R} + 3 \right) \right]^{1/3} \quad (\text{Equation 4.6})$$

where  $r$  is the pore radius (m),  $Q$  is the volumetric flow rate ( $\text{m}^3 \cdot \text{s}^{-1}$ ),  $\mu$  is the dynamic viscosity ( $\text{Pa} \cdot \text{s}$ ),  $\Delta p$  is the pressure drop across the pore (Pa),  $L$  is the pore length (m),  $R$  is the gas constant ( $\text{J} \cdot \text{K}^{-1} \cdot \text{mol}^{-1}$ ).

As TPT CNMs only permit the passage of helium and water, the effective pore diameter is supposed to be around 0.3 nm. For a given pore density and water permeance, the pore diameter estimated from Equation 4.6 is 0.56 nm, which is within the reasonable range of the expectation, yet slightly smaller than the one detected by AFM. Note that this model is ideally suited for viscous flow, whereas the assumed pore size of CNMs is too narrow to fit, thus a deviation may still exist between the actual pore size and the estimated value from the formula. Overall, the ~0.7 nm diameter determined from AFM images must be considered as an upper limit for the active pore diameters.

#### 4.4.2 Molecular Transport Mechanism Through TPT CNMs

To further understand the distinct differences between water and helium, the molecular transport through TPT CNMs with sub-nm channels is hereby discussed. The permeation process basically involves three steps: (i) molecules adsorb on the membrane surface and diffuses to the channel; (ii) move across the channel; and (iii) dissociates from the channel and desorbs from the surface.

For the first step, we compare water and helium by calculating their molar densities on the surface.<sup>120</sup> As indicated in the mass-loss measurements, at saturation conditions, water readily forms a liquid film on the membrane surface. Thus, the density of liquid water can be considered as the molar density on the surface, which is  $5.6 \times 10^4 \text{ mol} \cdot \text{m}^{-3}$ . In comparison, the density of helium is only  $5.3 \text{ mol} \cdot \text{m}^{-3}$  at the applied pressure of 130 mbar in the permeation experiments. Therefore, the probability that a water molecule in a water film reaches the channel is much higher than that of a helium atom in the gas phase.



Assuming that all sub-nm channels in CNMs are active in mass transport, a single-channel permeation coefficient  $\Pi$  can be calculated as follows:

$$\Pi = P \cdot N_A / \sigma \quad (\text{Equation 4.7})$$

where  $P$  is the permeance ( $\text{mol} \cdot \text{m}^{-2} \cdot \text{s}^{-1} \cdot \text{Pa}^{-1}$ ),  $N_A$  is the Avogadro number ( $\text{mol}^{-1}$ ), and  $\sigma$  is the areal pore density ( $\text{m}^{-2}$ ).

The permeation coefficient is calculated to be  $\sim 66$  water molecules  $\cdot \text{s}^{-1} \cdot \text{Pa}^{-1}$  per channel for TPT CNMs. To understand this value, we looked into other extensively studied nanochannel systems, like CNTs and aquaporin proteins. Researches on flow through CNTs have demonstrated both experimentally and theoretically that there exists a transition from continuum to subcontinuum transport for liquid flow in nanoscale systems.<sup>121-123</sup> As predicted from the continuum Poiseuille flow (see Equation 1.13), the flow velocity would decrease monotonically with decreasing pore diameter. However, according to molecular dynamic simulations, when pore diameter is smaller than 1.25 nm, an increase in water flow velocity is observed when the CNT diameter decrease from 1.10 nm to 0.83 nm (**Figure 4.16**).<sup>122</sup>

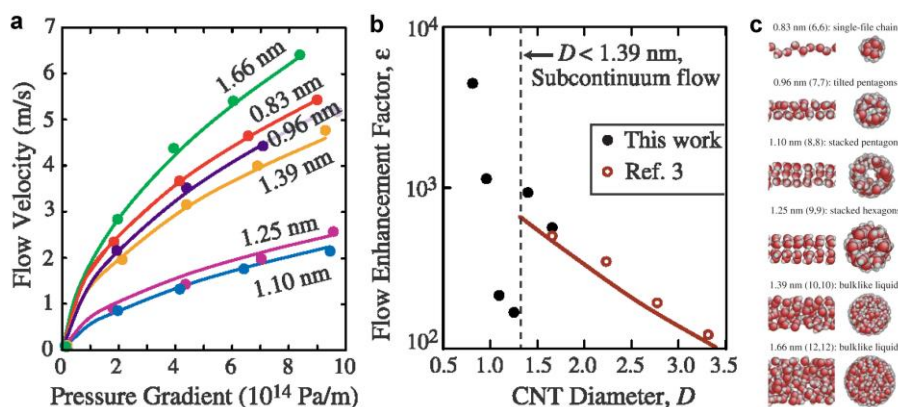


**Figure 4.16.** Molecular dynamic simulations on water flow in CNTs.<sup>122</sup> (a) Relationship between average flow velocity and applied pressure gradient for the 75 nm long CNTs. (b) Flow enhancement factor as a function of the CNT diameter. The enhancement factor is defined as the ratio of observed flow rate to the estimations from the Poiseuille law. Ref. 3 in the graph refers to ref. 123 in this thesis. (c) Molecular dynamics simulation snapshots of water structures inside the 0.83–1.66 nm diameter CNTs. Adapted with permission from ref. 122, American Physical Society.

For 0.81 nm wide CNTs, over 3 orders of magnitude enhancement over the estimations from the Poiseuille law has been observed, which is attributed to a single-file coordinated water transport. An abrupt change in enhancement between 1.39 and 1.25 nm suggests a transition to subcontinuum transport, which likely results from the structural variation of hydrogen bonding network of water.<sup>121-122</sup> Although the mass transport mechanisms are not yet clear, it has been suggested that water molecules become less interacted with the CNT surface in sub-nm sized channels, which may reduce the flow friction and increase the velocity.<sup>122-123</sup>

We found that the obtained value of  $\sim 66$  water molecules $\cdot$ s $^{-1}\cdot$ Pa $^{-1}$  per CNM channel compares well with the values obtained for CNTs with diameters of 0.66 nm ((5,5)CNT) and 0.81 nm ((6,6)CNT), and aquaporin proteins with diameter of  $\sim 0.3$  nm (**Figure 4.17**).<sup>45,124-125</sup> It implies that water molecules confined in these sub-nm channels form water chains attributed to the strong and short time hydrogen-bonding character between neighboring molecules,<sup>126</sup> which allows water to rapidly rush through as a single file. The cooperative effect in TPT CNMs is also well supported by the permeation data shown in **Figure 4.4**. In comparison, helium exhibits no directed and comparatively strong interactions at room temperature, thus lacking a concerted and cooperative transport. Hence, water passes through the channel apparently faster than helium in the second step (see also **Figure 4.18**).

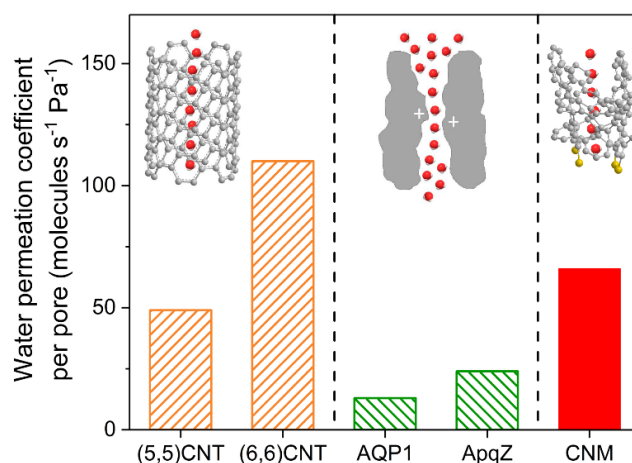


**Figure 4.17.** A comparison of single-channel water permeation coefficients between different membranes. Molecular dynamics simulation was used to study the permeation coefficients of CNTs ((5,5)CNT,<sup>45</sup> (6,6)CNT<sup>45</sup>), and a stopped-flow apparatus was employed to characterize aquaporins (AQP1,<sup>124</sup> AqpZ<sup>125</sup>).

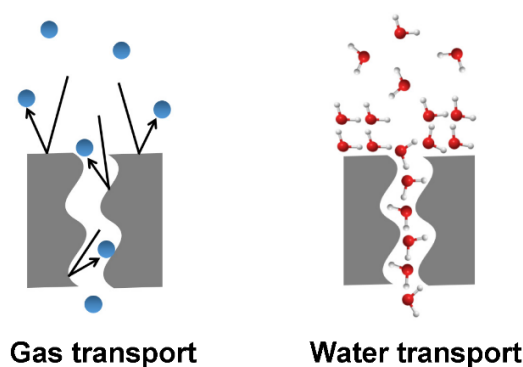


**Figure 4.18.** Schematic of gas and water transport path through the nanochannels in CNMs. Water molecules permeate cooperatively through the channel as a single file. In comparison, helium exhibits no strong interactions at room temperature. Besides, the steric hindrance could also impede the helium permeation, but has no effect on water permeation.

#### 4.5 Summary

In summary, we found that TPT CNMs are perforated by a high density of sub-nm channels that filter water with very high permeance and high molecular selectivity. The water permeance determined from the mass-loss method is in good agreement with the permeance detected by mass spectrometry. The rapid water permeation through CNMs is ascribed to a high areal density of sub-nm channels of  $10^{18}$  channels per  $\text{m}^2$  within the membrane, and a cooperative water transport across these channels, similar to the mechanisms responsible for the rapid water flow through aquaporin and carbon nanotubes. Unlike other carbon materials, CNMs are built in a versatile and scalable fabrication process, allowing membranes to be customized with nanometer thickness and chemistry.<sup>57,63</sup> Especially the possibility to modify CNMs by different functional groups<sup>57</sup> at the surface will allow further pathways to tailor and optimize the selectivity of the translocation process in future applications. These advantages make CNMs a highly promising material for efficient separations, such as dehydration of organics, dehumidification of gases, and purification of water.



# Chapter 5

## Ion Exclusion by TPT CNMs

### 5.1 Introduction

Chapter 4 presented molecular transport through TPT CNMs and demonstrated that the membrane is impermeable to most of gases and liquids, but permits the rapid passage of water. With this finding, a question arises that whether the membrane can still act as a molecular sieve in a liquid mixture composed of water and other substances. To give the answer, this chapter will study the motion of ionic species by employing ion conductance measurements. These experiments can test the sieving properties of TPT CNMs in a real mixture system.

### 5.2 Basics and Setup

The principle and setup of ion conductance measurements is schematically shown in **Figure 5.1**. The homemade permeation cell consists of two identical compartments made by polycarbonate. On each part two channels are created, in order to build a connection to the membrane and fix the distance between electrodes as well. CNM covered Si chips are assembled between the two compartments and sealed with two 600  $\mu\text{m}$  thick PDMS sheets. A 3 mm sized hole is punched in the middle of the PDMS sheet. To avoid the occurrence of air bubbles in the liquid filling process, the cell is first wetted with isopropanol, and then rinsed with sufficient amount of degassed salt solutions for exchanging the isopropanol.

The ion conductance measurements are performed using both DC and AC methods. To investigate the ion transport properties, the conductance is measured in five types of 1 M of chloride solutions, including HCl, LiCl, KCl, NaCl and MgCl<sub>2</sub>. Before real experiment, we firstly performed a control measurement to test the reliability of the whole system. For this purpose, 20 mM of KCl solution are employed as the electrolyte because most theories only applies to dilute solutions when describing the ion activities;

when the concentration increases, the ionic interactions start to be involved, which is not accounted for in the theory.<sup>127</sup>

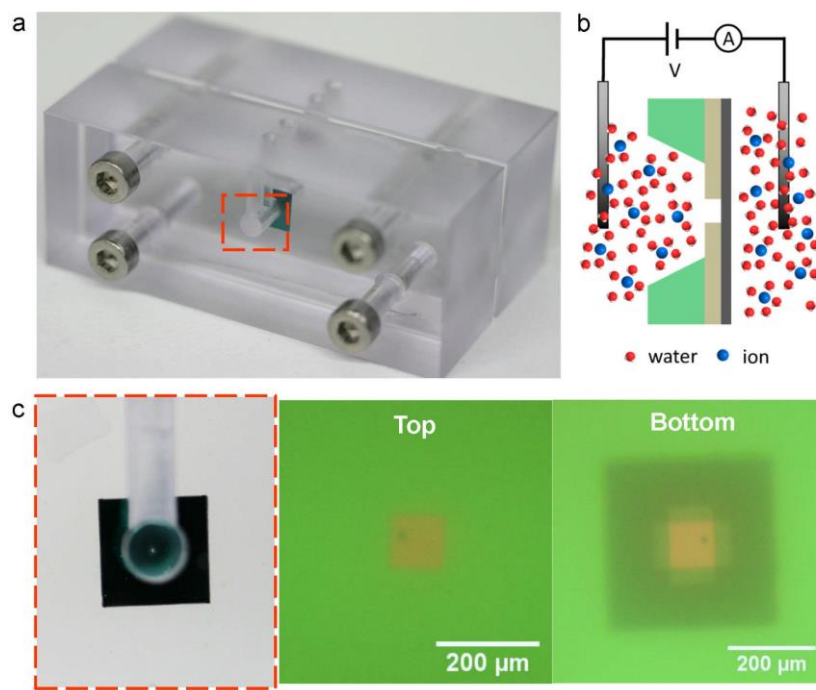


**Figure 5.1.** Ionic conductance measurements. (a) Photograph of the permeation cell. (b) Schematic of the experimental principle. (c) Exclusion of large air bubbles in the permeation cell after mounting the samples: photograph view through the window of the permeation cell (left), and optical microscope image of Si chips from the top view (middle) and bottom view (right).

In the experiments using DC method, the conductance is acquired by collecting I-V characteristics using a pair of Ag/AgCl electrodes. The electrodes are re-chlorided and calibrated regularly to ensure the stability and repeatability of the measurements. The current is recorded by using an Axopatch 200B amplifier (Axon Instruments) with a low-pass Bessel filter. The data is collected in 50 mV increments between  $-300$  mV and  $300$  mV. To facilitate the data processing and analysis, the collected current is further compressed by averaging the current values so as to reduce the number of data points. An analysis of the raw data and filtered data is plotted in **Figure 5.2** and **Table 5.1**. The average current obtained from the filtered data are in accordance with that extracted from the raw data.

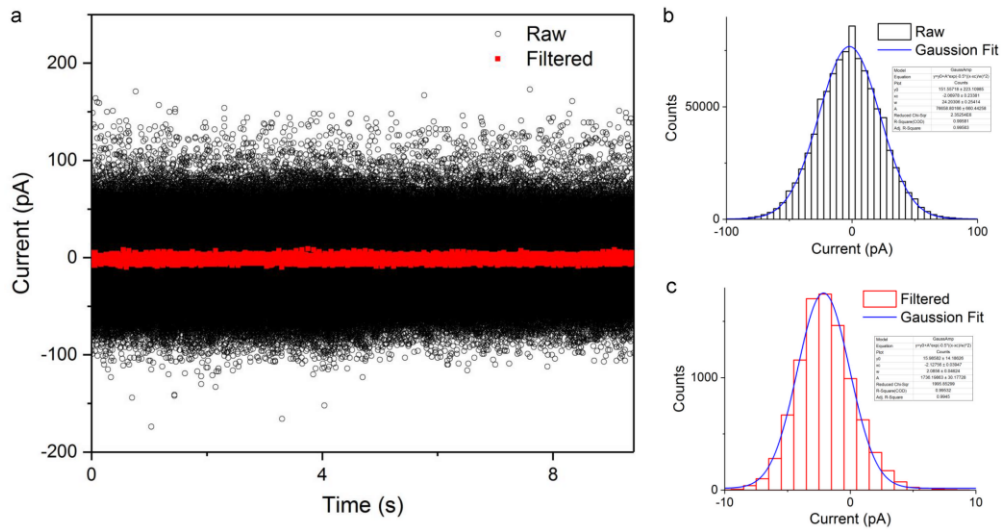


**Figure 5.2.** Data acquisition and analysis using DC method. (a) The raw data collected from the Electrical Patch device and the filtered data used for analyzing. Histogram of current distribution of (b) raw data and (c) filtered data. The bin size is taken as 1.

**Table 5.1.** Analysis of data extracted from the Gaussian fit in Figure 5.2.

|                             | Raw     | Filtered |
|-----------------------------|---------|----------|
| Number of data points       | 941,213 | 9,412    |
| Average current (pA)        | -2.070  | -2.128   |
| Standard error of mean (pA) | 0.025   | 0.022    |

Measurements of ion transport with AC method is performed by using electrochemical impedance spectroscopy (EIS). The experiments are carried out with the same permeation cell as employed in the DC method, but with a four-electrode system to reduce the undesired artifacts arising in the two-electrode systems. The data are recorded in potentiostatic mode by Reference 600 Potentiostat/Galvanostat (Gamry Instruments, Inc.). The AC amplitude was set at 1 mV. The EIS data are fitted to equivalent circuits by Echem Analyst program.

Ion conductance through a neutral pore can be estimated as follows:<sup>5,128</sup>

$$G = \sigma \left( \frac{L}{\pi R^2} + \frac{1}{2R} \right)^{-1} \quad (\text{Equation 5.1})$$

where  $\sigma$  is the bulk ionic conductivity ( $\text{S}\cdot\text{m}^{-1}$ ),  $L$  is the pore length (m),  $R$  is the pore radius (m). The first part of the equation is associated with the process of ion moving through a pore, and the second part is related to the occurrence of ion entering and leaving a pore.

### 5.3 Ion Conductance Measurements

#### 5.3.1 Measurements Using DC Method

As a control measurement, the ionic conductance through a  $15\ \mu\text{m}$  sized aperture in  $\text{Si}_3\text{N}_4/\text{Si}$  chip was first quantified by using  $20\ \text{mM}$  KCl solution (**Figure 5.3**). The current flow is found to be linearly proportional to the applied voltage across the open hole. The experimentally determined conductance of  $\sim 3\ \mu\text{S}$  fits well with the theoretical predictions from Equation 5.1. In contrast, when the aperture is covered with TPT CNMs, the current flow is nearly undetectable, sharing a similar tendency with a sealed silicon chip.

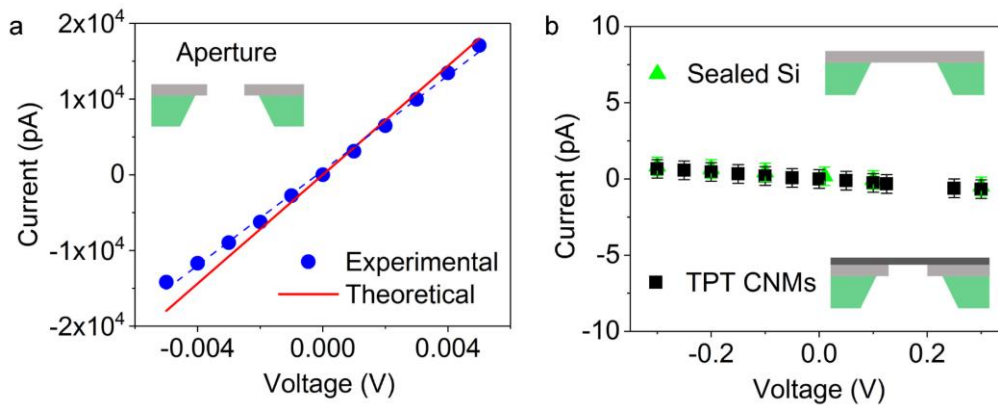


**Figure 5.3.** Ion conductance measurements with  $20\ \text{mM}$  KCl solution. (a)  $I$ - $V$  curves of a  $15\ \mu\text{m}$  aperture without TPT CNMs covered. The dashed line is a linear fit of the experimental data. The red curve is a plot of theoretical values obtained from Equation 5.1. (b)  $I$ - $V$  curves of a sealed Si chip and a  $15\ \mu\text{m}$  aperture with TPT CNMs covered. The error bar denotes the accuracy of determining current by the measurement.



The subsequent measurements in a variety of 1 M chloride solutions show that the current flow through CNMs only fluctuates in a range of  $-5$  pA to  $5$  pA at applied voltages between  $-0.3$  V to  $0.3$  V. Some I–V curves show a negative slope, which is most likely due to a slight drift of the baseline current during the measurements.<sup>129</sup> For the sealed silicon chip, a pA level current is also detected, which can be attributed to a tiny leakage. Accordingly, the small fluctuation observed for TPT CNMs is considered to be a perturbation combining the drift effects and leakage currents, which however is negligible compared to the  $\mu$ A level current detected for the same sized aperture without membrane covered (**Figure 5.4**). If taking the fluctuating range as detection limits of the measurement, a rough estimation could be made that ions cross over TPT CNMs with at least  $10^6$  times lower flux than through the aperture. The G $\Omega$  level transmembrane resistance detected for CNMs, is also found to be comparable to the values measured for planar lipid bilayers which is known to have a typical high resistance. This suggests that TPT CNMs can repel the penetration of ionic species as the lipid does. The reproducibility of the experiments is examined with up to five membrane samples, which all exhibit an ion exclusion behavior (**Figure 5.5**). This finding is also supported by the measurement of a defective membrane. When a few nanometer sized defects are present on a CNM, the resistance instantly drops to  $10$  M $\Omega$  (**Figure 5.6**).

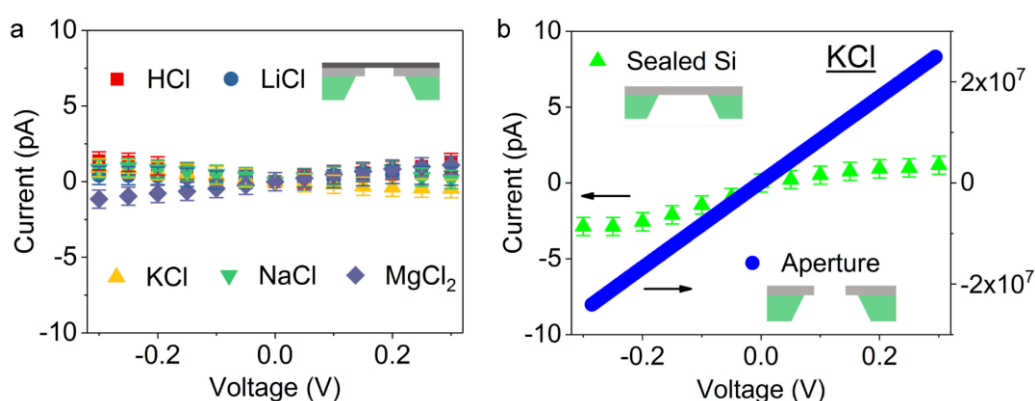


**Figure 5.4.** Ionic conductance measurements. (a) I–V curves of TPT CNMs suspending over a  $15 \mu\text{m}$  circular aperture in a  $\text{Si}_3\text{N}_4/\text{Si}$  chip in 1 M solutions of HCl, LiCl, KCl, NaCl and  $\text{MgCl}_2$ . (b) I–V curves of a  $15 \mu\text{m}$  circular aperture and a sealed  $\text{Si}_3\text{N}_4/\text{Si}$  chip in 1 M KCl solution. The error bar denotes the accuracy of determining current by the measurement.

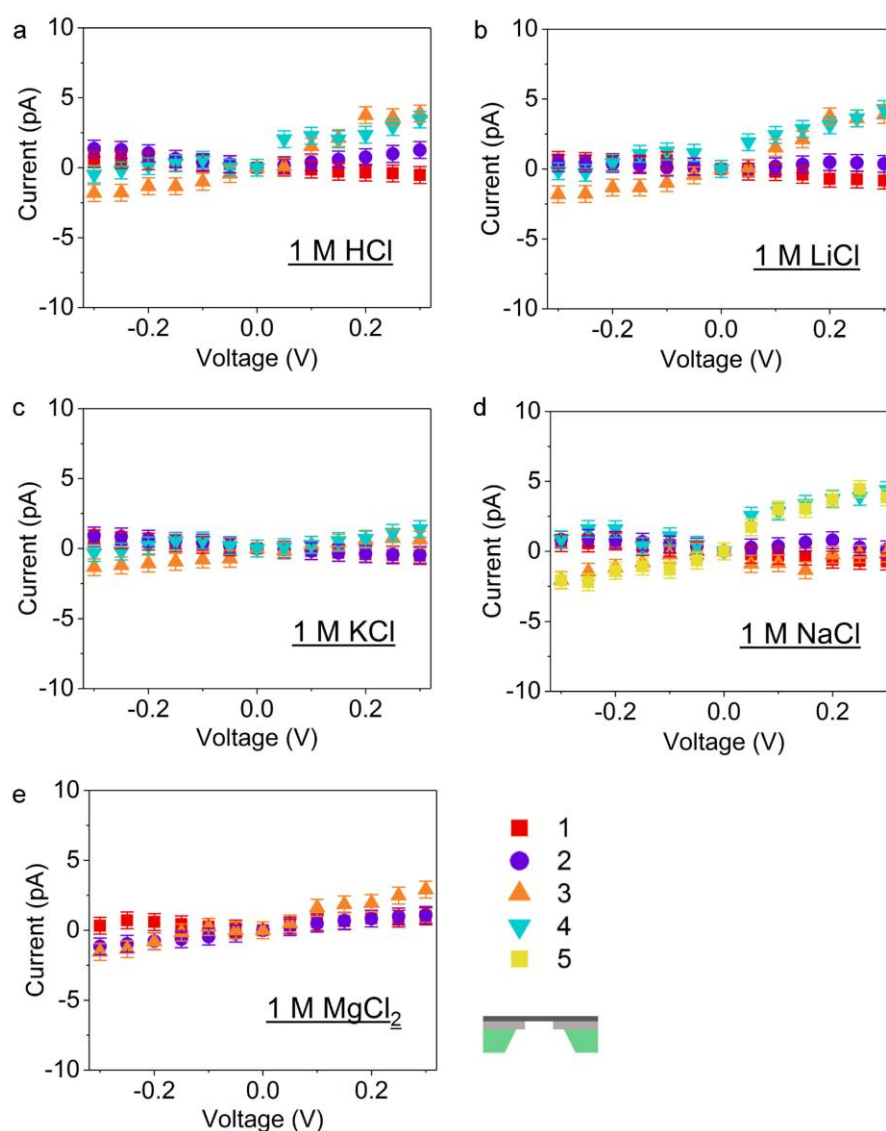


**Figure 5.5.** Ionic conductance measurements:  $I$ - $V$  curves of TPT CNMs measured in 1M solutions of HCl (a), LiCl (b), KCl (c), NaCl (d), and  $MgCl_2$  (e). 1-5 corresponds to 5 TPT CNM samples. The error bar denotes the accuracy of determining the current by the measurement.

To assure that the measured high resistance is indeed the CNM properties and are not caused by an inappropriate mounting of the samples, we subsequently carry out a dielectric breakdown experiment as follows. A high electric field is applied across the insulated CNMs, which is supposed to induce an accumulation of charge traps in the bulk film, leading to a mechanical rupture on the membrane and creating leakage currents.<sup>130</sup> In this way, the existence of the membrane in the system could be proved.

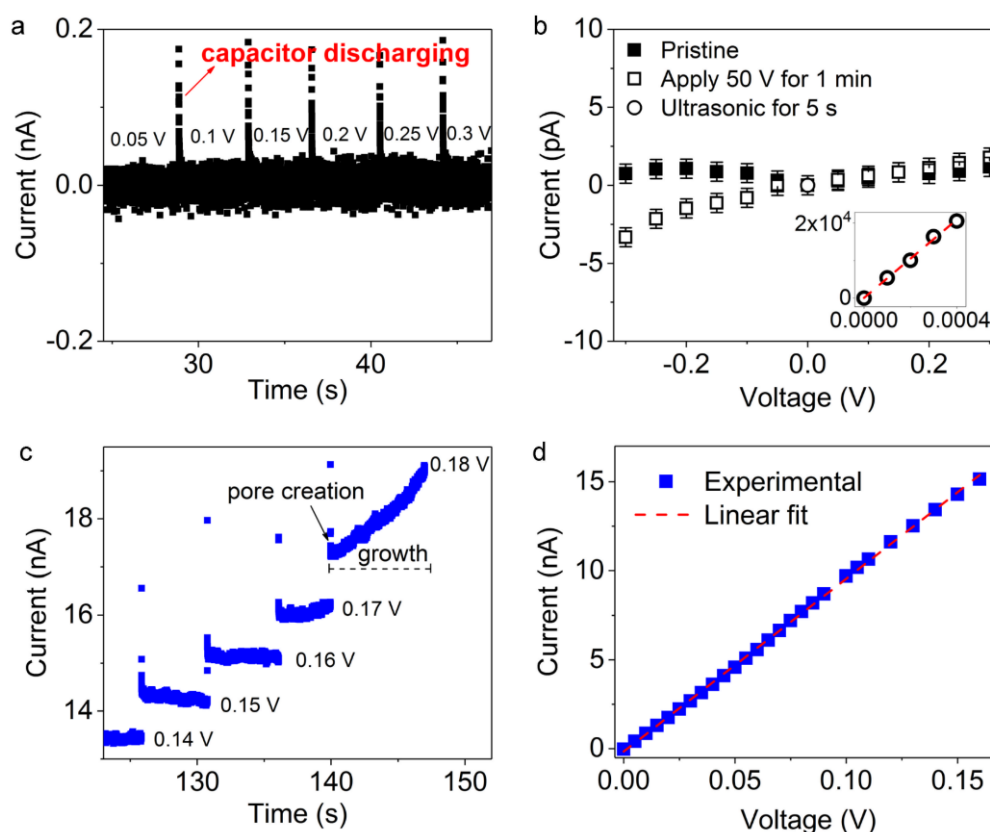


**Figure 5.6.** Ionic conductance and dielectric breakdown characterization in 1 M KCl. (a) Current probed at varied voltages as a function of time for TPT CNMs. (b) I–V curves for pristine TPT CNMs, measurements after applying 50 V across the membrane for 1 min, and after placing the permeation cell into an ultrasonic bath for 5 s. (c) Current as a function of time for a TPT CNM with  $\sim 0.6 \mu\text{m}^2$  defects. (d) I–V curves for the defective TPT CNMs. The current values shown in b and d is average values of the signal detected in a and c. The red dashed line is a linear fit of the experimental data. The error bar denotes the accuracy of determining current by the measurement.

Unexpectedly, for an intact CNM that impedes a current flow, even applying a voltage of up to 50 V for one minute, the current follow is still not notable in 1 M KCl, that is, the membrane remains free of fractures (**Figure 5.6a–b**). Instead, the membrane is eventually damaged by assistance with ultrasonic waves and as a consequence, an ionic conductance of  $\sim 50 \mu\text{S}$  was detected. These results reveal that the intact CNM can withstand high electric potentials. The phenomena was further evidenced by a following experiment shown in **Figure 5.6c–d**. In the case of a defective CNM, a constant ionic conductance of  $\sim 100 \text{ nS}$  was detected when the applied voltages is below 0.17 V.

According to Equation 5.1, the defects area is calculated to be  $\sim 0.6 \mu\text{m}^2$ . When the voltage increases and reaches up to 0.18 V, the current flow is no longer constant at a constant voltage but starts to increase linearly over time, indicating that the defects are continuously growing. This is likely because that the defects on CNMs experience an increased electric field strength, which locally initiates the defect growth. Although the process through which the material is removed from the defective CNM remains unclear, the analysis implies that the intact CNMs comprise a dense crosslinked network and seem improbable to be easily destroyed by the electrical potentials.

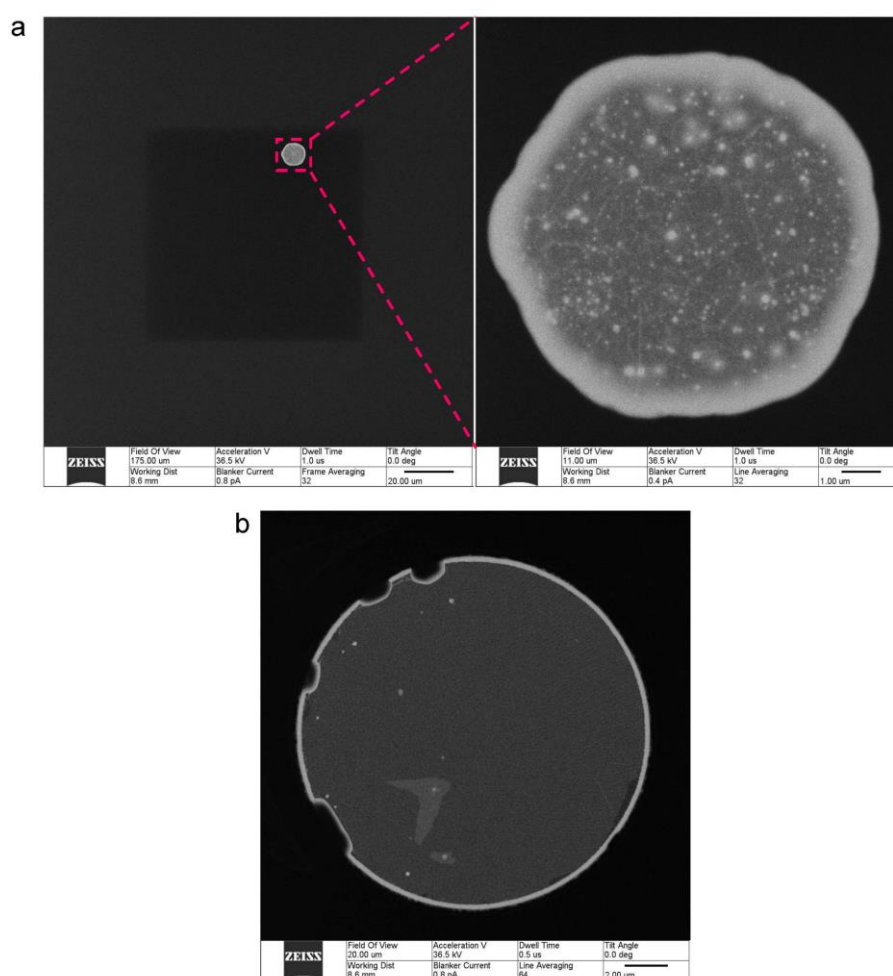


**Figure 5.7.** Helium ion micrograph of two TPT CNM samples after ion conductance measurements. (a) a pristine sample. (b) a sample rinsed with water after measurements.

After conductance measurements, the intactness of CNMs was also examined by helium ion microscopy. As examples, two samples are shown in **Figure 5.7**, a pristine sample and another rinsed with water after the measurements. The pristine sample is fully covered with particles, most likely salt residues, as the measurements were performed in highly concentrated salt solutions. In contrast, another sample is relatively much cleaner, which suggests that these residues can be removed by rinsing with water.

### 5.3.2 Measurements Using AC Method

To probe more characteristics of ionic diffusion across TPT CNMs, an EIS measurement using DC method is employed in a frequency range of  $10^{-2}$ – $10^6$  Hz. The impedance spectrum confirms that ions flow through CNMs with an exceedingly high resistance. Depressed semicircles in Nyquist Plots are fitted to an equivalent electrical circuit model (**Figure 5.8**), which consists of three components: (i)  $R_1$ —a total ohmic resistance of the system, including electrodes, solutions and electrical contacts, associated with the intercept at the  $Z_{\text{real}}$  axis at high frequency, only several  $\Omega$ ; (ii)  $R_2$ —ion diffusion resistance through CNMs, linked to the diameter of the semicircle, in a  $G\Omega$  level; and (iii)  $C_1$ , a constant phase element (CPE) representing a response of membrane capacitance related to the non-porous region of CNMs.

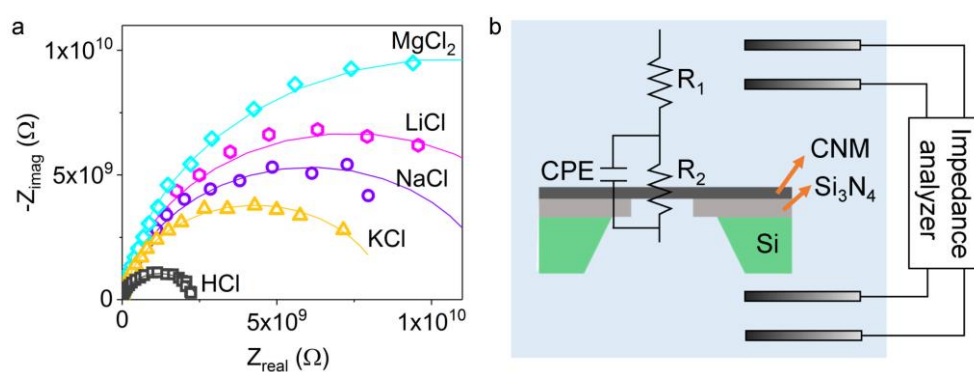


**Figure 5.8.** Electrochemical impedance spectra characterization. (a) Nyquist plots of impedance spectra for TPT CNMs measured in 1 M solutions of HCl, LiCl, KCl, NaCl and  $\text{MgCl}_2$ . (b) Equivalent circuit model for impedance spectra in a.

In comparison, salts pass through the same sized aperture without membrane covered with a  $\sim 10^6$  lower resistance than through TPT CNMs (**Figure 5.9**). It seems that ions moving through CNMs obeys a mechanism that is different with that of the aperture. Especially, the diffusion resistance through TPT CNMs is found to be highly related to the hydration radius of cations in the chloride salts:  $H^+ < K^+ < Na^+ < Li^+ < Mg^{2+}$ . The measurements in  $MgCl_2$  solution yields the highest resistance for TPT CNMs despite it contributing more ions than other solutions in same concentration.

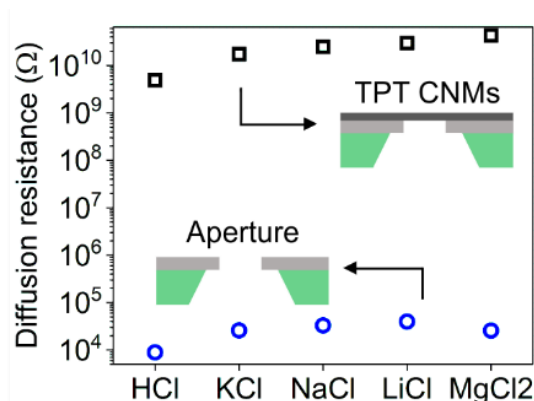


**Figure 5.9.** Comparison of ionic diffusion resistance through the aperture and TPT CNMs in a variety of 1 M chloride solutions.

These phenomena reveal two interesting structural properties of TPT CNMs. Firstly, the limited passage of cations is mainly dominated by a size exclusion mechanism. This again confirms the existence of sub-nm channels within TPT CNMs. Secondly, the membrane can strongly impede the penetration of  $Cl^-$  ions. This can be assigned to the presence of negatively charged groups on membrane surface, determined from a zeta potential measurement shown in **Figure 5.10**. TPT CNMs on two different substrates both show a negative surface charge property in the pH range of 3–9. The negatively charged properties of CNMs on gold is possibly caused by a small amount of carboxyl groups generated from the oxidation of carbon radical residues when CNMs are exposed to air after the crosslinking step. After being transferred onto PAN supports, TPT CNMs become more negatively charged, which may result from the occurrence of oxidized sulfur species produced in the membrane transfer process.

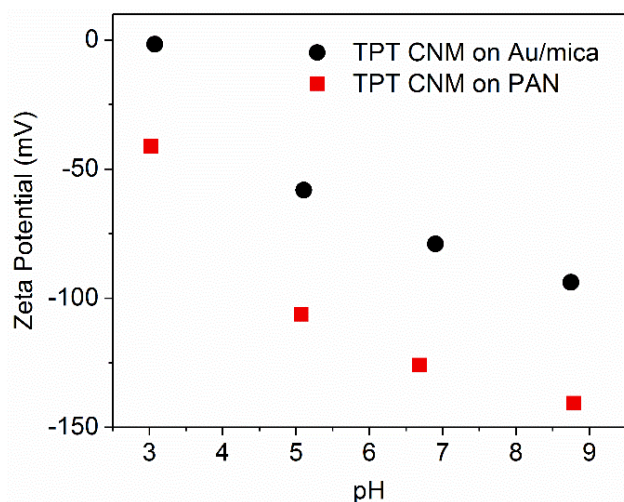


**Figure 5.10.** Zeta potential measurements of TPT CNMs on an Au/mica substrate (before transfer) and on a PAN support (after transfer).

**Table 5.2.** Hydration radius of ionic species.<sup>131</sup> Data is taken from ref. 131.

| Ionic species    | Hydration radius (Å) |
|------------------|----------------------|
| H <sup>+</sup>   | 2.82                 |
| K <sup>+</sup>   | 3.31                 |
| Na <sup>+</sup>  | 3.58                 |
| Li <sup>+</sup>  | 3.82                 |
| Mg <sup>2+</sup> | 4.28                 |
| Cl <sup>-</sup>  | 3.32                 |

Compared with biological systems, the specific resistance of  $\sim 10^4 \Omega \cdot \text{cm}^2$  detected for TPT CNMs is in the same level as the typical high resistance of planar lipid bilayers (**Figure 5.11**). According to the areal pore density of  $10^{18} \text{ m}^{-2}$  determined from AFM imaging in Section 4.4.1, a single-channel conductance of  $10^{-6} \text{ pS}$  is obtained for TPT CNMs in 1 M KCl. This value is more than  $\sim 10^7$  times lower than that of a single ion channel in lipid membranes acquired in similar measurement conditions. This implies that TPT CNMs present as a barrier against motion of ions like lipid bilayers.

The above explanation is also well supported by the phase shift of the EIS measurements. The bode plots in **Figure 5.12** reflects that a sealed silicon chip shows a purely capacitive behavior that the impedance decreases as the frequency is raised, with a fairly constant phase angle of  $-90^\circ$ . In contrast, CNMs present a highly resistive diffusion process in frequencies below 0.04 Hz, and a capacitive response in frequencies between 3 and  $10^6$  Hz. The phase angle also shows a gradual shift from  $0^\circ$  to  $-90^\circ$  while moving from low to high frequency. The aperture exhibits a similar impedance pattern as TPT CNMs, but with  $\sim 10^6$  lower diffusion resistance, and the transition from being resistive to capacitive also occurs at a much higher frequency of  $\sim 10^5$  Hz. These results are consistent with the data acquired by DC methods in **Figure 5.4**.

The electrochemical measurements revealed that TPT CNMs are able to impede the passage of ions including protons, which seems valid as the hydration diameter of ions exceeds the effective membrane channel size of  $\sim 3$  Å.<sup>100</sup> The limited passage of ions detected by EIS could be ascribed to a leakage current or interpreted by a transport in activated regime<sup>5</sup> where the diffusion relies on bond stretching or flexing. However, we note that the transport of protons in water follows a Grotthuss mechanism, that is, protons can move along the channel by hopping from one water molecule to another. Accordingly, the rapid water permeation through TPT CNMs should also facilitate the proton transport. Therefore, excepting steric hindrance, other energetic barriers should also contribute to the observed ion exclusion. Aquaporin proteins, as biological water channels, can perfectly hinder the transport of protons. Several simulations have provided hints that the water/proton selectivity in aquaporin systems is attributed to an electrostatic barrier, but debates still remain on whether residual charges<sup>132</sup> or low dielectric regions<sup>133</sup> in proteins dominate the electrostatic origin. In addition, simulations in carbon nanotube systems indicate that the mobility of protons is very high in nonpolar 1D water wires but it can be interrupted if orientational defects are present in the hydrogen-bonded water chains<sup>134</sup>. Overall, it seems that proton transport in the sub-nm narrow channels is a complicated process. To fully elucidate the transport behavior, extensive experiments and dynamic simulations are still required.



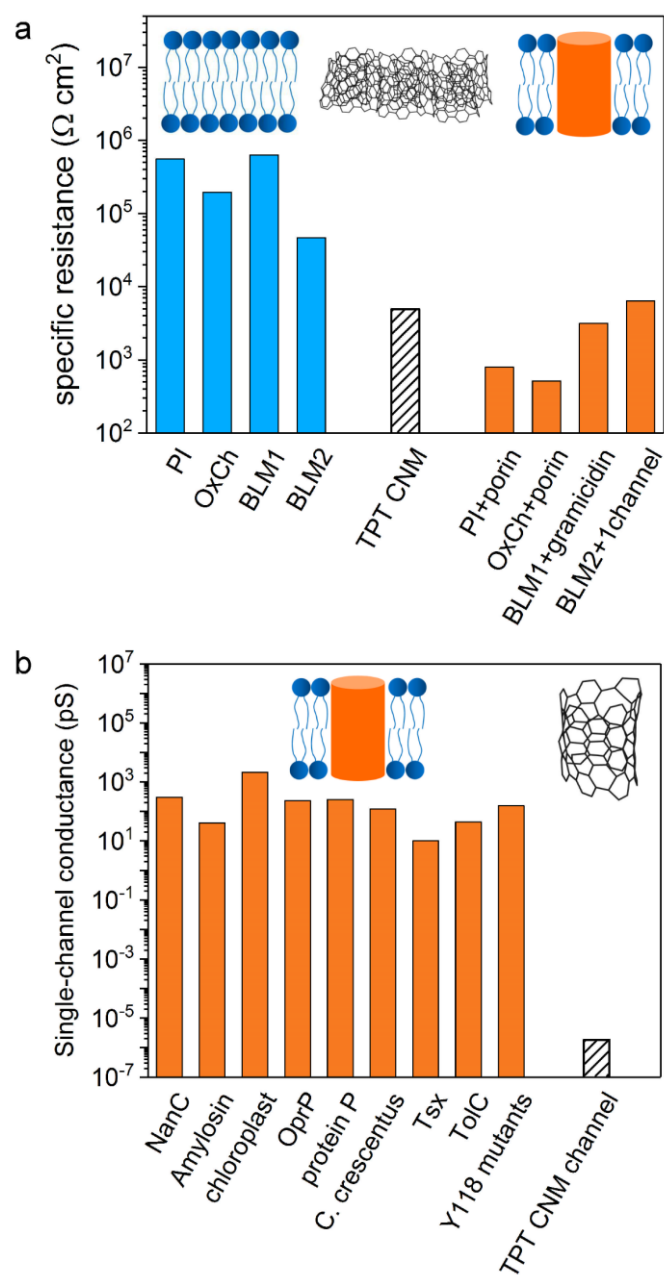


**Figure 5.11.** A comparison of ion transport behaviors between TPT CNMs and biological systems. (a) Specific resistance of TPT CNMs, pure lipid bilayers (PI,<sup>135</sup> OxCh,<sup>135</sup> BLM1<sup>136</sup> and BLM2<sup>137</sup>) and bilayers with a single ion channel (PI+porin,<sup>135</sup> OxCh+porin,<sup>135</sup> BLM1+gramicidin<sup>136</sup> and BLM2+1channel<sup>137</sup>). The resistance of planar lipid bilayers differs in varied salt concentration and types, in a wide range of  $10^4$ – $10^7 \Omega \cdot \text{cm}^2$ , thus the literature values selected for comparison are acquired in 1–2 M KCl solution. (b) Single-channel conductance of TPT CNMs and biological ion channels (NanC,<sup>138</sup> Amylosin,<sup>139</sup> chloroplast,<sup>140</sup> OprP,<sup>141</sup> protein P,<sup>142</sup> C. crescentus,<sup>143</sup> Tsx,<sup>144</sup> TolC,<sup>145</sup> Y118 mutants<sup>146</sup>).

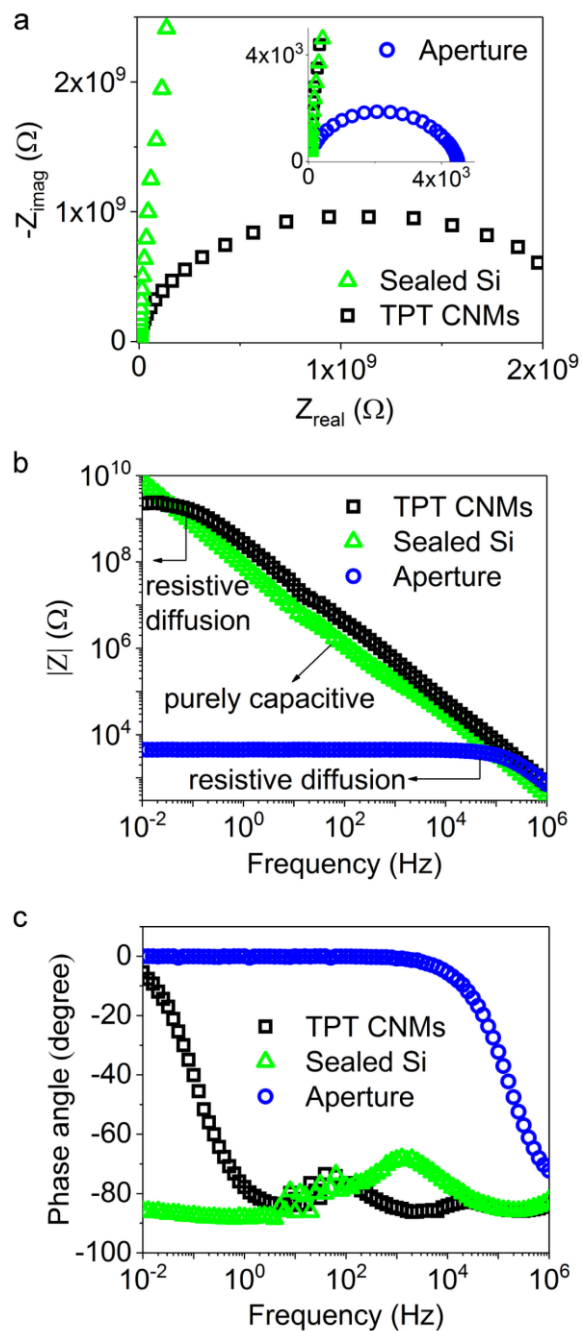


**Figure 5.12.** EIS measurements in 1M HCl solution. Nyquist plots (a), bode plots of impedance magnitude  $|Z|$  (b) and phase shift (c) as a function of frequency for the aperture, TPT CNMs and sealed Si chip.

## 5.4 Summary

Ion transport through TPT CNMs was investigated using both DC and AC electrochemical measurements. The results demonstrate that TPT CNMs can filter out ions including protons. The DC method works well for the micrometer sized aperture as the data has a good signal-to-noise ratio, but it is very sensitive to a baseline drift and a tiny leak when measuring of TPT CNMs due to a very high membrane resistance. With an AC based EIS measurement, the ion diffusion resistance through the membrane could be extracted by fitting the data to equivalent electrical circuits. The obtained transmembrane resistance of  $\sim 10^4 \Omega \cdot \text{cm}^2$  is in the same level as that of the pure planar lipid bilayers. A single channel conductance is calculated to be  $2 \times 10^{-18} \text{ S}$  in 1 M KCl solution,  $>10^7$  times lower than that of a biological porin. This finding reveals a rigid structure of CNMs in liquid systems, and encourages their use as a new membrane platform for studying biological systems, as well as in separation processes like water purification.



## Chapter 6

### Conclusions and Outlook

This work investigated the permeation properties of freestanding TPT CNMs by several permeation experiments including mass loss measurements, gas permeation in vacuum system and ion conductance measurements. The results revealed that TPT CNMs act as molecular sieves, exhibiting high water selectivity and high permeance; they exclude most gases (Ne, CO<sub>2</sub>, Ar, O<sub>2</sub>, N<sub>2</sub>), liquids (acetonitrile, n-hexane, ethanol, 2-propanol), as well as ionic species including protons, but permit the passage of water and helium. Water transits with a remarkably high permeance of  $\sim 1.1 \times 10^{-4} \text{ mol} \cdot \text{m}^{-2} \cdot \text{s}^{-1} \cdot \text{Pa}^{-1}$ ,  $\sim 2,500$  times faster than helium. The water permeance achieved by TPT CNMs is orders of magnitude higher than other existing membranes. The sieving behavior is attributed to a dense network of sub-nm channels within TPT CNMs. The rapid water flow is ascribed to a single-file transport of 66 water molecules  $\text{s}^{-1} \cdot \text{Pa}^{-1}$  per single channel, similar to the phenomenon observed for aquaporin proteins and carbon nanotubes, and a high areal channel density of  $10^{18} \text{ m}^{-2}$  within the membrane.

In liquid solutions, TPT CNMs can also hinder the penetration of ionic species. Ions transmit through the membrane with a specific resistance as high as that of pure lipid bilayers. The obtained single-channel conductance is  $\sim 10^7$  times lower than the value for a biological porin. The sieving properties suggest that TPT CNMs have an identical behavior as the protein channels—aquaporins, which only allow water to pass, but block all ionic species. With advances in nanofabrication, many efforts have been made to mimic these nature structures, but none is really successful. A more recent progress has been achieved by 2D slits made from stacking graphite or hBN crystals with graphene as spacers.<sup>51</sup> These devices can block small ions such as Na<sup>+</sup> and Cl<sup>-</sup>, but proton is still an exception. Although the mechanism of excluding protons by TPT CNMs remains unclear, the membrane can be considered as a potential platform for enriching the understanding of biological processes.

The molecular sieving properties also inspire the use of TPT CNMs for a variety of

separation processes, such as water purification, dehydration of organics, etc. CNMs as 2D filters that combines ease fabrication with tunable fabrication, provide enormous potentials in manipulating membrane architecture with precision in sub-nm dimensions. Careful design of these molecular filters could bring about new opportunities in molecular separation. Thus further work on exploring the tunability of CNMs would promote the developing of this 2D membrane system. In addition, temperature-dependent transport experiments and molecular dynamic simulations might be useful in further understanding the transport mechanisms.

## List of Figures

|  |    |
|--|----|
| <b>Figure 1.1.</b> First demonstration of reverse osmosis membranes. <sup>4</sup> .....  | 11 |
| <b>Figure 1.2.</b> Mechanisms of molecular transport through dense membranes and porous membranes. <sup>2,5</sup> Reprinted with permission from ref. 5, Springer Nature.....  | 12 |
| <b>Figure 1.3.</b> Spherical particle flow in a cylindrical pore. <sup>11</sup> .....  | 14 |
| <b>Figure 1.4.</b> Permeation properties of Knudsen and Poiseuille flow as a function of the pore radius ( $r$ ) divided by the mean pore path ( $\lambda$ ) of the gas. <sup>2,14</sup> .....   | 15 |
| <b>Figure 1.5.</b> Illustration of estimating mean free path from kinetic theory. <sup>15-16</sup> .....   | 16 |
| <b>Figure 1.6.</b> Properties of conventional polymer membranes. (a) Scanning electron microscopy images of porous membranes made by phase inversion: the upper panel is a cross-section of a polysulfone membrane with finger-like macrovoids, <sup>25</sup> and the lower panel is a top view of a commercial polyvinylidene fluoride membrane (EMD Millipore, Billerica, MA, USA). <sup>22</sup> (b–c), Permeance and selectivity trade-off relations in polymer membranes: b, O <sub>2</sub> /N <sub>2</sub> separation; <sup>26</sup> c, Water/salt separation. <sup>27</sup> The upper panel of part a is reprinted with permission from ref. 25, Elsevier, and the lower panel is reprinted with permission from ref. 22, Springer Nature. Part b is adapted with permission from ref. 26, Elsevier. Part c is reprinted with permission from ref. 27, Elsevier. .... | 20 |
| <b>Figure 1.7.</b> Thin-film composite membranes made by interfacial polymerization. (a) Polyamide fabricated in a conventional way. <sup>22</sup> (b) Sub-10-nm thin polyamide fabricated with a sacrificial layer of nanostrands. <sup>29</sup> (c) Polyamide fabricated by electrospinning. <sup>30</sup> Panel a is reprinted with permission from ref. 22, Springer Nature. Panel b is reprinted with permission from ref. 29, The American Association for the Advancement of Science. Panel c is reprinted with permission from ref. 30, The American Association for the Advancement of Science. ....  | 22 |
| <b>Figure 1.8.</b> Bottom-up approach for fabricating molecularly selective membranes. (a) Top, illustration view of water passage through aquaporin; <sup>39</sup> bottom, schematic of aquaporin-based biomimetic membranes. <sup>40</sup> (b) Top, illustration view of CNT structure; bottom, schematic and SEM cross-section view of CNT-embedded membranes. <sup>33</sup> (c) Top, crystal structure of ZIF-90; <sup>41</sup> bottom, SEM cross-section view of mixed-matrix membranes containing ZIF-90 crystals. <sup>42</sup> Part a is reprinted with permission from ref.   |    |

|   |    |
|---|----|
| 40, Elsevier. Part b is adapted with permission from ref. 33, The American Association for the Advancement of Science. Part c is adapted with permission from ref. 41, American Chemical Society, and ref. 42, John Wiley and Sons.....   | 23 |
| <b>Figure 1.9.</b> Top-down approach for fabricating molecularly selective membranes. (a) perforated graphene. <sup>49</sup> (b) graphene oxide membranes. <sup>50</sup> (c) 2D capillary devices made from bulk crystals with graphene as spacers. <sup>51</sup> Part a is reprinted with permission from ref. 49, American Chemical Society. Part b is reprinted with permission from ref. 50, The American Association for the Advancement of Science. Part c is reprinted with permission from ref. 51, The American Association for the Advancement of Science. .... | 24 |
| <b>Figure 1.10.</b> Helium ion micrograph of a 1-nm-thick freestanding CNM suspended over a 400 $\mu\text{m}$ wide hexagonal opening of a copper grid. <sup>57</sup> Reprinted with permission from ref. 57, John Wiley and Sons. ....  | 26 |
| <b>Figure 1.11.</b> Fabrication of CNMs from different precursor molecules. <sup>63</sup> The graph is adapted with permission from ref. 63, American Chemical Society. ....  | 27 |
| <b>Figure 1.12.</b> Transfer CNMs to another substrate. <sup>68</sup> Reprinted with permission from ref. 68, Elsevier.....   | 28 |
| <b>Figure 2.1.</b> Schematic illustration of a self-assembled monolayer (SAM) formed from alkanethiolates on an Au(111) surface. <sup>69</sup> Reprinted with permission from ref. 69, American Chemical Society.....   | 31 |
| <b>Figure 2.2.</b> The secondary electron yield as a function of the primary energy for a hexadecanethiol (HDT) monolayer on a gold substrate. <sup>77</sup> Reprinted with permission from ref. 77, AIP Publishing. ....   | 33 |
| <b>Figure 2.3.</b> Schematic representation of four main steps involved in the cross-linking of biphenylthiol SAMs. <sup>78</sup> Reprinted with permission from ref. 78, American Chemical Society.....  | 34 |
| <b>Figure 2.4.</b> Schematic illustration of X-ray photoemission process. ....  | 35 |
| <b>Figure 2.5.</b> Schematic illustration of scanning a metallofullerene and alkanethiol SAM on Au(111) by STM in a constant-current mode. <sup>80</sup> Reprinted from Ref. 80. ....   | 36 |
| <b>Figure 2.6.</b> Schematic view of the principle of AFM. <sup>84</sup> Reprinted with permission from ref. 84, Springer Nature.....   | 37 |
| <b>Figure 2.7.</b> The tip–sample interaction force as a function of the distance. <sup>86</sup> ....   | 38 |
| <b>Figure 2.8.</b> Schematic representation of HIM. <sup>87</sup> Reprinted with permission from ref. 87, AIP Publishing. ....  | 39 |
| <b>Figure 2.9.</b> Sinusoidal Current Response in a Linear System. ....   | 41 |



- Figure 2.10.** Nyquist plots for (a) a capacitor, (b) a capacitor in series with a resistor, (c) a capacitor in parallel with a resistor, and (d) a resistor in series with a parallel RC-circuit.<sup>90</sup> Reprinted with permission from ref. 90, Royal Society of Chemistry..... 42
- Figure 3.1.** Structure of hexaphenylbenzene (HPB) based derivative **1**: 4,4'-(4,4''-bis(methylthio)-3'',6''-diphenyl-[1,1':4',1'':2'',1''':4''',1''''-quinquephenyl]-4'',5''-diyl)dipyridine..... 45
- Figure 3.2.** Schematic illustration of the SAM preparation from HPB derivative **1**... 46
- Figure 3.3.** X-ray photoelectron spectra of the bulk sample, SAM and crosslinked SAM prepared from HPB derivative **1**. .... 48
- Figure 3.4.** Optical micrograph of CNMs from HPB derivative **1** transferred on SiO<sub>2</sub>/Si. .... 49
- Figure 3.5.** Helium ion micrograph of the CNMs made from HPB derivative **1** and transferred onto (a) Lacey carbon films on Cu grids, (b) Quantifoil TEM grids, and (c) Cu 400 mesh grids..... 50
- Figure 3.6.** Structure of the precursor terphenyl-4-thiol (TPT)..... 51
- Figure 3.7.** X-ray Photoelectron Spectra. (a) TPT SAM on Au(111)/mica. (b) TPT CNM on Au(111)/mica. (c) TPT-CNM transferred onto a new Au(111)/mica substrate. .... 52
- Figure 3.8.** Schematic illustration of transferring the CNM onto a Si<sub>3</sub>N<sub>4</sub>/Si chip device with a single microhole. .... 53
- Figure 3.9.** Optical micrograph of two ruptured CNMs from HPB derivative **1** suspended over a microhole on Si<sub>3</sub>N<sub>4</sub>/Si chip..... 54
- Figure 3.10.** Optical and helium ion micrographs of a freestanding TPT CNM suspended over a microhole on Si<sub>3</sub>N<sub>4</sub>/Si chip. The sample was tilted by ~75° for HIM imaging..... 54
- Figure 4.1.** (a) Schematic view and (b) photograph of the mass loss experiments. .... 58
- Figure 4.2.** Mass loss through a 20 μm sized aperture as a function of time. The blue square is the experimental data, and the red curve is plotted with the theoretical values calculated from Equation 4.2. .... 59
- Figure 4.3.** Dependence of the mass loss rate on the diameter of open apertures. The blue dashed line is a curve derived from a linear fit of the experimental data, and the red line is plotted with the theoretical values predicted from Equation 4.2..... 60
- Figure 4.4.** Mass loss measurements. (a) Mass loss rates measured in upright position for a sealed Si<sub>3</sub>N<sub>4</sub>/Si chip (top), a 18-μm-sized hole without (middle) and covered with CNMs (bottom). (b) Water permeance of TPT CNMs measured by mass loss—upright

|  |    |
|--|----|
| cup (liquid water not in contact with CNMs) and inverted cup (liquid water in contact with CNMs). The error bars denote standard error of mean within 4–6 samples.....   | 61 |
| <b>Figure 4.5.</b> Water permeances of CNMs and other membranes (commercial breathable polymers, <sup>107</sup> CNT-parylene composite films <sup>34</sup> , aquaporin-based membrane <sup>106</sup> , perforated graphene (PG) with pore diameter of ~0.5 nm and porosity of 0.6% <sup>38</sup> and graphene oxide membrane <sup>54</sup> ) as a function of pore diameters. The boundary for breathable polymers was plotted on the basis of the reported values in the literature. <sup>107</sup>   | 62 |
| <b>Figure 4.6.</b> (a) Schematic and photographs of the gas permeation setup. The permeance was detected by a quadrupole mass-spectrometer (QMS). (b) Exemplary mass-spectrometry analysis: the signal intensity of instrumental background noise, a TPT CNM sample and the reference sample. ....   | 63 |
| <b>Figure 4.7.</b> Scanning transmission HIM image of a reference sample used for mass spectrometer measurements. The reference sample is produced by drilling a ~140 nm sized hole in a 100 nm thick Si <sub>3</sub> N <sub>4</sub> membrane by using a focused helium ion beam. .  | 63 |
| <b>Figure 4.8.</b> Water permeance of TPT CNMs as a function of the RH in the feed chamber measured in the vacuum apparatus. The red square is the value measured by the mass loss methods (upright cup). The error bars denote standard error of mean within 4–6 samples.....   | 65 |
| <b>Figure 4.9.</b> Permeances of vapors and gases of TPT CNMs measured by two different experiments. The dashed lines indicate the respective detection limits of our measurements. The detection limit of vapor permeation measurements is related to the sensitivity of the balance and the duration of the experiment. The detection limit of gas permeation measurements depends on the instrumental background noise (a signal produced with a blank test) of the mass spectrometer. The error bars denote standard error of mean within 4–6 samples..... | 66 |
| <b>Figure 4.10.</b> Scanning transmission HIM image. A TPT CNM covering a 5 μm hole in a Si <sub>3</sub> N <sub>4</sub> /Si chip is still intact after permeation experiments. ....  | 67 |
| <b>Figure 4.11.</b> (a) Schematic illustration of transforming TPT SAMs to CNMs. (b) STM image of TPT SAM measured at room temperature in ultra-high vacuum (UHV) ( $U_{\text{Bias}} = 790$ mV, $I_{\text{T}} = 40$ pA). (c) AFM image of TPT CNM measured at 93 K in UHV via AFM tapping mode of operation (amplitude set point $A = 8.9$ nm, center frequency $f_0 = 274.9$ kHz). (d) Extracted line profiles in (b) (marked with red lines) and (c) (marked with green lines). All the STM and AFM images shown were drift corrected.....                   | 68 |
| <b>Figure 4.12.</b> Morphology of TPT SAM measured by STM and AFM in UHV. (a) STM  |    |

|  |    |
|--|----|
| image of TPT SAM measured at room temperature on a 300 nm × 300 nm scale ( $U_{\text{Bias}} = 330$ mV, $I_{\text{T}} = 75$ pA). (b) AFM image of TPT SAM measured at 93 K via non-contact mode of operation (amplitude set point $A = 14.8$ nm, center frequency $f_0 = -21.4$ Hz, $U_{\text{Bias}} = 400$ mV).....  | 68 |
| <b>Figure 4.13.</b> UHV-AFM image of TPT-CNMs measured at 93 K by AFM tapping mode of operation. (a) Pristine AFM image (amplitude set point $A = 10.2$ nm, center frequency $f_0 = 274.9$ kHz). (b) The AFM image with exemplified pores marked by the mask drawing tool of Gwyddion. (c) Extracted Line profiles marked with green lines in (b). (d) Estimated pore diameter distribution of (a). .....  | 69 |
| <b>Figure 4.14.</b> Estimation of areal pore density from the UHV-AFM images of TPT CNMs. (a) 95 pores are marked and the areal pore density is $\sim 0.7 \times 10^{18} \text{ m}^{-2}$ . (b) 155 pores are marked and the areal pore density is $\sim 0.6 \times 10^{18} \text{ m}^{-2}$ . (c) 330 pores are marked and the areal pore density is $\sim 0.5 \times 10^{18} \text{ m}^{-2}$ . (d) A large-scale AFM image which clearly shows that the TPT CNMs consist of a high density of sub-nm pores. ....   | 70 |
| <b>Figure 4.15.</b> (a) AFM image of TPT CNM measured at 93 K in UHV via AFM tapping mode of operation (amplitude set point $A = 7.6$ nm, center frequency $f_0 = 274.8$ kHz). (b) A drawing of the marked pore in (a) by Chemdraw program (PerkinElmer Informatics). (c) The estimated pore diameter distributions ( $0.7 \pm 0.1$ nm, the error bar denotes standard deviation) extracted from the acquired AFM images.....  | 71 |
| <b>Figure 4.16.</b> Molecular dynamic simulations on water flow in CNTs. <sup>122</sup> (a) Relationship between average flow velocity and applied pressure gradient for the 75 nm long CNTs. (b) Flow enhancement factor as a function of the CNT diameter. The enhancement factor is defined as the ratio of observed flow rate to the estimations from the Poiseuille law. (c) molecular dynamics simulation snapshots of water structures inside the 0.83–1.66 nm diameter CNTs. Adapted with permission from ref. 122, American Physical Society..... | 73 |
| <b>Figure 4.17.</b> A comparison of single-channel water permeation coefficients between different membranes. Molecular dynamics simulation was used to study the permeation coefficients of CNTs ((5,5)CNT, <sup>45</sup> (6,6)CNT <sup>45</sup> ), and a stopped-flow apparatus was employed to characterize aquaporins (AQP1, <sup>124</sup> AqpZ <sup>125</sup> ). .....   | 74 |
| <b>Figure 4.18.</b> Schematic of gas and water transport path through the nanochannels in CNMs. Water molecules permeate cooperatively through the channel as a single file. In comparison, helium exhibits no strong interactions at room temperature. Besides, the steric hindrance could also impede the helium permeation, but has no effect on water permeation.....  | 75 |

- Figure 5.1.** Ionic conductance measurements. (a) Photograph of the permeation cell. (b) Schematic of the experimental principle. (c) Exclusion of large air bubbles in the permeation cell after mounting the samples: photograph view through the window of the permeation cell (left), and optical microscope image of Si chips from the top view (middle) and bottom view (right). ..... 78
- Figure 5.2.** Data acquisition and analysis using DC method. (a) The raw data collected from the Electrical Patch device and the filtered data used for analyzing. Histogram of current distribution of (b) raw data and (c) filtered data. The bin size is taken as 1.... 79
- Figure 5.3.** Ion conductance measurements with 20 mM KCl solution. (a) I–V curves of a 15  $\mu\text{m}$  aperture without TPT CNMs covered. The dashed line is a linear fit of the experimental data. The red curve is a plot of theoretical values obtained from Equation 5.1. (b) I–V curves of a sealed Si chip and a 15  $\mu\text{m}$  aperture with TPT CNMs covered. The error bar denotes the accuracy of determining current by the measurement. .... 80
- Figure 5.4.** Ionic conductance measurements. (a) I–V curves of TPT CNMs suspending over a 15  $\mu\text{m}$  circular aperture in a  $\text{Si}_3\text{N}_4/\text{Si}$  chip in 1 M solutions of HCl, LiCl, KCl, NaCl and  $\text{MgCl}_2$ . (b) I–V curves of a 15  $\mu\text{m}$  circular aperture and a sealed  $\text{Si}_3\text{N}_4/\text{Si}$  chip in 1 M KCl solution. The error bar denotes the accuracy of determining current by the measurement. .... 81
- Figure 5.5.** Ionic conductance measurements: I–V curves of TPT CNMs measured in 1M solutions of HCl (a), LiCl (b), KCl (c), NaCl (d), and  $\text{MgCl}_2$  (e). 1–5 corresponds to 5 TPT CNM samples. The error bar denotes the accuracy of determining the current by the measurement..... 82
- Figure 5.6.** Ionic conductance and dielectric breakdown characterization in 1 M KCl. (a) Current probed at varied voltages as a function of time for TPT CNMs. (b) I–V curves for pristine TPT CNMs, measurements after applying 50 V across the membrane for 1 min, and after placing the permeation cell into an ultrasonic bath for 5 s. (c) Current as a function of time for a TPT CNM with  $\sim 0.6 \mu\text{m}^2$  defects. (d) I–V curves for the defective TPT CNMs. The current values shown in b and d is average values of the signal detected in a and c. The red dashed line is a linear fit of the experimental data. The error bar denotes the accuracy of determining current by the measurement. .... 83
- Figure 5.7.** Helium ion micrograph of two TPT CNM samples after ion conductance measurements. (a) a pristine sample. (b) a sample rinsed with water after measurements. .... 84
- Figure 5.8.** Electrochemical impedance spectra characterization. (a) Nyquist plots of impedance spectra for TPT CNMs measured in 1 M solutions of HCl, LiCl, KCl, NaCl

|   |    |
|---|----|
| and MgCl <sub>2</sub> . (b) Equivalent circuit model for impedance spectra in a.....  | 85 |
| <b>Figure 5.9.</b> Comparison of ionic diffusion resistance through the aperture and TPT CNMs in a variety of 1 M chloride solutions.....   | 86 |
| <b>Figure 5.10.</b> Zeta potential measurements of TPT CNMs on an Au/mica substrate (before transfer) and on a PAN support (after transfer). .....  | 87 |
| <b>Figure 5.11.</b> A comparison of ion transport behaviors between TPT CNMs and biological systems. (a) Specific resistance of TPT CNMs, pure lipid bilayers (PI, <sup>135</sup> OxCh, <sup>135</sup> BLM1 <sup>136</sup> and BLM2 <sup>137</sup> ) and bilayers with a single ion channel (PI+porin, <sup>135</sup> OxCh+porin, <sup>135</sup> BLM1+gramicidin <sup>136</sup> and BLM2+1channel <sup>137</sup> ). The resistance of planar lipid bilayers differs in varied salt concentration and types, in a wide range of 10 <sup>4</sup> –10 <sup>7</sup> Ω·cm <sup>2</sup> , thus the literature values selected for comparison are acquired in 1–2 M KCl solution. (b) Single-channel conductance of TPT CNMs and biological ion channels (NanC, <sup>138</sup> Amylosin, <sup>139</sup> chloroplast, <sup>140</sup> OprP, <sup>141</sup> protein P, <sup>142</sup> C. crescentus, <sup>143</sup> Tsx, <sup>144</sup> TolC, <sup>145</sup> Y118 mutants <sup>146</sup> )..... | 89 |
| <b>Figure 5.12.</b> EIS measurements in 1M HCl solution. Nyquist plots (a), bode plots of impedance magnitude  Z  (b) and phase shift (c) as a function of frequency for the aperture, TPT CNMs and sealed Si chip.....   | 90 |

## List of Tables

**Table 3.1.** Varied conditions for preparing CNMs from HPB derivative 1.

**Table 4.1.** Kinetic diameters of gases and liquids.<sup>108,112</sup> The values are taken from refs. 108 and 112.

**Table 5.1.** Analysis of data extracted from the Gaussian fit in Figure 5.2.

**Table 5.2.** Hydration radius of ionic species.<sup>131</sup> Data is taken from ref. 131.

## References

1. Loeb, S.; Sourirajan, S. Sea Water Demineralization by Means of an Osmotic Membrane. In *Saline Water Conversion—II*, AMERICAN CHEMICAL SOCIETY: 1963; Vol. 38, pp 117-132.
2. Baker, R. W. *Membrane Technology and Applications*. Wiley: 2004.
3. Sholl, D. S.; Lively, R. P. Seven Chemical Separations to Change the World. *Nature* **2016**, *532*, 6-8.
4. Historical Research Highlights: First Demonstration of Reverse Osmosis. <https://samueli.ucla.edu/historical-research-highlights/> (accessed 10 December 2018).
5. Wang, L.; Boutilier, M. S. H.; Kidambi, P. R.; Jang, D.; Hadjiconstantinou, N. G.; Karnik, R. Fundamental Transport Mechanisms, Fabrication and Potential Applications of Nanoporous Atomically Thin Membranes. *Nat. Nanotech.* **2017**, *12*, 509-522.
6. Cussler, E. L. *Diffusion: Mass Transfer in Fluid Systems*. Cambridge University Press: New York, 2007; p 86-88.
7. Wijmans, J. G.; Baker, R. W. The Solution-Diffusion Model: A Review. *J. Membr. Sci.* **1995**, *107*, 1-21.
8. Cen, Y.; Lichtenthaler, R. N. Chapter 3 Vapor Permeation. In *Membrane Science and Technology*, Noble, R. D., Stern, S. A., Eds. Elsevier: 1995; Vol. 2, pp 85-112.
9. Einstein, A. *Investigations on the Theory of Brownian Movement*. Dover Publications: New York, NY, USA, 1956.
10. Ferry, J. D. Statistical Evaluation of Sieve Constants in Ultrafiltration. *The Journal of General Physiology* **1936**, *20*, 95.
11. Deen, W. M. Hindered Transport of Large Molecules in Liquid-Filled Pores. *AIChE Journal* **1987**, *33*, 1409-1425.
12. Han, J.; Fu, J.; Schoch, R. B. Molecular Sieving Using Nanofilters: Past, Present and Future. *Lab on a Chip* **2008**, *8*, 23-33.
13. Brenner, H.; Gaydos, L. J. The Constrained Brownian Movement of Spherical Particles in Cylindrical Pores of Comparable Radius: Models of the Diffusive and Convective Transport of Solute Molecules in Membranes and Porous Media. *Journal of Colloid and Interface Science* **1977**, *58*, 312-356.
14. Barrer, R. M. Diffusion in Porous Media. *Applied Materials Research* **1963**, *2*, 129-143.

15. HyperPhysics Mean Free Path. <http://hyperphysics.phy-astr.gsu.edu/hbase/Kinetic/menfre.html> (accessed 29.01.2019).
16. Serway, R. A.; Jewett, J. W. *Physics for Scientists and Engineers with Modern Physics, Technology Update*. Cengage Learning: 2015.
17. Maxwell, J. C. V. Illustrations of the Dynamical Theory of Gases.—Part I. On the Motions and Collisions of Perfectly Elastic Spheres. *The London, Edinburgh, and Dublin Philosophical Magazine and Journal of Science* **1860**, *19*, 19-32.
18. Clausius, R. Ueber Die Art Der Bewegung, Welche Wir Wärme Nennen. *Annalen der Physik* **1857**, *176*, 353-380.
19. Cunningham, R. E.; Williams, R. J. J. *Diffusion in Gases and Porous Media*. Plenum Press: 1980.
20. Suter, S. P.; Skalak, R. The History of Poiseuille's Law. *Annual Review of Fluid Mechanics* **1993**, *25*, 1-20.
21. Bear, J. *Dynamics of Fluids in Porous Media*. Dover: 1988.
22. Werber, J. R.; Osuji, C. O.; Elimelech, M. Materials for Next-Generation Desalination and Water Purification Membranes. *Nat. Rev. Mater.* **2016**, *1*, 16018.
23. Livingston, A.; College, I.; Baker, R.; Technology, M. Membranes from Academia to Industry. *Nature Materials* **2017**, *16*, 280-282.
24. Park, H. B.; Kamcev, J.; Robeson, L. M.; Elimelech, M.; Freeman, B. D. Maximizing the Right Stuff: The Trade-Off between Membrane Permeability and Selectivity. *Science* **2017**, *356*, eaab0530.
25. Tiraferri, A.; Yip, N. Y.; Phillip, W. A.; Schiffman, J. D.; Elimelech, M. Relating Performance of Thin-Film Composite Forward Osmosis Membranes to Support Layer Formation and Structure. *J. Membr. Sci.* **2011**, *367*, 340-352.
26. Robeson, L. M. The Upper Bound Revisited. *J. Membr. Sci.* **2008**, *320*, 390-400.
27. Geise, G. M.; Park, H. B.; Sagle, A. C.; Freeman, B. D.; McGrath, J. E. Water Permeability and Water/Salt Selectivity Tradeoff in Polymers for Desalination. *J. Membr. Sci.* **2011**, *369*, 130-138.
28. Elimelech, M.; Phillip, W. A. The Future of Seawater and the Environment: Energy, Technology, and the Environment. *Science* **2011**, *333*, 712-718.
29. Karan, S.; Jiang, Z.; Livingston, A. G. Sub-10 nm Polyamide Nanofilms with Ultrafast Solvent Transport for Molecular Separation. *Science* **2015**, *348*, 1347-1351.
30. Chowdhury, M. R.; Steffes, J.; Huey, B. D.; McCutcheon, J. R. 3d Printed Polyamide Membranes for Desalination. *Science* **2018**, *361*, 682.
31. Park, H. G.; Jung, Y. Carbon Nanofluidics of Rapid Water Transport for Energy Applications. *Chem. Soc. Rev.* **2014**, *43*, 565-576.
32. Tang, C.; Wang, Z.; Petrini, I.; Fane, A. G.; Helix-Nielsen, C. Biomimetic Aquaporin Membranes Coming of Age. *Desalination* **2014**, *368*, 89-105.



33. Holt, J. K.; Park, H. G.; Wang, Y.; Stadermann, M.; Artyukhin, A. B.; Grigoropoulos, C. P.; Noy, A.; Bakajin, O. Fast Mass Transport through Sub-2-Nanometer Carbon Nanotubes. *Science* **2006**, *312*, 1034-1037.
34. Bui, N.; Meshot, E. R.; Kim, S.; Peña, J.; Gibson, P. W.; Wu, K. J.; Fornasiero, F. Ultrabreathable and Protective Membranes with Sub-5 nm Carbon Nanotube Pores. *Adv. Mater.* **2016**, *28*, 5871-5877.
35. Bachman, J. E.; Smith, Z. P.; Li, T.; Xu, T.; Long, J. R. Enhanced Ethylene Separation and Plasticization Resistance in Polymer Membranes Incorporating Metal–Organic Framework Nanocrystals. *Nature Materials* **2016**, *15*, 845-849.
36. Koros, W. J.; Zhang, C. Materials for Next-Generation Molecularly Selective Synthetic Membranes. *Nature Materials* **2017**, *16*, 289-297.
37. Celebi, K.; Buchheim, J.; Wyss, R. M.; Droudian, A.; Gasser, P.; Shorubalko, I.; Kye, J. I. J.-I.; Lee, C.; Park, H. G. Ultimate Permeation across Atomically Thin Porous Graphene. *Science* **2014**, *344*, 289-292.
38. O'Hern, S. C.; Jang, D.; Bose, S.; Idrobo, J. C.; Song, Y.; Laoui, T.; Kong, J.; Karnik, R. Nanofiltration across Defect-Sealed Nanoporous Monolayer Graphene. *Nano Lett.* **2015**, *15*, 3254-3260.
39. The Nobel Prize in Chemistry 2003. Nobelprize.Org. Nobel Media Ab 2019. Wed. 6 Feb 2019.
40. Zhao, Y.; Qiu, C.; Li, X.; Vararattanavech, A.; Shen, W.; Torres, J.; Hélix-Nielsen, C.; Wang, R.; Hu, X.; Fane, A. G.; Tang, C. Y. Synthesis of Robust and High-Performance Aquaporin-Based Biomimetic Membranes by Interfacial Polymerization-Membrane Preparation and RO Performance Characterization. *J. Membr. Sci.* **2012**, *423-424*, 422-428.
41. Morris, W.; Doonan, C. J.; Furukawa, H.; Banerjee, R.; Yaghi, O. M. Crystals as Molecules: Postsynthesis Covalent Functionalization of Zeolitic Imidazolate Frameworks. *Journal of the American Chemical Society* **2008**, *130*, 12626-12627.
42. Bae, T.-H.; Lee, J. S.; Qiu, W.; Koros, W. J.; Jones, C. W.; Nair, S. A High-Performance Gas-Separation Membrane Containing Submicrometer-Sized Metal–Organic Framework Crystals. *Angew. Chem. Int. Ed.* **2010**, *49*, 9863-9866.
43. Agre, P. Aquaporin Water Channels (Nobel Lecture). *Angew. Chem. Int. Ed.* **2004**, *43*, 4278-4290.
44. Hummer, G.; Rasaiah, J. C.; Noworyta, J. P. Water Conduction through the Hydrophobic Channel of a Carbon Nanotube. *Nature* **2001**, *414*, 188-190.
45. Corry, B. Designing Carbon Nanotube Membranes for Efficient Water Desalination. *J. Phys. Chem. B* **2008**, *112*, 1427-1434.
46. Majumder, M.; Chopra, N.; Andrews, R.; Hinds, B. J. Nanoscale Hydrodynamics: Enhanced Flow in Carbon Nanotubes. *Nature* **2005**, *438*, 44.

47. Thostenson, E. T.; Ren, Z.; Chou, T.-W. Advances in the Science and Technology of Carbon Nanotubes and Their Composites: A Review. *Composites Science and Technology* **2001**, *61*, 1899-1912.
48. Li, J.-R.; Sculley, J.; Zhou, H.-C. Metal–Organic Frameworks for Separations. *Chemical Reviews* **2012**, *112*, 869-932.
49. O'Hern, S. C.; Boutilier, M. S. H.; Idrobo, J. C.; Song, Y.; Kong, J.; Laoui, T.; Atieh, M.; Karnik, R. Selective Ionic Transport through Tunable Subnanometer Pores in Single-Layer Graphene Membranes. *Nano Lett.* **2014**, *14*, 1234-1241.
50. Joshi, R. K.; Carbone, P.; Wang, F. C.; Kravets, V. G.; Su, Y.; Grigorieva, I. V.; Wu, H. A.; Geim, A. K.; Nair, R. R. Precise and Ultrafast Molecular Sieving through Graphene Oxide Membranes. *Science* **2014**, *343*, 752-754.
51. Gopinadhan, K.; Hu, S.; Esfandiar, A.; Lozada-Hidalgo, M.; Wang, F. C.; Yang, Q.; Tyurnina, A. V.; Keerthi, A.; Radha, B.; Geim, A. K. Complete Steric Exclusion of Ions and Proton Transport through Confined Monolayer Water. *Science* **2019**, *363*, 145-148.
52. Berry, V. Impermeability of Graphene and Its Applications. *Carbon* **2013**, *62*, 1-10.
53. Buchheim, J.; Wyss, R. M.; Kim, C.-M.; Deng, M.; Park, H. G. Architecture and Transport Properties of Membranes out of Graphene. *Membr. J.* **2016**, *26*, 239-252.
54. Nair, R. R.; Wu, H. A.; Jayaram, P. N.; Grigorieva, I. V.; Geim, A. K. Unimpeded Permeation of Water through Helium-Leak-Tight Graphene-Based Membranes. *Science* **2012**, *335*, 442-444.
55. Zheng, S.; Tu, Q.; Urban, J. J.; Li, S.; Mi, B. Swelling of Graphene Oxide Membranes in Aqueous Solution: Characterization of Interlayer Spacing and Insight into Water Transport Mechanisms. *ACS Nano* **2017**, *11*, 6440-6450.
56. Radha, B.; Esfandiar, A.; Wang, F. C.; Rooney, A. P.; Gopinadhan, K.; Keerthi, A.; Mishchenko, A.; Janardanan, A.; Blake, P.; Fumagalli, L.; Lozada-Hidalgo, M.; Garaj, S.; Haigh, S. J.; Grigorieva, I. V.; Wu, H. A.; Geim, A. K. Molecular Transport through Capillaries Made with Atomic-Scale Precision. *Nature* **2016**, *538*, 222-225.
57. Turchanin, A.; Götzhäuser, A. Carbon Nanomembranes. *Adv. Mater.* **2016**, *28*, 6075–6103.
58. Zhang, X.; Neumann, C.; Angelova, P.; Beyer, A.; Götzhäuser, A. Tailoring the Mechanics of Ultrathin Carbon Nanomembranes by Molecular Design. *Langmuir* **2014**, *30*, 8221-8227.
59. Turchanin, A.; El-Desawy, M.; Götzhäuser, A. High Thermal Stability of Cross-Linked Aromatic Self-Assembled Monolayers: Nanopatterning Via Selective Thermal Desorption. *Appl. Phys. Lett.* **2007**, *90*, 1-4.
60. Matei, D. G.; Weber, N.-E.; Kurasch, S.; Wundrack, S.; Woszczyna, M.; Grothe, M.; Weimann, T.; Ahlers, F.; Stosch, R.; Kaiser, U.; Turchanin, A. Functional Single-Layer Graphene Sheets from Aromatic Monolayers. *Adv. Mater.* **2013**, *25*, 4146-4151.

61. Ferrari, A. C.; Basko, D. M. Raman Spectroscopy as a Versatile Tool for Studying the Properties of Graphene. *Nat. Nanotech.* **2013**, *8*, 235.
62. Turchanin, A.; Beyer, A.; Nottbohm, C. T.; Zhang, X.; Stosch, R.; Sologubenko, A.; Mayer, J.; Hinze, P.; Weimann, T.; Götzhäuser, A. One Nanometer Thin Carbon Nanosheets with Tunable Conductivity and Stiffness. *Adv. Mater.* **2009**, *21*, 1233-1237.
63. Angelova, P.; Vieker, H.; Weber, N.-E.; Matei, D.; Reimer, O.; Meier, I.; Kurasch, S.; Biskupek, J.; Lorbach, D.; Wunderlich, K.; Chen, L.; Terfort, A.; Klapper, M.; Müllen, K.; Kaiser, U.; Götzhäuser, A.; Turchanin, A. A Universal Scheme to Convert Aromatic Molecular Monolayers into Functional Carbon Nanomembranes. *ACS Nano* **2013**, *7*, 6489-6497.
64. Zheng, Z.; Nottbohm, C. T.; Turchanin, A.; Muzik, H.; Beyer, A.; Heilemann, M.; Sauer, M.; Götzhäuser, A. Janus Nanomembranes: A Generic Platform for Chemistry in Two Dimensions. *Angew. Chem. Int. Ed.* **2010**, *49*, 8493-8497.
65. Kendall, K. Adhesion: Molecules and Mechanics. *Science* **1994**, *263*, 1720-1725.
66. Penner, P.; Zhang, X.; Marschewski, E.; Behler, F.; Angelova, P.; Beyer, A.; Christoffers, J.; Götzhäuser, A. Charge Transport through Carbon Nanomembranes. *J. Phys. Chem. C* **2014**, *118*, 21687-21694.
67. Ai, M.; Shishatskiy, S.; Wind, J.; Zhang, X.; Nottbohm, C. T.; Mellech, N.; Winter, A.; Vieker, H.; Qiu, J.; Dietz, K. J.; Götzhäuser, A.; Beyer, A. Carbon Nanomembranes (CNMs) Supported by Polymer: Mechanics and Gas Permeation. *Adv. Mater.* **2014**, *26*, 3421-3426.
68. Turchanin, A.; Götzhäuser, A. Carbon Nanomembranes from Self-Assembled Monolayers: Functional Surfaces without Bulk. *Progr. Surf. Sci.* **2012**, *87*, 108-162.
69. Love, J. C.; Estroff, L. A.; Kriebel, J. K.; Nuzzo, R. G.; Whitesides, G. M. Self-Assembled Monolayers of Thiolates on Metals as a Form of Nanotechnology. *Chemical Reviews* **2005**, *105*, 1103-1170.
70. Hammer, B.; Norskov, J. K. Why Gold Is the Noblest of All the Metals. *Nature* **1995**, *376*, 238.
71. Adamson, A. W.; Gast, A. P. *Physical Chemistry of Surfaces*. Wiley: 1997.
72. Schessler, H. M.; Karpovich, D. S.; Blanchard, G. J. Quantitating the Balance between Enthalpic and Entropic Forces in Alkanethiol/Gold Monolayer Self Assembly. *Journal of the American Chemical Society* **1996**, *118*, 9645-9651.
73. Zhong, C.-J.; Porter, M. D. Evidence for Carbon-Sulfur Bond Cleavage in Spontaneously Adsorbed Organosulfide-Based Monolayers at Gold. *Journal of the American Chemical Society* **1994**, *116*, 11616-11617.
74. Nuzzo, R. G.; Dubois, L. H.; Allara, D. L. Fundamental Studies of Microscopic Wetting on Organic Surfaces. 1. Formation and Structural Characterization of a Self-Consistent Series of Polyfunctional Organic Monolayers. *Journal of the American Chemical Society* **1990**, *112*, 558-569.

75. Geyer, W.; Stadler, V.; Eck, W.; Zharnikov, M.; Götzhäuser, A.; Grunze, M. Electron-Induced Crosslinking of Aromatic Self-Assembled Monolayers: Negative Resists for Nanolithography. *Appl. Phys. Lett.* **1999**, *75*, 2401-2403.
76. Turchanin, A.; Schnietz, M.; El-Desawy, M.; Solak, H. H.; David, C.; Götzhäuser, A. Fabrication of Molecular Nanotemplates in Self-Assembled Monolayers by Extreme-Ultraviolet-Induced Chemical Lithography. *Small* **2007**, *3*, 2114-2119.
77. Völkel, B.; Götzhäuser, A.; Müller, H. U.; David, C.; Grunze, M. Influence of Secondary Electrons in Proximal Probe Lithography. *J. Vac. Sci. Technol., B: Microelectron. Nanometer Struct.* **1997**, *15*, 2877-2877.
78. Turchanin, A.; Käfer, D.; El-Desawy, M.; Wöll, C.; Witte, G.; Götzhäuser, A. Molecular Mechanisms of Electron-Induced Cross-Linking in Aromatic Sams. *Langmuir* **2009**, *25*, 7342-7352.
79. Briggs, D.; Grant, J. T. *Surface Analysis by Auger and X-Ray Photoelectron Spectroscopy*. SurfaceSpectra: Manchester, UK, 2003.
80. Kano, S.; Tada, T.; Majima, Y. Nanoparticle Characterization Based on Stm and Sts. *Chem. Soc. Rev.* **2015**, *44*, 970-987.
81. Vang, R. T.; Lauritsen, J. V.; Lægsgaard, E.; Besenbacher, F. Scanning Tunneling Microscopy as a Tool to Study Catalytically Relevant Model Systems. *Chem. Soc. Rev.* **2008**, *37*, 2191-2203.
82. Marshall, M. S. J.; Castell, M. R. Scanning Tunnelling Microscopy of Epitaxial Nanostructures. *Chem. Soc. Rev.* **2014**, *43*, 2226-2239.
83. Giessibl, F. J. Advances in Atomic Force Microscopy. *Rev. Mod. Phys.* **2003**, *75*, 949-983.
84. Hinterdorfer, P.; Dufrêne, Y. F. Detection and Localization of Single Molecular Recognition Events Using Atomic Force Microscopy. *Nature Methods* **2006**, *3*, 347.
85. Reifenger, R. *Fundamentals of Atomic Force Microscopy Part I: Foundations*. World Scientific Publishing Co. Pte. Ltd.: Singapore, 2016.
86. Tomczak, N.; Goh, K. E. J. *Scanning Probe Microscopy*. World Scientific Publishing Company: 2011.
87. Morgan, J.; Notte, J.; Hill, R.; Ward, B. An Introduction to the Helium Ion Microscope. *Microscopy Today* **2006**, *14*, 24-31.
88. Vieker, H. Helium Ion Microscopy: A New Tool to Analyze and Modify Nanoscale Objects. Bielefeld Univeristy, Bielefeld: Universitätsbibliothek Bielefeld, 2014.
89. Orazem, M. E.; Tribollet, B. *Electrochemical Impedance Spectroscopy*. Wiley: 2011.
90. Rubinson, J. F.; Kayinamura, Y. P. Charge Transport in Conducting Polymers: Insights from Impedance Spectroscopy. *Chem. Soc. Rev.* **2009**, *38*, 3339-3347.
91. Barsoukov, E.; Macdonald, J. R. *Impedance Spectroscopy: Theory, Experiment, and Applications*. Wiley: 2005.

92. Brug, G. J.; van den Eeden, A. L. G.; Sluyters-Rehbach, M.; Sluyters, J. H. The Analysis of Electrode Impedances Complicated by the Presence of a Constant Phase Element. *Journal of Electroanalytical Chemistry and Interfacial Electrochemistry* **1984**, *176*, 275-295.
93. Castner, D. G.; Hinds, K.; Grainger, D. W. X-Ray Photoelectron Spectroscopy Sulfur 2p Study of Organic Thiol and Disulfide Binding Interactions with Gold Surfaces. *Langmuir* **1996**, *12*, 5083-5086.
94. Angelova, P.; Solel, E.; Parvari, G.; Turchanin, A.; Botoshansky, M.; Götzhäuser, A.; Keinan, E. Chemisorbed Monolayers of Corannulene Penta-Thioethers on Gold. *Langmuir* **2013**, *29*, 2217-2223.
95. Ahn, H.; Zharnikov, M.; Whitten, J. E. Abnormal Pinning of the Fermi and Vacuum Levels in Monomolecular Self-Assembled Films. *Chem. Phys. Lett.* **2006**, *428*, 283-287.
96. Laibinis, P. E.; Whitesides, G. M.; Allara, D. L.; Tao, Y. T.; Parikh, A. N.; Nuzzo, R. G. Comparison of the Structures and Wetting Properties of Self-Assembled Monolayers of N-Alkanethiols on the Coinage Metal Surfaces, Copper, Silver, and Gold. *Journal of the American Chemical Society* **1991**, *113*, 7152-7167.
97. Ito, Y.; Christodoulou, C.; Nardi, M. V.; Koch, N.; Kläui, M.; Sachdev, H.; Müllen, K. Tuning the Magnetic Properties of Carbon by Nitrogen Doping of Its Graphene Domains. *Journal of the American Chemical Society* **2015**, *137*, 7678-7685.
98. Heister, K.; Zharnikov, M.; Grunze, M.; Johansson, L. S. O.; Ulman, A. Characterization of X-Ray Induced Damage in Alkanethiolate Monolayers by High-Resolution Photoelectron Spectroscopy. *Langmuir* **2001**, *17*, 8-11.
99. Zharnikov, M. High-Resolution X-Ray Photoelectron Spectroscopy in Studies of Self-Assembled Organic Monolayers. *J. Electron Spectrosc. Relat. Phenom.* **2010**, *178-179*, 380-393.
100. Yang, Y.; Dementyev, P.; Biere, N.; Emmrich, D.; Stohmann, P.; Korzetz, R.; Zhang, X.; Beyer, A.; Koch, S.; Anselmetti, D.; Götzhäuser, A. Rapid Water Permeation through Carbon Nanomembranes with Sub-Nanometer Channels. *ACS Nano* **2018**, *12*, 4695-4701.
101. ASTM E96/E96m-16, Standard Test Methods for Water Vapor Transmission of Materials. ASTM International: West Conshohocken, PA, 2016.
102. Greenspan, L. Humidity Fixed Points of Binary Saturated Aqueous Solutions. *J. Res. Natl. Bur. Stand. Sect. A* **1977**, *81A*, 89-89.
103. Crank, J. *The Mathematics of Diffusion*. Oxford University Press: Ely House, London, UK, 1975.
104. Saito, Y. A Theoretical Study on the Diffusion Current at the Stationary Electrodes of Circular and Narrow Band Types. *Rev. Polarogr.* **1968**, *15*, 177-187.
105. Marrero, T. R.; Mason, E. A. Gaseous Diffusion Coefficients. *J. Phys. Chem. Ref. Data* **1972**, *1*, 3-118.

106. Li, X.; Wang, R.; Wicaksana, F.; Tang, C.; Torres, J.; Fane, A. G. Preparation of High Performance Nanofiltration (Nf) Membranes Incorporated with Aquaporin Z. *J. Membr. Sci.* **2014**, *450*, 181-188.
107. McCullough, E. A.; Kwon, M.; Shim, H. A Comparison of Standard Methods for Measuring Water Vapour Permeability of Fabrics. *Meas. Sci. Technol.* **2003**, *14*, 1402-1408.
108. Van der Perre, S.; Van Assche, T.; Bozbiyik, B.; Lannoeye, J.; De Vos, D. E.; Baron, G. V.; Denayer, J. F. M. Adsorptive Characterization of the ZIF-68 Metal-Organic Framework: A Complex Structure with Amphiphilic Properties. *Langmuir* **2014**, *30*, 8416-8424.
109. Thies, S. Benetzbarkeit Und Oberflächenenergie Von Aromatischen Sams Und Cnms. Bachelor Thesis, Bielefeld University, 2015.
110. Firpo, G.; Angeli, E.; Repetto, L.; Valbusa, U. Permeability Thickness Dependence of Polydimethylsiloxane (Pdms) Membranes. *J. Membr. Sci.* **2015**, *481*, 1-8.
111. Bowden, F. P.; Throssell, W. R. Adsorption of Water Vapour on Solid Surfaces. *Nature* **1951**, *167*, 601-602.
112. Breck, D. W. *Zeolite Molecular Sieves: Structure, Chemistry, and Use*. R.E. Krieger: 1984.
113. Delamarche, E.; Michel, B.; Gerber, C.; Anselmetti, D.; Guntherodt, H. J.; Wolf, H.; Ringsdorf, H. Real-Space Observation of Nanoscale Molecular Domains in Self-Assembled Monolayers. *Langmuir* **1994**, *10*, 2869-2871.
114. Korolkov, V. V.; Allen, S.; Roberts, C. J.; Tendler, S. J. B. High-Temperature Adsorption of P-Terphenylthiol on Au(111) Surfaces. *J. Phys. Chem. C* **2011**, *115*, 14899-14906.
115. Bashir, A.; Azzam, W.; Rohwerder, M.; Terfort, A. Polymorphism in Self-Assembled Terphenylthiolate Monolayers on Au(111). *Langmuir* **2013**, *29*, 13449-13456.
116. Houplin, J.; Dablemont, C.; Sala, L.; Lafosse, A.; Amiaud, L. Electron Processing at 50 Ev of Terphenylthiol Self-Assembled Monolayers: Contributions of Primary and Secondary Electrons. *Langmuir* **2015**, *31*, 13528-13534.
117. García, R.; San Paulo, A. Attractive and Repulsive Tip-Sample Interaction Regimes in Tapping-Mode Atomic Force Microscopy. *Phys. Rev. B* **1999**, *60*, 4961-4967.
118. Sampson, R. A. On Stokes's Current Function. *Philos. Trans. R. Soc., A* **1891**, *182*, 449-518.
119. Dagan, Z.; Weinbaum, S.; Pfeffer, R. An Infinite-Series Solution for the Creeping Motion through an Orifice of Finite Length. *J. Fluid Mech.* **1982**, *115*, 505-505.

120. Sun, C.; Boutilier, M. S. H.; Au, H.; Poesio, P.; Bai, B.; Karnik, R.; Hadjiconstantinou, N. G. Mechanisms of Molecular Permeation through Nanoporous Graphene Membranes. *Langmuir* **2014**, *30*, 675-682.
121. Qin, X.; Yuan, Q.; Zhao, Y.; Xie, S.; Liu, Z. Measurement of the Rate of Water Translocation through Carbon Nanotubes. *Nano Lett.* **2011**, *11*, 2173-2177.
122. Thomas, J. A.; McGaughey, A. J. H. Water Flow in Carbon Nanotubes: Transition to Subcontinuum Transport. *Phys. Rev. Lett.* **2009**, *102*, 184502.
123. Thomas, J. A.; McGaughey, A. J. H. Reassessing Fast Water Transport through Carbon Nanotubes. *Nano Lett.* **2008**, *8*, 2788-2793.
124. Walz, T.; Smith, B. L.; Zeidel, M. L.; Engel, A.; Agre, P. Biologically Active Two-Dimensional Crystals of Aquaporin Chip. *J. Biol. Chem.* **1994**, *269*, 1583-1586.
125. Borgnia, M. J.; Kozono, D.; Calamita, G.; Maloney, P. C.; Agre, P. Functional Reconstitution and Characterization of Aqpz, the E. Coli Water Channel Protein. *J. Mol. Biol.* **1999**, *291*, 1169-1179.
126. Köfinger, J.; Hummer, G.; Dellago, C. Single-File Water in Nanopores. *Phys. Chem. Chem. Phys.* **2011**, *13*, 15403-15417.
127. Ball, D. W. *Physical Chemistry*. Cengage Learning: 2014.
128. Hall, J. E. Access Resistance of a Small Circular Pore. *The Journal of General Physiology* **1975**, *66*, 531-532.
129. Penner, R. A Practical Guide to Patch Clamping. In *Single-Channel Recording*, Sakmann, B., Neher, E., Eds. Springer US: Boston, MA, 1995; pp 3-30.
130. Kwok, H.; Briggs, K.; Tabard-Cossa, V. Nanopore Fabrication by Controlled Dielectric Breakdown. *PLoS ONE* **2014**, *9*.
131. Nightingale, E. R. Phenomenological Theory of Ion Solvation. Effective Radii of Hydrated Ions. *The Journal of Physical Chemistry* **1959**, *63*, 1381-1387.
132. de Groot, B. L.; Frigato, T.; Helms, V.; Grubmüller, H. The Mechanism of Proton Exclusion in the Aquaporin-1 Water Channel. *J. Mol. Biol.* **2003**, *333*, 279-293.
133. Burykin, A.; Warshel, A. What Really Prevents Proton Transport through Aquaporin? Charge Self-Energy Versus Proton Wire Proposals. *Biophys. J.* **2003**, *85*, 3696-3706.
134. Dellago, C.; Naor, M. M.; Hummer, G. Proton Transport through Water-Filled Carbon Nanotubes. *Phys. Rev. Lett.* **2003**, *90*, 105902.
135. Micelli, S.; Gallucci, E.; Meleleo, D.; Stipani, V.; Picciarelli, V. Mitochondrial Porin Incorporation into Black Lipid Membranes: Ionic and Gating Contribution to the Total Current. *Bioelectrochemistry* **2002**, *57*, 97-106.
136. Hirano-Iwata, A.; Aoto, K.; Oshima, A.; Taira, T.; Yamaguchi, R.-T.; Kimura, Y.; Niwano, M. Free-Standing Lipid Bilayers in Silicon Chips—Membrane Stabilization Based on Microfabricated Apertures with a Nanometer-Scale Smoothness. *Langmuir* **2010**, *26*, 1949-1952.

137. Peterman, M. C.; Ziebarth, J. M.; Braha, O.; Bayley, H.; Fishman, H. A.; Bloom, D. M. Ion Channels and Lipid Bilayer Membranes under High Potentials Using Microfabricated Apertures. *Biomedical Microdevices* **2002**, *4*, 231-236.
138. Giri, J.; Tang, J. M.; Wirth, C.; Peneff, C. M.; Eisenberg, B. Single-Channel Measurements of an N-Acetylneuraminic Acid-Inducible Outer Membrane Channel in Escherichia Coli. *European Biophysics Journal* **2012**, *41*, 259-271.
139. Saris, N. E. L.; Andersson, M. A.; Mikkola, R.; Andersson, L. C.; Teplova, V. V.; Grigoriev, P. A.; Salkinoja-Salonen, M. S. Microbial Toxin's Effect on Mitochondrial Survival by Increasing K<sup>+</sup> Uptake. *Toxicology and Industrial Health* **2009**, *25*, 441-446.
140. Fuks, B.; Homblé, F. A Voltage-Dependent Porin-Like Channel in the Inner Envelope Membrane of Plant Chloroplasts. *J. Biol. Chem.* **1995**, *270*, 9947-9952.
141. Sukhan, A.; Hancock, R. E. W. The Role of Specific Lysine Residues in the Passage of Anions through the Pseudomonas Aeruginosa Porin Oprp. *J. Biol. Chem.* **1996**, *271*, 21239-21242.
142. Hancock, R. E. W.; Poole, K.; Gimple, M.; Benz, R. Modification of the Conductance, Selectivity and Concentration-Dependent Saturation of Pseudomonas Aeruginosa Protein P Channels by Chemical Acetylation. *Biochimica et Biophysica Acta (BBA) - Biomembranes* **1983**, *735*, 137-144.
143. Benz, R.; Jones, M. D.; Younas, F.; Maier, E.; Modi, N.; Mentele, R.; Lottspeich, F.; Kleinekathöfer, U.; Smit, J. Ompw of Caulobacter Crescentus Functions as an Outer Membrane Channel for Cations. *PLOS ONE* **2015**, *10*, e0143557.
144. Benz, R.; Schmid, A.; Maier, C.; Bremer, E. Characterization of the Nucleoside-Binding Site inside the Tsx Channel of Escherichia Coli Outer Membrane Reconstitution Experiments with Lipid Bilayer Membranes. *European Journal of Biochemistry* **1988**, *176*, 699-705.
145. Polleichtner, G.; Andersen, C. The Channel-Tunnel Hi1462 of Haemophilus Influenzae Reveals Differences to Escherichia Coli Tolc. *Microbiology* **2006**, *152*, 1639-1647.
146. Orlik, F.; Andersen, C.; Benz, R. Site-Directed Mutagenesis of Tyrosine 118 within the Central Constriction Site of the Lamb (Maltoporin) Channel of Escherichia Coli. I. Effect on Ion Transport. *Biophys. J.* **2002**, *82*, 2466-2475.



## Acknowledgement

The past four and a half years is a great journey with lots of memorable moments. Apart from what I expected to acquire, the life in Germany has also influenced my ways of thinking and working. All these experiences make this journey special, which I will benefit in the rest of my life. To this end, I would like to acknowledge all those who have given me help and support.

First of all, I wish to express my deepest gratitude to my research supervisor, Prof. Dr. Armin Götzhäuser who provides me opportunities to grow up, and strong support all the time if it's needed. He knows how to motivate me and keep me on the track, meanwhile also offers me sufficient freedom. I always feel lucky to have had the chance to work in his group and truly enjoy the time here.

Secondly, I would like to say thanks to all the group members. Thank Xianghui for his help and guidance at the beginning of my PhD. The start of a new life is always tough, but he helped me to get through it. Thank Polina for picking me up on my arrival, and for her help and advices during my studies. Thank Karin and Udo for all the administration help and support. Thank Andreas, Christof, Natalie and Henning for their help on my movement to new apartment, and all the fun time, coffee, tea, movie and ikea... Thank André for his advices, and the encouragement words when I gave talks. Thanks to Berthold for all his help and advices. Thank Sascha for his help on AFM and STM measurements. He is always willing to spend a lot of time answering my questions. Thanks to Petr for his contributions to gas permeation measurements. The permeation work would not be proceeded so well without his support. I also enjoy all the discussions with him. Thank Daniel, Natalie, Henning and Michael for their help on HIM measurements. Thank Patrick for his help on STM measurements. Thanks to Riko, who provides theoretical support. He is a perceptive physicist who is always able to help solve my technical and experimental problems. Thank Raphael for his help at all times. Thank Paul, especially for driving me home after the Christmas party every year. Thank Emmanuel for his help on LabVIEW programming. Thanks to Florian for his help on

mechanical measurements. Thanks to Linh, Lena, David, Albert, Nikolaus and Melanie for their help and encouragement.

Also, I want to thank Prof. Dr. Dario Anselmetti for his supervising, as well as the support from his group members. I always feel encouraged after talking with him. Thank Niklas for his contributions on AFM measurements. Thank Rolland for his help on ion conductance measurements. Thank Sebastein for all his advices.

In addition, I want to thank Prof. Dr. Mathias Ulbricht from Universität Duisburg-Essen for his assistance with zeta potential measurements, and thank Prof. Dr. Claus Hélix-Nielsen from Technical University of Denmark for his advices on interpretation of ion conductance results.

I cannot cover everything they have done for me, but all of this will stay in my heart and be the best memories of my studies in Germany.

Finally, I want to thank my family for always being there supporting me.

